DETERMINATION OF THE SYNERGISM BETWEEN EROSION AND CORROSION IN POTASH-SAND SLURRY CORROSION OF CARBON STEEL

A Thesis Submitted to the
College of Graduate and Postdoctoral Studies
In Partial Fulfillment of the Requirements
For the Degree of Master of Science
In the Department of Chemical and Biological Engineering
University of Saskatchewan
Saskatoon

By

Michael Brent Trask

Permission To Use

In presenting this thesis in partial fulfillment of the requirements for a Postgraduate degree from the University of Saskatchewan, I agree that the Libraries of this University may make it freely available for inspection. I further agree that permission for copying of this thesis in any manner, in whole or in part, for scholarly purposes may be granted by the professor or professors who supervised my thesis work or, in their absence, by the Head of the Department or the Dean of the College in which my thesis work was done. It is understood that any copying or publication or use of this thesis or parts thereof for financial gain shall not be allowed without my written permission. It is also understood that due recognition shall be given to me and to the University of Saskatchewan in any scholarly use which may be made of any material in my thesis.

Requests for permission to copy or to make other uses of materials in this thesis in whole or part should be addressed to:

Head of the College of Engineering

57 Campus Drive

University of Saskatchewan

Saskatoon, Saskatchewan S7N 5A9 Canada

OR

Dean

College of Graduate and Postdoctoral Studies

University of Saskatchewan

116 Thorvaldson Building, 110 Science Place

Saskatoon, Saskatchewan S7N 5C9 Canada

Abstract

Erosion-corrosion is a common problem in the mining and mineral processing industries, both in Saskatchewan and other parts of the world. The combination of erosion and corrosion in flow systems may lead to severe material wear in pipelines and equipment. When erosion and corrosion interact, a synergy may occur between them. Erosion-corrosion synergism may cause more or less material loss beyond the effects of pure erosion and pure corrosion.

Experiments were performed using saturated sand-potash slurries over a wide range of solids concentrations, velocities, and two particle sizes. A flow loop apparatus circulated the slurry through an AISI 1018 carbon steel elbow. An additional apparatus was developed to apply cathodic protection to the inside surface of the elbow. The research conditions aimed to mimic those found in the potash industry. Experiments focused on determining the effect of solids concentration, flow velocity, and particle size on the protection current density (i_{prot}) and corrosion rate (CR) within the elbow.

A complex relationship was oberserved between i_{prot} and slurry concentration. As the slurry concentration was increased, i_{prot} increased up to a critical slurry concentration between 4 – 10 wt.%. Above the critical slurry concentration, i_{prot} decreased with increasing slurry concentrations. This relationship was consistent regardless of the flow velocity. Particle sizes of 0.55 mm and 1.05 mm were both examined in this research. It was observed that the elbow required a larger i_{prot} when smaller sand particles were used, relative to when larger particles were used. In all experiments, enhanced corrosion material loss caused by erosion-corrosion synergy was quantified. Enhanced corrosion was shown to increase the total corrosion rate by as much as 52% over varying slurry concentrations. Additionally, the smaller sand particle size increased the enhanced corrosion by an average of 12.5% across the conditions examined. All the observed changes in enhanced corrosion and i_{prot} were most likely caused by slurry concentration, flow velocity, and particle size altering mass transfer rates of oxygen.

From the phase IV research, a linear correlation was developed relating the CR to i_{prot}. The linear relationship was consistent for all flow velocities and slurry concentrations tested. This suggests that corrosion rates could potentially be predicted from the measurement of i_{prot} for carbon steel – potash slurry systems, and possibly others.

Acknowledgments

The research and findings presented in this thesis would not have been possible without the aid and help from many individuals. Firstly, I would like to thank Professor Richard Evitts and Dr. Glyn Kennell for their leadership, direction, and help throughout my entire degree. I also want to acknowledge my committee members, Dr. Lifeng Zhang and Dr. Ikechukwuka Oguocha, for their comments and encouragement throughout my research. Special thanks to Dakota Somers and Kasia McChesney for their aid in experiments, editing, and the completion publications. I would also like to acknowledge Dr. Raheem Elemuran, Regan Gerspacher, and Gang Li for all their help and guidance in the lab throughout my experiments. Lastly, this research could not have been made possible without the funding and support of the International Mineral Innovation Institute (IMII).

Dedication

I would like to dedicate this thesis to my wife Alora, who always encouraged me throughout the highs and lows of graduate school, and to my friends and family for their continued support during my education and research.

Table of Contents

List of Tables

List of Figures

List of Abbreviations

CE	Counter Electrode
CSE	Copper Sulphate Electrode
CR	Corrosion Rate
DC	Direct Current
DO	Dissolved Oxygen
E-C	Erosion-Corrosion
EIS	Electrical Impedance Spectroscopy
HCLA	High-Carbon Low Alloy
HSCI	High-Silicon Cast Iron
HV	Hardness Vickers
ICPS	Internal Cathodic Protection System
NAB	Nickel Aluminum Bronze
RCE	Rotating Cylinder Electrode
RE	Reference Electrode
SCE	Saturated Calomel Electrode
SHE	Standard Hydrogen Electrode
WE	Working Electrode

Nomenclature

A	Slope of Anodic/Cathodic Tafel Line	mV/Decade
b_a	Slope of Anodic Tafel Line	mV/Decade
b_c	Slope of Cathodic Tafel Line	mV/Decade
C	Mass Loss due to Corrosion	g
E	Erosion Mass Loss	g
$E°_{Anode}$	Standard Anodic Half-Cell Potential	mV
$E°_{Cathode}$	Standard Cathodic Half-Cell Potential	mV
$E°_{Cell}$	Standard Cell Potential	mV
EC	Erosion-Corrosion Mass Loss	g
E_{corr}	Corrosion Potential	mV
E_{prot}	Corrosion Protection Potential	mV
F	Faraday's Constant	96,485
i	Corrosion Current	A
i_{corr}	Corrosion Current Density	$\mu A/cm^2$
i_o	Exchange Current Density	$\mu A/cm^2$
i_{prot}	Protective Current Density	$\mu A/cm^2$
M	Molecular Weight	g/mol
M_f	Final Mass	g
M_i	Initial Mass	g
S	Erosion-Corrosion Synergy Mass Loss	g
S_C	Mass Loss due to Enhanced Corrosion	g
S_E	Mass Loss due to Enhanced Erosion	g
t	Time	seconds
η	Overpotential	mV
w	Corrosion Mass Loss	g
Z	Number of Electrons Transferred	-

1. Introduction

Corrosion is one of the leading causes of failure and maintenance costs in mineral and natural resource processing (Dai *et al.*, 2017). The annual cost attributed to corrosion is in the trillions of dollars globally (Koch *et al.*, 2016). Corrosion's significant financial impact requires many companies to have entire divisions dedicated to material integrity. Corrosion may also create safety issues. Many industrial incidents are the result of corrosion-related failures, which may lead to loss of life. For example, the major Bhopal disaster in India in 1984 that led to the loss of life may have been caused by a corrosion-related leak of water into a methylisocyanate tank (Hansson, 2011). While corrosion was not the only factor causing the Bhopal incident, it was a contributor. The large economic impact of corrosion, coupled with safety concerns, implies corrosion research is essential to determine knowledge leading to mitigation strategies.

In Saskatchewan, corrosion is a significant contributor to pipeline and equipment damage and failure in the potash industry (Strathdee, 1996). Potash is a potassium based mineral ore primarily used for fertilizer production and often spoken of in terms of potassium oxide (K_2O) equivalent – done so to compare different types of potash compositions (Wolfbauer, 1977). Saskatchewan has some of the largest deposits of naturally occurring potash in the World, measuring roughly one billion tons or almost a third of the world supply (Broughton, 2019). All potash producers have common problems regarding wear on their processing equipment and pipelines. In solution mines and within potash refining facilities, potash brine is typically transported using pipelines. Many brines being transported are typically a slurry of saturated potash brine with undissolved granules of potassium chloride crystals. Raw potash ore composition can vary depending on the site-specific geology. An example of common potash composition in Saskatchewan is approximately 38% potassium chloride (KCl), 59% sodium chloride (NaCl), 0.5% magnesium oxide (MgO), and 3% trace elements by mass (Huang *et al.*, 2005). It is well known highly concentrated chloride solutions, such as potash brine, can be extremely corrosive to many metals. Electrolyte composition and high process temperatures is a major contributor to corrosion in the potash industry. In addition, potash processing pipelines that contain a solid phase may increase pipeline wear as erosion becomes a dominant force causing material loss. Degradation of materials caused by flow or slurry flow of a corrosive

liquid is known as erosion-corrosion. Therefore, erosion-corrosion is a major concern for the potash industry.

Erosion-corrosion is the mechanical and electrochemical degradation of a material subject to the flow of a corrosive fluid or slurry (Malka *et al*., 2006). While erosion-corrosion of carbon steel will occur in the absence of a second phase, material loss is commonly enhanced by the addition of solids or gases into the electrolyte. Research has shown that erosion-corrosion has a more substantial effect on elbows and joints compared to straight pipe (Keating and Nesic, 1999). Erosion-corrosion targeting elbows and joints is likely due to the suspended phase and liquids dependence on impact angles to cause damage (Clark and Wong, 1995). Plainly, the amount of erosion-corrosion in a system would be the sum of erosion and corrosion independently; however, this is rarely the case. When erosion-corrosion occurs, the material loss is generally different than the sum of pure erosion and pure corrosion (Islam and Farhat, 2017). This phenomenon is referred to as erosion-corrosion synergy. Erosion-corrosion synergy is described as the interaction between erosion and corrosion and the effects they have on either accelerating or decelerating their respective mechanisms. Erosion-corrosion synergy may lead to additional wear not attributed to pure erosion and pure corrosion independently. Erosion-corrosion synergy can be both positive and negative.

Many environmental and operating parameters affect the severity of erosion-corrosion. These include parameters such as temperature, flow velocity, fluid composition, material type, and particle size/concentration, to name a few. Since erosion-corrosion is affected by many parameters that can be monitored or controlled in industrial processes, research into their effect on erosion-corrosion and erosion-corrosion synergy is beneficial. Insights into erosion-corrosion's mechanisms and how the individual components interact may lead to safer, more efficient, and more reliable infrastructure.

This thesis presents the effects various operating parameters such as flow velocity, slurry concentration, and slurry particle size have on the erosion-corrosion of AISI 1018 carbon steel elbows. Specifically, the experiments performed determine relationships between flow velocity, slurry concentration, and particle size to the corrosion and enhanced corrosion (synergy) experienced in a metal elbow during erosion-corrosion. The apparatus used was a vertical flow

loop containing a mixture of saturated potash brine and silica sand. From the research, an analytical method of determining the corrosion rate occurring inside the elbows was explored.

This thesis has five chapters. Chapter 1 is an introduction to this research. Chapter 2 presents the literature review that culminates in a statement of the knowledge gap and research objectives. Chapter 3 provides detail on the methodology, materials, and apparatus. Chapter 4 presents the results and discussion. Chapter 5 states the conclusions of the research.

2. Literature Review

2.1 Introduction

This section describes the literature of research in erosion-corrosion and the use of cathodic protection in erosion-corrosion experiments. This review provides a brief background of corrosion, erosion-corrosion, erosion-corrosion synergy, and cathodic protection (both generically and specific to erosion-corrosion). Also, previous experimental works related to this research are summarized and discussed. This review aims to expose any knowledge gaps found in the discussed erosion-corrosion research. From the knowledge gap, a hypothesis is stated.

2.2 Corrosion Overview

This section presents a discussion on the fundamentals of corrosion, including corrosion theory and corrosion measurement techniques.

2.2.1 Corrosion Theory

Metallic corrosion involves electrochemical reactions located at the surface of a metal substrate in contact with an electrolyte. Due to these electrochemical reactions, metal atoms will leave the metal lattice and dissolve into the electrolyte. Some of these dissolved species may undergo further reactions and precipitate back onto the corroding metal surface, in some cases forming rust. The electrochemical reactions that cause metallic corrosion form two categories: oxidation reactions and reduction. Oxidation and reduction reactions co-occur and work in unison. Oxidation reactions release electrons which are consumed in reduction reactions. In metallic corrosion, the oxidation reaction is generally the dissolution of the metal. The electrons released during metal dissolution are consumed by a reduction reaction, which varies depending on the aqueous environment. Oxidation and reduction reactions occur on surface regions called the anode and cathode respectively (Tro, 2008).

The electric potential is an indication of the thermodynamic driving force causing electrochemical reactions. The overall electric potential of an electrochemical reaction can be calculated from its component (half-cell) electrochemical reactions. Each half-cell reaction describes the reduction of a single species and its associated electric potential. Adding or subtracting the electric potentials of relevant half-cell reactions can provide the overall electric potential ($E°_{cell}$) of the electrochemical reaction formed from constituent half-cell reactions. Concerning corrosion, the larger the electric potential of the corrosion cell, the higher the driving force is that causes corrosion (Davis, 2000).

An example corrosion reaction involves the dissolution of iron (Fe) in water. In this example, there is an anodic region in which iron is dissolving and releasing electrons (oxidation), and a cathodic region where the electrons are consumed (reduction). Subtracting the reduction half-cell potentials of both the anode and cathode provides the overall electric potential of the corrosion reaction. The relevant reduction half-cell reactions and overall electric potential for iron corroding in water are shown in Eq. [2.1], [2.2], and [2.3]:

Cathodic Half Cell: $$O_{2(g)} + 2H_2O_{(l)} + 4e^- \rightarrow 4OH^-_{(aq)} \qquad E^\circ_{Cathode} = 0.40\ V \quad [2.1]$$

Anodic Half Cell: $$Fe^{2+}_{(aq)} + 2e^- \rightarrow Fe(II)_{(s)} \qquad E^\circ_{Anode} = -0.45\ V \quad [2.2]$$

$$E^\circ_{Cell} = E^\circ_{Cathode} - E^\circ_{Anode} = 0.40\ \text{V} - (-0.45\ \text{V}) = 0.85\ \text{V} \quad [2.3]$$

During corrosion, the electric potential created between the anode and cathode produces an electric current. The electric current produced is called the corrosion current. Often, the corrosion current between a single anode and cathode is difficult to measure experimentally. It is especially difficult in the case of uniform corrosion where the anodic and cathodic reactions are occurring at the same locations distributed over the substrate surface. To simplify oberservation, the corrosion current can be measured as the sum of current produced within the surface area corroding. This is called the corrosion current density, measured as the corrosion current per unit

surface area. Corrosion current density is often denoted as i_{corr}. Various testing methods can measure i_{corr} experimentally.

Corrosion rates can be calculated, and are best understood using Faraday's law. Faraday's law calculates the amount of iron (or any metal substrate) that dissolves into solution during corrosion. The general form of Faraday's law is shown in Eq. [2.4] (Chaudhari *et al.,* 2014):

$$w = \frac{itM}{ZF} \qquad [2.4]$$

where w is the mass loss of the substrate (grams), i is the corrosion current (amps), t is the time (seconds), M is the molecular weight of the substrate, Z is the number of electrons transferred, and F is Faraday's constant. Using i_{corr} in the above equation will provide the mass loss per unit area of the substrate. Faraday's law can be applied to any metal to determine the corrosion rate and is often used in conjunction with various measuring techniques.

2.2.2 Corrosion Measuring Techniques

Measuring i_{corr} is a standard method used in research to determine or define corrosion rates. Typically, i_{corr} is measured through various electrochemical tests performed by a potentiostat. Potentiostats can perform potentiodynamic scans (and various other scanning methods) to calculate the corrosion current density. Potentiodynamic scans utilize a 3-electrode setup consisting of a working electrode (WE), a counter electrode (CE), and a reference electrode (RE). The WE is generally the subject material, the CE is commonly an inert conductive material, and the RE is an electrochemical cell with a known potential used to measure electrochemical potentials in solution. During scans, a potentiostat allows the corrosion cell to reach the free corrosion potential (E_{corr}) before changing the potential of the system. The rate of change in potential is called the scan rate. During potentiodynamic scans, the potentiostat slowly increases the potential from a low cathodic potential to a high anodic potential. The data collected from potentiodynamic scans can be plotted in a Tafel plot as shown in Figure 2.1.

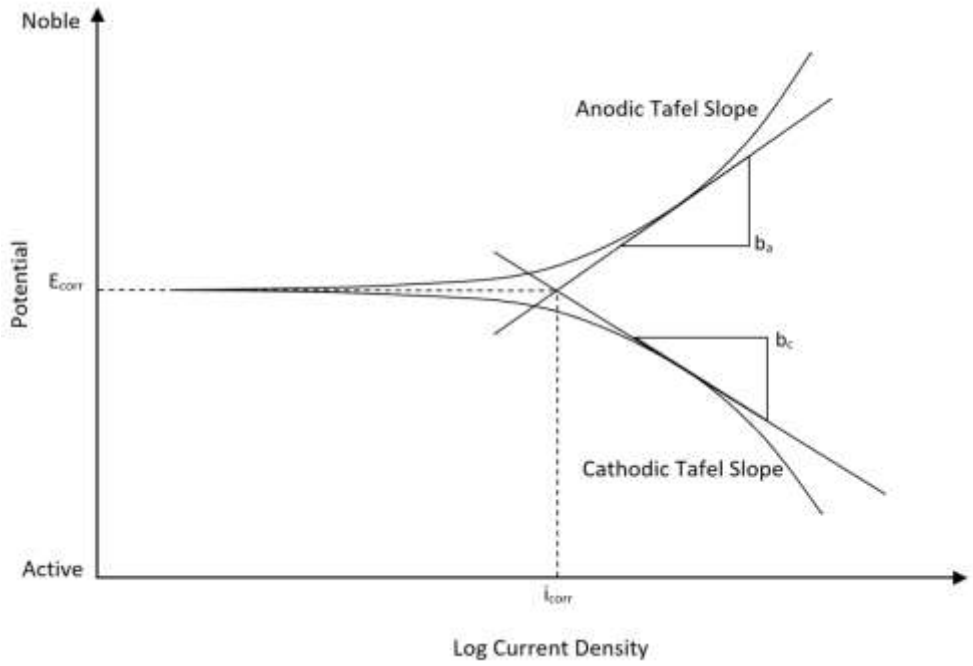

Figure 2.1. Example of a Tafel plot created from a potentiodynamic scan to determine i_{corr} as recreated from Anaee and Abdulmajeed (2016).

Figure 2.1 provides insights into how potentiodynamic scans are analyzed. From the plotted data, both the anodic and cathodic scans have tangential sloped lines placed on the inflection points. The two tangential lines should intersect at the free corrosion potential (E_{corr}). At the intersection, a vertical line may be drawn down to the x-axis. The point at which the vertical line intersects the x-axis is i_{corr}. The following equation describes the anodic and cathodic scan lines in Eq. [2.5]:

$$\eta = A \cdot \log \frac{i}{i_o} \qquad [2.5]$$

Where η is the overpotential (V) measured from E_{corr}, A is the slope of the Tafel line as depicted in Figure 2.1 by b_a and b_c, i is the measured current density at any point, and i_o is the exchange current density or i_{corr}. Tafel plots are a useful tool in corrosion research to determine corrosion rates by measuring i_{corr} and applying them to Faraday's law. One downfall of potentiodynamic

scans is their high sensitivity to operating parameters and need for specialized equipment. Therefore, this method is not used for all research applications or experiments.

A second corrosion measuring technique is by determining the mass loss of a sample that has been corroding for a set amount of time. Utilizing the mass loss method, a sample can be weighed before corrosion, placed in a corrosive environment for a set period of time, cleaned of all corrosion products, and then weighed again. The difference in the sample's mass before corrosion (M_i) and after being corroded for a set time (M_f) can be divided by the total time of immersion to calculate the corrosion rate, as shown in Eq. [2.6]:

$$Corrosion\ Rate = \frac{M_i - M_f\ (g)}{Time\ (hr)} \qquad [2.6]$$

Determining the corrosion rate through mass loss can be accurate; however, due to the slow rate of corrosion in many environments, it may often be time consuming. Measuring the corrosion rate of a single material in one environment may take days or weeks to allow sufficient mass loss from corrosion to occur. This method is useful when electrochemical measurements are difficult or perhaps impossible.

2.3 Erosion-corrosion Overview

Erosion-corrosion occurs when a metal surface is exposed to a flowing corrosive environment (Islam *et al.*, 2013). It is composed of both mechanical wear from erosion and the electrochemical dissolution of metal from corrosion. When erosion and corrosion coincide within piping or equipment, the material wear can be severe. During erosion-corrosion observation, the simple addition of each component rarely constitutes the total mass loss. In most cases of erosion-corrosion, the total mass loss experienced is found to be higher than the addition of corrosion and erosion processes independently. The additional mass loss observed is due to a synergistic relationship between erosion and corrosion and can be either positive or negative (Harvey *et al.,* 2007). Erosion-corrosion synergy is corrosion's effect on erosion mechanisms, and erosions effect on corrosion mechanisms (Jiang *et al.,* 1993). From this definition, mass loss

caused by erosion-corrosion synergy has two distinct parts: enhanced erosion and enhanced corrosion. Enhanced erosion is the additional erosion mass loss caused by corrosion mechanisms. Enhanced corrosion is the additional corrosion mass loss caused by erosion mechanisms. The mass balance equation of erosion-corrosion is shown in Eq. [2.7] and further expanded in Eq. [2.8] (ASTM Internationl, 1994):

$$EC = E + C + S \quad [2.7]$$

$$EC = E + C + (S_E + S_C) \quad [2.8]$$

where *EC* is the total erosion-corrosion, *E* is pure erosion, *C* is pure corrosion, *S* is synergy, S_E is enhanced erosion, and S_C is enhanced corrosion material loss all in units of grams (g). Through a series of experiments, erosion-corrosion and erosion-corrosion synergy mass loss can be quantified. Erosion-corrosion synergy research aims to explore and explain the mechanisms behind which erosion and corrosion interact.

Erosion-corrosion can occur on carbon steel during the single-phase flow of a fluid. The effect of erosion-corrosion generally increases with the addition of a second phase to the fluid. The second phase can be either a gas or solid. Any liquid mixture which contains multiple phases is called a slurry. Many slurries transported in the potash industry are solid-liquid mixtures. Solid-liquid slurries are heavily researched due to the severity of erosion-corrosion wear they produce. While erosion-corrosion will occur in all sections of pipe and equipment, targeted areas include joints, elbows, and valves (Keating and Nesic, 1999). These areas experience more severe wear as they cause the flow to change direction, speed, or pressure (Clark and Wong, 1995).

Many flow parameters and electrolytic properties affect erosion-corrosion. The parameters that cause significant changes to erosion-corrosion material loss include flow velocity, slurry concentration, abrasive particle size and shape, electrolyte composition, temperature, impact angle, and material properties (all of which will be discussed in subsequent sections). Individually, each parameter can be observed to determine its relationship to erosion-corrosion

and erosion-corrosion synergy. More detailed experiments may observe multiple parameters and their interactions on erosion-corrosion material loss.

2.4 Parameters that Influence Erosion-corrosion

2.4.1 Slurry Flow Velocity

Slurry flow velocity can affect erosion-corrosion material loss both mechanically and electrochemically. Mechanically, increasing flow velocity will increase the velocity of suspended particles. Higher velocities will raise the kinetic energy of each particle. The additional kinetic energy may translate to more significant erosion mass loss from impingement and micro-abrasions (Wang and Stack, 2000). A higher flow velocity may also increase the number of impingements occurring per unit time on pipe or equipment walls. A greater number of particle impingements may increase wear from erosion mechanisms.

Electrochemically, flow velocity will affect the mass transfer of corrosion reactants and products between the electrolyte and metal surface. Increasing mass transfer rates of solutes may increase or decrease corrosion depending on the metal and solute type. Experiments have shown that increasing flow velocity corresponds to faster rates of oxygen diffusion from the bulk fluid to the metal surface (Zheng *et al*., 1995). In passive metals, faster diffusion of oxygen may increase rates of re-passivation, which could reduce the conventional corrosion experienced. Alternatively, faster repassivation rates and ample oxygen diffusion may create thick oxide films that are less adherent to the surface, or less adherent to themselves (Abd-El-Kader and El-Raghy, 1986). These thicker, less adherent films are vulnerable to erosion. For non-passivating metals, the increased rate of oxygen diffusion will expedite corrosion. In a study performed by Wang and Stack (2000), the relationship of flow velocity on both erosion and corrosion rates for various steels is discussed (Wang and Stack, 2000). The results of Wang and Stack's study is shown in Figure 2.2 (a) and (b). From the study, it is evident that all three metals experienced an increase in erosion mass loss from increasing flow velocity. Passive metals tended to resist additional corrosion from increasing flow velocity in comparison to carbon steel.

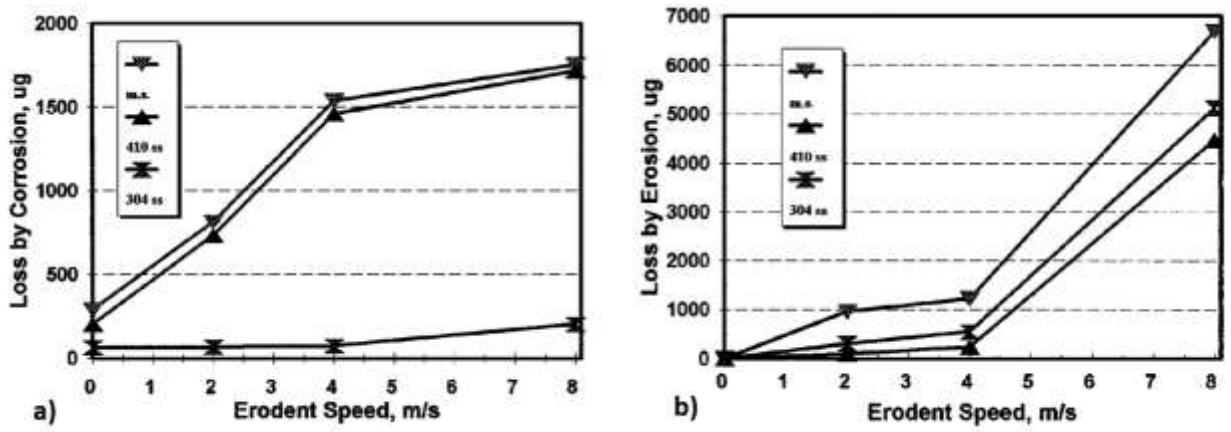

Figure 2.2. (a) The effect of slurry flow velocity on corrosion rates of various common steels, (b) The effect of slurry flow velocity on erosion rates of various common steels – reproduced from Wang and Stack (2000) with permission from Springer.

Research produced from Guo *et al.* (2005) has shown there may exist a critical flow velocity where the increased mass transport of corrosion products and reactants no longer increases corrosion (Guo *et al.*, 2005). The critical velocity implies there may be a mass transfer rate ceiling of oxygen. At the ceiling, the diffusion of oxygen as a reactant is no longer the rate-determining step in the corrosion reaction. At the critical flow velocity, the speed of the corrosion reaction becomes the rate-determining step.

2.4.2 Particle Shape and Size

Particle shape and size both affect erosion-corrosion material loss. Larger, sharper particles have been shown to erode metal surfaces quicker than smaller, rounded particles (Guo, 2006). Similar to the effect of flow velocity on erosion-corrosion, it has been theorized that particles may only increase erosion-corrosion material loss up to a specific size. In a report written by Oka and Matsumura (1983), various materials were put under erosion-corrosion while increasing particle size (Oka and Matsumera, 1983). The study showed that particles above 100 µm showed a plateau in erosion rates on nylon and carbon steel. This trend was assumed to be from the erosion of the abrasive particle itself. Larger particles naturally erode into smaller, less erosive particles. The relationship between particle size and erosion-corrosion material loss is complicated and

based on a concept called collision efficiency (Rajahram *et al.*, 2009). Collision efficiency is the relationship between the number of impingements per unit area per second and the energy of each particle impact. Given a set slurry concentration, as particle size decreases, the number of impingements increase and the kinetic energy of each impact is lower. Conversely, an increase in particle size leads to fewer impacts, but larger kinetic energies. The mechanism of collision efficiency suggests there is a particle size where erosion-corrosion mass loss peaks from balancing each particle's kinetic energy and the number of impingements occurring.

In many cases, larger particles lead to higher erosion-corrosion rates from robust stripping of corrosion films revealing bare metal (Song and Du, 2017). However, the complicated relationship between erosion-corrosion and particle size is still not fully understood. In a study performed by Clark and Hartwich (2001), the effect of particle size on erosion-corrosion rates was experimented. The research concluded that particle size effects on erosion-corrosion material loss could only be understood if the effect of particle size on the hydrodynamics of slurry flow is known. This conclusion suggests that the hydrodynamics of slurry flow may be required to understand the relationship between erosion-corrosion and particle size.

The hardness of abrasive particles may also influence erosion-corrosion material loss. Experiments have estimated particles approximately 1.2 - 1.5 times harder than the metal surface will induce the most substantial erosion-corrosion material loss (Hutchings, 1986). This occurs as harder materials naturally erode softer materials through more efficient energy transfer during impacts.

The composition of the particle, which may relate to hardness, is also an important parameter in erosion-corrosion studies. The composition of the particle may cause contact corrosion on the impingement surface. Contact corrosion occurs when the particle is metallic and nobler than the metal being impinged (Qi *et al.*, 2011). Contact corrosion is fast, galvanic corrosion that occurs between dissimilar metals when connected electrically. Under high loading conditions of metallic particles, contact corrosion may increase the rate of erosion-corrosion noticeably.

2.4.3 Material Properties

Material selection is an essential factor in erosion-corrosion prevention. Important material properties concerning erosion-corrosion include hardness, ductility, passivity, and carbon

content. Hardness and ductility are related as most ductile metals lack hardness. Metal hardness commonly affects erosion material loss. The harder the metal, the more erosion-resistant the metal becomes (Guo, 2006); an observation further verified by Wang *et al.* (2000). Erosion wear may increase on ductile metals as the bonds holding the metal together are weaker. Ductile metals typically flake from impingement and particle ploughing. When ductile metals are impinged, the impact crater may have large jagged lips which are further susceptible to erosion and corrosion (Rajahram *et al.*, 2011).

A metal's ability to passivate also affects its resistance to erosion-corrosion. Passive metals develop outer films that resist corrosion by restricting oxygen to the bare metal, having low(er) conductivity, and providing a barrier to the release of ions (Cao *et al.*, 2015). Experimentation has shown that metals which form passive films are more resistant to erosion-corrosion than those that do not (Wang and Stack, 2000). Metals that form strong adhering passive films can outperform harder metals that do not have passive films from erosive and corrosive material loss. Many passive steels significantly lower the rate of erosion-corrosion material loss from eliminating corrosion and enhanced erosion (Matsumura *et al.*, 1991).

The carbon content of steel may also increase resistance to erosion-corrosion. An increase in carbon content generally relates to the hardening of steels. In a study performed by Xie *et al*. (2015), various steels with different carbide contents were placed in erosive conditions. The results displayed that metals with high levels of carbide performed better during erosion. The superior erosion resistance occurred from the difference in hardness between the carbide (1350-2500 HV) and the standard silica erodent (100 HV). However, high carbide levels may also increase corrosion at grain boundaries (Zheng *et al.*, 2000). Therefore, a compromise to minimize erosion-corrosion material loss should be explored between carbon content resisting erosion wear and its effect on increasing corrosion at grain boundaries.

2.4.4 Environmental Conditions

For most materials, increased acidity corresponds to higher corrosion rates (Watson *et al*., 1995). In regards to erosion-corrosion, increased acidity could correspond to more substantial material loss. As corrosion can cause enhanced erosion, increasing acidity may also increase erosion

rates. A study performed by Batchelor and Stachowiak (1988) on mild steel found that while high acidity will increase corrosion rates, the effect of acidity on erosion and corrosion combined causes more significant material loss (Batchelor and Stachowiak, 1988). Batchelor and Stachowiak's findings suggest that erosion-corrosion reacts more severely to a change in pH than undisturbed corrosion alone. The severe erosion-corrosion material loss occurring in more acidic solutions may be caused by acidity increasing erosion-corrosion synergy.

Temperature can also affect erosion-corrosion material loss. An increase in temperature can raise the kinetics of the corrosion reaction and the ductility of the metal. Table 2.1 shows the temperature dependence of erosion-corrosion on A514 carbon steel, 316 stainless steel, and REM 500 low alloy steel in a study performed by Madsen (1988). Madsen's results showed as the temperature of the solution increased, erosion-corrosion wear increased by as much as 30%. At extremely high temperatures, the kinetics of passive film formation may also increase, creating thick oxide layers that quickly erode (Stack *et al.*, 1993). These results suggest that although high temperatures may protect passive metals from additional corrosion due to fast re-passivation rates, the weakly bonded oxide films may increase erosion wear.

Table 2.1. Temperatures effect on the wear rate of A514 steel, 316 stainless steel, and REM 500 from 26 °C to 60 °C *(Madsen, 1988)*.

Alloy Type (Flow Velocity)	Wear Rate (mm^3h^{-1})	
	26 °C	60 °C
A514 Carbon Steel		
15.6 ms^{-1}	28.12	35.68
5.8 ms^{-1}	0.494	0.722
316 Stainless Steel		
15.6 ms^{-1}	31.32	39.34
5.8 ms^{-1}	0.781	0.802
REM 500		
15.6 ms^{-1}	16.56	21.58
5.8 ms^{-1}	0.339	0.589

A fluid's composition has also affects erosion-corrosion. Passive films are easily penetrated and broken in the presence of chloride ions (Elfstrom, 1980). Caution should be displayed when

choosing the material of pipes carrying high concentrations of chloride salts. When chlorides are present, passive metal alloys should be avoided altogether.

The dissolved oxygen (DO) content contained within fluids or slurries may also affect the erosion-corrosion experienced. In a study performed on low carbon En30B steel, the total erosion-corrosion and erosion-corrosion synergy increased significantly with higher levels of DO (Jiang *et al*., 2017). Higher DO content increased the corrosion rate by providing ample corrosion reactants. In flow systems that are erosion dominated, an increase in mass loss from corrosion alone may be negligible. However, the increase in corrosion from DO also increased the erosion wear due to synergistic mechanisms. The elevated levels of material loss caused by DO were mainly from an increase in the enhanced erosion experienced.

2.4.5 Slurry Concentration

Slurry concentration can affect erosion-corrosion material loss and synergistic mechanisms. Slurry concentration is the number of solids contained in solution and is measured in percentage by mass or volume. As a general trend, an increase in slurry concentration can elevate the amount of erosion-corrosion experienced by a metal (Rajahram *et al*., 2011). Higher solids concentrations increase erosion material loss as greater numbers of particles can impinge the metal surface. Studies have shown that there may exist a critical particle concentration in which erosion no longer increases for certain metals (Rajahram *et al*., 2011). At this critical concentration, the particles may protect the metal from further impingement. This phenomenon occurred from particle-particle interactions occurring in the slurry, which decreased kinetic energy and varied impingement angles. In a study performed by Hutchings (1986) on carbon steel, the relationship between slurry concentration and erosion mass loss was explored. Hutchings found that carbon steel in slurry concentrations over 12 vol.% experienced a slowing erosion rate, which no longer increased linearly with slurry concentration (Hutchings, 1986). At slurry concentrations past 30 vol.%, erosion was shown to stop increasing altogether. Elevated slurry concentrations may also cause the erosion of the particles themselves into less erosive entities, which may cause the phenomenon shown in Hutchings' research.

Corrosion also has a relationship with slurry concentration. As slurry concentration increases, so do the corrosion kinetics, as seen by a negative shift in the open-circuit potential of a metal (Xie *et al*., 2003). The negative open-circuit potential shift during erosion may be caused by corrosion preferentially attacking work-hardened metal caused by particle impingement. At low slurry concentrations, passive metals have been shown to outperform non-passive metals with corrosion mass loss (Hussain and Robinson, 2007). This result occurs as the smaller number of particle impingement's at low slurry concentrations leaves ample time for repassivation of the surface. Generally, fast repassivation rates lead to lower corrosion rates. In instances where the passive film is harder or more durable than the base metal, fast repassivation may also protect from erosion material loss. As slurry concentration increases with less time between successive impingements, the rate at which a metal can repassivate becomes vital for the material's ability to resist erosion-corrosion material loss.

Erosion-corrosion material loss involving slurry concentration is also complexly dependent on flow velocity. The relationship between flow velocity and slurry concentration can be mapped for materials to show which regions are dominated by either erosive or corrosive mechanisms. Detailed slurry concentration mapping for mild steel was performed in experiments by Stack *et al.* (2003). Stacks results showed there was a complex relationship between slurry concentration and flow velocity on the mechanisms driving erosion-corrosion. The study showed at low velocities and low slurry concentrations, the material loss was corrosion dominated. Slurry concentration had a more substantial overall effect on erosion-corrosion material loss when kept low and during high flow velocities.

2.4.6 Impact Angle

The effect of impact angle on erosion-corrosion wear may lead to regions on infrastructure with localized material loss. The local material loss could occur where the impact angles are such that maximum wear occurs. Local erosion-corrosion material loss can be a significant cause of pipeline or equipment failure and is essential to monitor or prevent if possible.

Erosion-corrosion material loss is dependent on the angle at which both the fluid and solid particles impact the metal surface. The effect of impact angle on erosion-corrosion explains how

elbows, joints, and valves exhibit high levels of material loss in comparison to straight pipe lengths (Keating and Nesic, 1999). Pipe contractions and expansions may also affect erosion-corrosion material loss. The increase in erosion-corrosion rates from pipe contractions or expansions occurs from a change in the flow regime at these locations. As flow regimes change, local eddies form, which can affect the impact angle of the solids and fluid on pipe walls (Woods and Jones, 2003). The effect of impact angle on erosion-corrosion is also dependent on the type of material. Ductile materials and brittle materials exhibit different behaviour when subject to the same impact angles (Clark, 2002). Figure 2.3 shows the difference in erosion wear mechanisms associated with brittle and ductile materials. From the schematic, it is evident that brittle materials experience considerable wear at higher impact angles closer to 90° (deformation wear). Ductile materials experience more substantial wear at shallower impact angles (cutting wear). The difference in wear mechanisms occurs from a brittle material's tendency to fracture and break off from blunt impacts. In contrast, ductile materials exhibit wear from low angle ploughing, which creates craters and troughs.

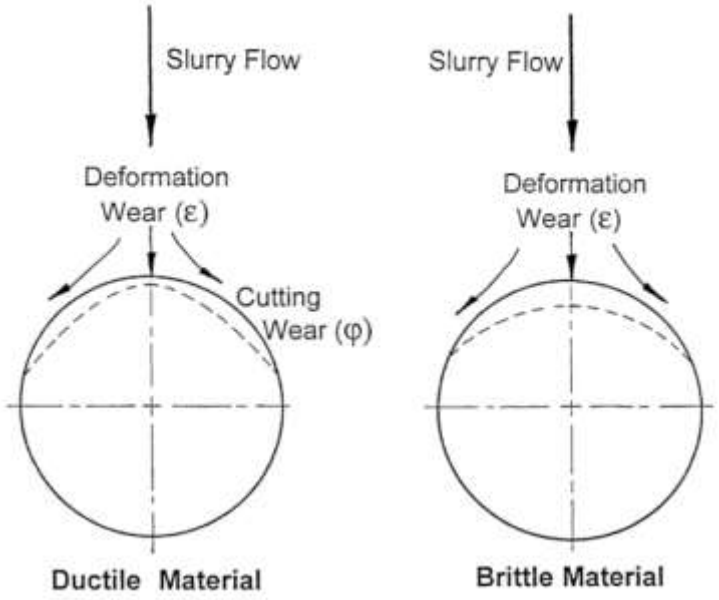

Figure 2.3. Difference in wear mechanisms and patterns between ductile and brittle materials in slurry flow – reproduced from Clark (2002) with permission from Tribology International.

In a study performed by Hutchings (1987) on flat specimens, ductile metals displayed the highest wear at shallow angles between 20° to 30°. Conversely, the same study found ceramics (being harder and more brittle than most metals) showed elevated wear from impacts on the normal plane (90°). Similar results occurred regardless of using a solid or gas as the second phase. Additionally, many stainless steels have been shown to behave similarly to ductile metals showing the highest degradation at shallower impact angles (Andrews *et al.*, 2014). Figure 2.4 shows the general effect of impact angle as displayed on carburized and non-carburized low alloy AISI 5117 steel in various solutions. It is evident from Figure 2.4 the most extensive material loss occurred at a median angle, showing characteristics of both ductile and brittle behaviour. This suggests that materials can experience maximum material wear at many different impact angles between 0° to 90° and are not limited to shallow or acute impacts.

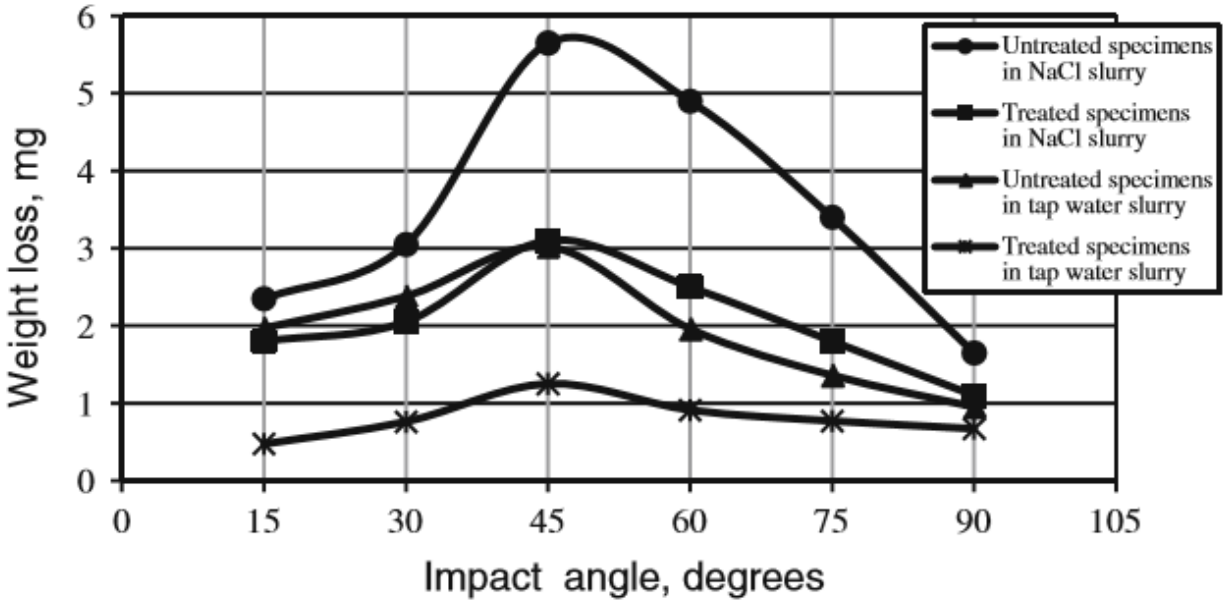

Figure 2.4. Effect of impact angle on the erosion-corrosion of treated and untreated AISI 5117 steel in tap water and NaCl brine slurries - reproduced from Saleh and Ahmed (2013) with permission from Springer Nature.

2.5 Erosion-corrosion Synergy

When erosion and corrosion interact in flow systems, a synergy exists between them. The synergy between erosion and corrosion can cause their respective mechanisms and material loss to change. Erosion-corrosion synergy can result in additional material loss or, in rare cases, less material loss. Erosion-corrosion synergy is composed of two parts: enhanced corrosion and enhanced erosion. Enhanced corrosion is corrosion material loss that varies from the pure corrosion that occurs in the absence of erosion. Similarly, enhanced erosion is erosion material loss that varies from the pure erosion that occurs in the absence of corrosion. Therefore, the interaction between erosion and corrosion may act to *enhance* each other, either positively or negatively.

2.5.1 Enhanced Corrosion

Enhanced corrosion is material loss caused by erosion accelerating or decelerating corrosion mechanisms. During single or two-phase flow, carbon steel will undergo erosion-corrosion. When erosive forces exist, the material loss caused by corrosion on carbon steel is usually enhanced. Enhanced corrosion researched is performed often, but the mechanisms driving enhanced corrosion are not well defined.

Enhanced corrosion is the by-product of several phenomena caused by mechanical erosion. Erosion during slurry flow will roughen the surface of the metal by creating pits, fibrous surface textures, and craters through impingement. The additional surface area created by erosion intensifies the local electric field of the metal, especially at the tops of craters (Wang and Stack, 2000). The stronger electric field may act to increase the corrosion experienced by the metal. Surface films, even non-passive, protect the metal surface in many ways including limiting the mass transfer of oxygen to the metal surface (Wang and Stack, 2000). For weakly passive metals, impingement can strip the passive film protecting the metal, exposing a clean surface for corrosion to occur on. Non-passive metals may also experience higher corrosion rates from erosion mechanically removing corrosion product films or scaling.

Constant impingement on the surface of the metal may also cause elastic and plastic deformations known as the strain effect. From the strain effect, surface impacts cause dislocations in sub-structure deformation bands and emerging slip steps. These dislocations can increase the active anodic sites on the metal, thereby increasing corrosion material loss (Xie *et al.*, 2003). The strain effect in mild steels occurs from the ridges and troughs created from plastic deformation of the metal surface during erosion. The ridges and troughs create corrosion cells, which increase the corrosion rate (Noel and Ball, 1983). Corrosion cells develop from the high instance of dislocations found in metal ridges compared to valleys or troughs. The dislocations in metal substructures are relatively anodic while the low trough regions become cathodic. Similar to the strain effect, the chemo-mechanical effect states that corrosion dissolution rates are higher in metals subject to high stress/strain loads (Guo H. , 2006). High stress/strain loads in metals commonly occur from particle impingements. Impingements from erosion can also cause sub-surface cracks in the metal. Cracks can act as initiation sites for corrosion to occur and elevates the reaction kinetics (Islam, 2017).

The effect of *shot peening* has been found in metals experiencing high rates of impingements from the addition of a second phase (Wood and Hutton, 1990). Shot peening can act to work-harden the metal surface which may provide additional erosion resistance. In highly corrosive environments, corrosion may preferentially attack the work-hardened metal due to high strain loads held within the metal structure (Wang and Stack, 2000). Therefore, in cases where shot peening occurs, corrosion material loss may increase as it dissolves the work-hardened metal.

Many mechanisms of enhanced corrosion are directly associated with the mechanical interaction of erosion on the metal surface. However, there are other properties of erosive flow that increase corrosion material loss. During slurry flow, solid or gas particles become suspended in the fluid. Each particle may act as a fluid agitator during turbulent flow. The increased fluid agitation caused by particles may augment the mass transfer of corrosion products and reagents to and from the pipe wall (Guo, 2006). The increase in the mass transfer of oxygen and corrosion products may shift the corrosion reaction forward.

2.5.2 Enhanced Erosion

Enhanced erosion is material loss caused by corrosion accelerating or decelerating erosion mechanisms. Many mechanisms that cause enhanced erosion are from corrosion altering the mechanical properties of a metal. Corrosion product films and passive films are usually less adherent and weaker than bare metal surfaces (Wang and Stack, 2000). Weak films may be more easily removed by erosion compared to pure metal. As discussed in Section 2.4.3, as the hardness of a material decreases, their resistance to erosion generally declines accordingly. Corrosion may deform and dissolve the work-hardened surface of metals, in some cases preferentially over ductile surfaces (Wang and Stack, 2000). Removal of the work-hardened outer layer from corrosion may expose less dense metal which is more susceptible to erosion.

Recent experiments designed apparatuses to observe the effect anodic current had on the hardness of metals. Two separate studies by Guo *et al.* (2005) and Lu and Luo (2006) both found consistent results that increasing the anodic current will decrease the hardness of a metal. Anodic current is representative of the current produced by a corrosion cell. Therefore, corrosion may cause a decrease in metal hardness which could ultimately increase the erosion material loss. Figure 2.5 shows the decreasing-linear relationship anodic current had with metal hardness. It should be noted that the observed decrease in metal hardness was only applicable to the thin layer on the surface that is actively corroding.

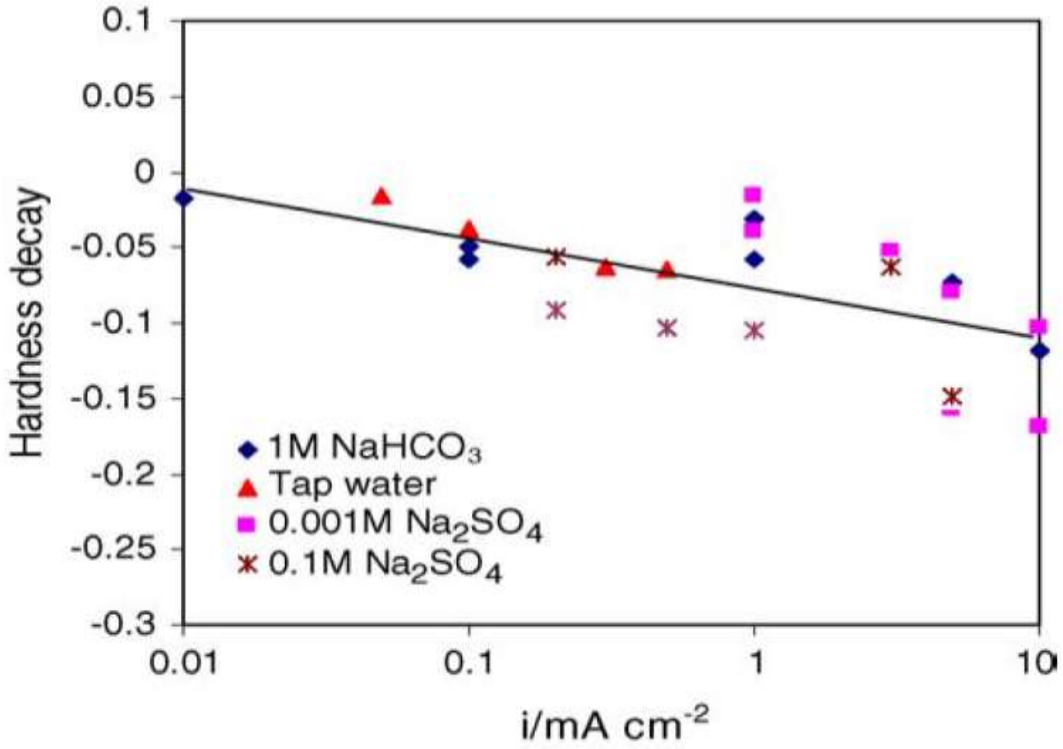

Figure 2.5. Hardness decay of steel in various solutions with increasing anodic current density – reproduced from Guo et al. (2005) with permission from Elsevier.

Corrosion has also been found to attack grain boundaries in many metals but prefers alloys with multiple phases (Wood and Hutton, 1990). Grain boundaries can be highly active anodic sites depending on the nobility difference of each phase. The preferential corrosion of grain boundaries can lead to grain loosening, which may cause entire grains to detach by erosive forces. Erosion of a metal surface is also sensitive to the impingement angle. Roughening a metal surface from corrosion can alter the striking angle to become more acute, thus transferring more energy to the metal (Guo H. , 2006). Corrosion that creates surface roughness may increase erosion material loss as the fluid or slurry impacts the surface. Localized corrosion occurring on crater lips can also weaken a metals adherence to the surface, creating flakes that are easily removed by erosive slurry flow (Wang and Stack, 2000).

2.6 Cathodic Protection

2.6.1 Cathodic Protection Overview

Cathodic protection is a well-known mitigation strategy used to inhibit corrosion since the 1950s (Kean, 1981). Cathodic protection has also been used in many erosion-corrosion experiments to quantify pure erosion material loss, or as a method to reduce erosion-corrosion wear. Cathodic protection operates by lowering the electric potential of the corroding material such that the anodic corrosion reaction (the dissolution of metal) does not occur. The potential is lowered by applying an electric current through the metal. The current applied to the metal creates a blanket of electrons on the surface. With ample electrons available on the surface, the anodic reaction that dissolves metal no longer occurs on the structure protected. Instead, the protected structure acts as a cathode where reduction reactions take place – hence *cathodic* protection. Cathodic protection commonly protects pipelines, process tanks, railroads, and rebar from corrosion.

Pourbaix diagrams describe electrochemical reactions in terms of corrosion cell potential and acidity. Pourbaix diagrams depict how a metal may react given a specific pH and corrosion cell potential. An example Pourbaix diagram of iron corroding in water is shown in Figure 2.6 and can display how cathodic protection inhibits corrosion.

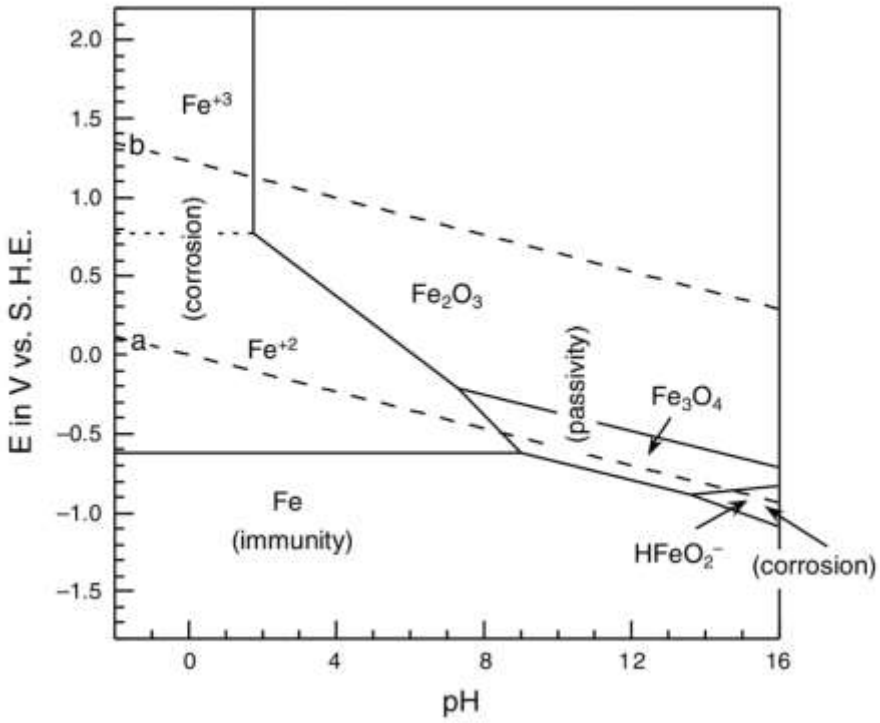

Figure 2.6. Pourbaix diagram of iron in water for pH from 0 to 16 at 25°C – reproduced from McCafferty (2010) with permission from Springer Nature.

In Figure 2.6, the y-axis is the corrosion cell potential (V), and the x-axis displays pH. When placing a metal in a solution, the potential of the corrosion cell and pH will define which region (corrosion, passivity, immunity) the metal is within. From the above Pourbaix diagram, if the corrosion cell potential is between 0.0 and -0.6 V_{SHE}, iron should actively corrode in water. During cathodic protection, the potential of the corrosion cell is lowered. If decreased sufficiently, a metal may enter the immunity region in which corrosion becomes inhibited. In the above Pourbaix diagram, lowering the potential of iron in water below -0.6 V_{SHE} places the iron into its immunity region depicted by the area labelled *"*Fe*"*. In the immunity region, the reaction on the iron surface is purely cathodic and stays in a solid-state.

The accepted corrosion cell potential that ensures steel is adequately protected (E_{prot}) is -0.85 V_{CSE} (Applegate, 1973). The value of -0.85 V_{CSE} has been determined through the practical application of cathodic protection in structures while observing the corrosion behaviour. However, lower potentials may be required depending on the corrosion environment and metal type.

During the application of cathodic protection, lowering the potential too far can cause the metal to be over-protected, and may be detrimental to the metal. Over-protection may cause disbonding of protective coatings or excessive hydrogen evolution leading to embrittlement (Byrne *et al.*, 2015). The current density required to lower the potential of most steels to -0.85 V_{CSE} is commonly between 1-20 mA/ft^2 for external protection of buried structures (Bosich, 1970). The amount of current density supplied to the protected structure depends heavily on the resistance of the environment surrounding the metal. Structures with thick, highly resistant coatings require less current density to achieve protection than a structure with no coating. Similarly, metals with highly resistant passive films require lower current density for protection. Over long periods, the amount of current required to protect a structure may decrease due to the applied amperage causing polarization. Polarization is a barrier that forms over the metal surface that provides resistance to corrosion (Davis, 2000).

Cathodic protection is commonly implemented using two methods. The applied current can be provided using a sacrificial anode or using an inert anode with a power source (otherwise called impressed current cathodic protection). The following section(s) describe both methods.

2.6.2 Cathodic Protection from Sacrificial Anodes

A sacrificial anode is a material that is less noble than the material being protected and will corrode preferentially (Eyres and Bruce, 2012). Sacrificial anodes work by being placed in the same electrolyte as the structure in need of protection. The sacrificial anode and structure are electrically connected using a cable. Once connected, the electrons produced from the dissolution of the sacrificial anode transfer to the structure. The excess electrons lower the potential of the structure such that corrosion is inhibited. The sacrificial anode will eventually be consumed to feed the reduction reactions occurring on the protected structure. The consumption of the anode is why it is deemed *sacrificial*. Sacrificial anode protection is commonly called galvanic protection as the mechanisms mimic that of galvanic corrosion. Figure 2.7 shows a typical schematic of cathodic protection using a sacrificial anode.

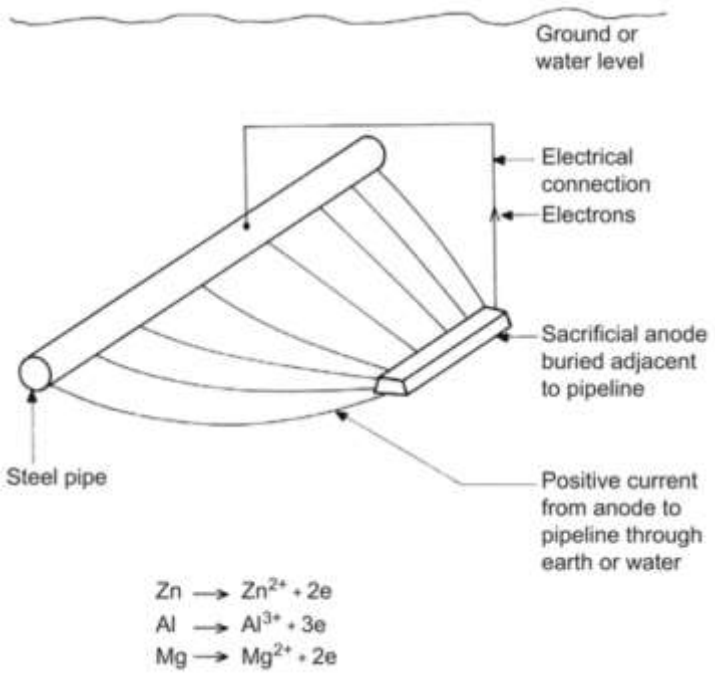

Figure 2.7. Schematic diagram of cathodic protection on a buried pipeline using a sacrificial anode – reproduced from Bahadori (2014) with permission from Elsevier.

Sacrificial anodes are commonly metals such as zinc, magnesium, or aluminum (Applegate, 1973). All sacrificial anodes have half-cell potentials larger than the metal they are protecting. When coupled electrically with iron, the sacrificial anode will corrode in place. Sacrificial anodes are sized based upon the amount of current required to protect the structure and the protection period. Materials such as zinc and magnesium have a known amount of chemical potential energy, measured in amp-hours per pound, that is released once coupled with iron. Large masses of sacrificial materials may become expensive if the load requirement of the protected structure is high. Sacrificial systems commonly protect smaller, more regional structures such as tanks and ground equipment. These structures have lower current requirements and benefit from the versatility of anode placement.

2.6.3 Impressed Cathodic Protection with Inert Anodes

Impressed cathodic protection systems work similarly to galvanic systems. Instead of a sacrificial material that releases electrons, electrons are supplied by an external power source

such as a generator. Impressed systems still require an anode placed near the protected structure to complete an electric circuit. The anodes used in impressed systems are generally inert, but electrically conductive materials. An inert anode provides longevity of protection as the anode does not degrade quickly. Inert anodes are often materials such as graphite or high-silicon cast iron (Bryne *et al.*, 2015). While graphite anodes are corrosion resistant, over time they react with oxygen from the high positive potential at the anode creating carbon dioxide. The graphite anode oxidation process is slow from the high energy capacity of the graphite measured in amp-hours per pound. Compared to sacrificial anodes such as zinc or magnesium, graphite has over ten times the chemical energy capacity and lasts longer (Applegate, 1973). Figure 2.8 shows a generic schematic of an impressed cathodic protection system.

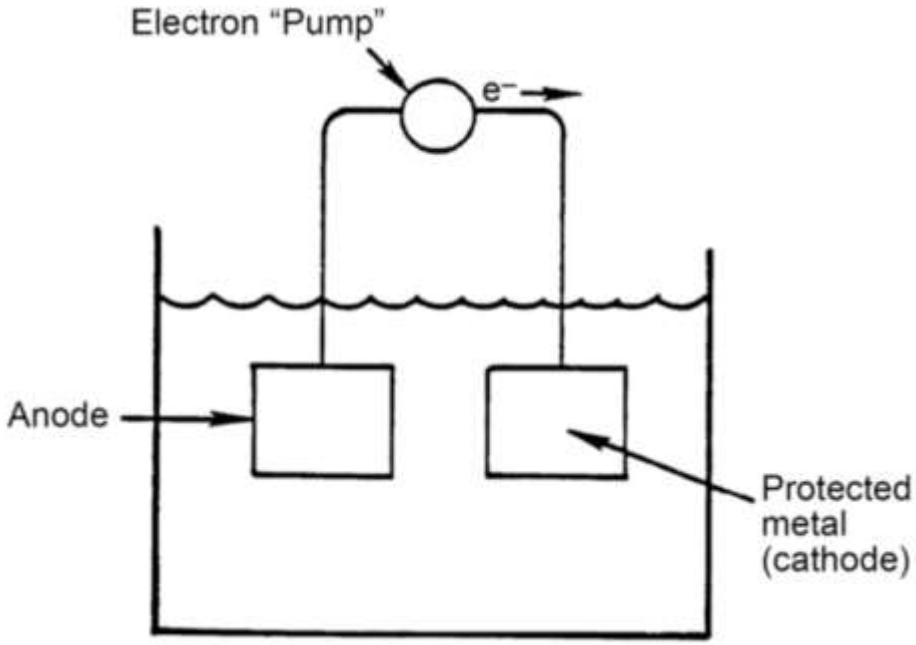

Figure 2.8. Schematic of an impressed cathodic protection system on a buried pipeline using an inert anode and external power source - reproduced from Bahadori (2014) with permission from Elsevier.

Impressed cathodic protection provides the user with increased flexibility. Over time, as the power requirement of the structure decreases from polarization, the load of the DC power supply can be reduced to save costs. The supplied current may also be adjusted using impressed systems

depending on the structure-to-electrolyte potential measured to ensure adequate protection. The use of substantial power sources and inert anodes makes impressed cathodic protection efficient for protecting large structures with significant load requirements. Impressed systems commonly protect pipelines and industrial facilities due to the high current required and amount of exposed surface area.

2.7 Previous Works

2.7.1 Works Related to Cathodic Protection in Erosion-Corrosion Studies

Cathodic protection is a common mitigation strategy used industrially to inhibit corrosion on equipment and structures. The same technique can be applied in laboratory research to inhibit corrosion in erosion-corrosion experiments. While many researchers have used cathodic protection in erosion-corrosion studies, its uses are limited. The following literature explores the use of cathodic protection in erosion-corrosion studies.

Madsen (1988) used cathodic protection to study and quantify the pure erosion and erosion-corrosion synergy occurring on stainless steels using a slurry-wear test apparatus. It was found that the erosive removal of passive films from the metal surface significantly increased the corrosion experienced on stainless steel. Similarly, Yao *et al*. (1995) used cathodic protection to study pure erosion, erosion-corrosion synergy, and as a method to reduce erosion-corrosion material loss. The experiments used AISI 321 stainless steel in an acidic slurry. The study suggested that cathodic protection was a viable method to reduce erosion-corrosion wear from the suppression of corrosion and enhanced erosion. In addition, Yao observed the hydrogen evolution created during cathodic protection reduced erosion wear from creating a gas cushion on the metal surface. Whether or not hydrogen evolution caused any embrittlement in the stainless steel was not addressed. Wang *et al*. (2005) used cathodic protection on BS080A15 steel samples in a rotating cylinder electrode (RCE) slurry pot tester. The experiments aimed to determine if cathodic protection was a comparable method to corrosion inhibitors in reducing erosion-corrosion material loss in low slurry concentration environments. Experiments showed a 95% reduction in mass loss with the application of cathodic protection and performed better than

corrosion inhibitors. The experiment displayed a possible use for cathodic protection to reduce erosion-corrosion wear.

The effect of flow velocity on erosion wear was determined by Zheng *et al*. (2000) by applying cathodic protection to stainless steel samples in an acidic-sand slurry. Results showed that flow velocity increased the rate of erosion from a greater number of high energy impingements. Zheng's research also stated that the reduction of corrosion using cathodic protection could limit erosion-corrosion mass loss by decreasing synergistic effects. Lu and Luo (2006) used cathodic protection on AISI 1018 carbon steel samples in a modified RCE slurry pot tester to study the effects of corrosion on erosion wear. The experiments found that corrosion significantly increased the rate of erosion from chemo-mechanical (synergistic) mechanisms. Lorenzi *et al*. (2016) studied the use of cathodic protection to inhibit corrosion on fully submerged AISI 304 stainless steel ship propellers as they undergo rapid erosion-corrosion in chlorinated seawater. Both impressed and sacrificial anode systems were tested for their viability. The results were modelled and displayed how the structure-to-electrolyte potential changed along the propeller shaft. The study did not mention if cathodic protection would be an economical option in reducing erosion-corrosion on the propellers.

While cathodically protecting the inside of pipelines is rare due to high throwing power, cost, and design limitations - its possibility as a corrosion mitigation strategy has been explored. In a study performed by Morgan (1959), cathodic protection on the inside of pipes carrying seawater was experimented. Observation showed that increasing flow velocity elevated the amount of current density required to protect the pipe. Additional tests showed at a greater distance from the anode, the structure-to-electrolyte potential of the steel increased. This trend matches the potential attenuation in conventional cathodic protection of buried structures. Detailed descriptions of the in-situ anode/reference electrode placements were also provided. Ultimately, the research concluded that cathodic protection alone is uneconomic to protect the inside of a pipe without a coating. While Morgan found protecting the inside of a pipe uneconomical, the ability to protect the inside of a pipe using impressed cathodic protection was shown to be possible.

The use of cathodic protection to study erosion-corrosion synergy on a sliding wear apparatus was performed by Wang *et al.* (2015). Experiments were performed on QT100 steel in

chlorinated sand-water slurries. The study found that enhanced erosion increased as slurry corrosivity increased. Furthermore, enhanced corrosion was inversely proportional to the sliding speed (erosive velocity). The research concluded that cathodic protection offered a viable means of observing erosion-corrosion synergy and pure erosion material loss. Experiments performed by Yang and Swisher (1993) explored the concept of cathodically protecting common hard alloys from erosion-corrosion in seawater-sand slurries. High hardness copper, steel, and titanium alloys were all tested while placed under cathodic protection. Experiments used 3.5 wt.% NaCl brine in a slurry pot apparatus modified for electrochemical measurements. Silica sand was added at 9 vol.% for erosion-corrosion experiments. The experiments found that cathodic protection improved the erosion-corrosion resistance of all alloys tested. Further tests showed there was no measurable ductility loss caused by hydrogen embrittlement as a result of applying cathodic protection.

In similar experiments, Giourntas *et al.* (2015) conducted research to determine the effect of cathodic protection on erosion-corrosion material loss for various stainless steels and one carbon steel in a marine environment. The study aimed to determine the relative roles of erosion, corrosion, and related synergy on the total erosion-corrosion material loss. The experiments used a slurry-jet impingement apparatus in 3.5 wt.% NaCl brine-sand slurry. The test samples were modified flat metal specimens that enabled electrochemical tests. The study concluded that UNS G10400 carbon steel, when placed under cathodic protection, had similar performance to many harder, corrosion-resistant stainless steels. Further analysis showed cathodic protection of stainless steels negatively affected erosion-corrosion material loss by limiting the re-passivation of the surface metal. The loss of passive films from applying cathodic protection caused increased wear from erosion dominated mechanisms on softer, bare metal.

From the above literature, it is evident that cathodic protection is useful in erosion-corrosion research. Its main uses have been to study pure erosion, to reduce erosion-corrosion, and to quantify the erosion-corrosion synergy experienced. From the experimental methods discussed, however, some limitations in the study of erosion-corrosion are evident. Many of the instruments and apparatuses used include slurry pot testers, sliding-wear apparatuses, and slurry-jet impingement apparatuses. While these apparatuses have their advantages, they may not reproduce realistic slurry environments as found in pipes. The simulated environments created in

these apparatuses may not accurately display pipe flow or the hydrodynamics of slurry flow. Moreover, the metal samples used in these apparatuses are generally flat coupons or cylindrical rods. While these types of samples are inexpensive and readily available, they may not provide results that accurately depict erosion-corrosion on a pipe wall. Flat or cylindrical samples do not display the effect pipe geometry may have on erosion-corrosion mechanisms. Additionally, while many types of materials are used during erosion-corrosion research, most of the samples discussed were stainless steels. Exploring a diverse set of materials may lead to a better understanding of erosion-corrosion.

2.7.2 Works Related to Electrochemical Apparatuses in Erosion-Corrosion Studies

As erosion-corrosion research progresses, researchers are turning to electrochemical tests to gather data on the corrosion occurring during erosion-corrosion. Electrochemical tests provide a method of studying the effect of erosion, flow velocity, and the environment on corrosion. Three-electrode electrochemical setups are instrumental in observing how corrosion and erosion interact. The following literature describes various erosion-corrosion experiments three-electrode modified apparatuses.

Wang and Stack (2000) performed electrochemical tests using a three-electrode fitting on a rotating cylinder apparatus. The experiments aimed to determine the erosion-corrosion resistance of BS 6323 mild steel, AISI 410 stainless steel, and AISI 304 stainless steel. Linear polarization scans determined the corrosion rates at various flow velocities. The slurry used had a solids concentration of 23 wt.% using alumina particles in a 0.5 M sodium carbonate solution. Pure erosion was determined from experiments performed in de-aerated solutions. Experiments showed that AISI 304 stainless steel had the most significant erosion-corrosion resistance. When flow velocity increased, all samples experienced elevated material loss. Furthermore, while the erosion-corrosion material loss was mainly erosion dominated, the more corrosion resistant AISI 304 stainless steel showed elevated erosion-corrosion resistance compared to the harder AISI 410 stainless steel. This result suggests that corrosion may play an integral part in increasing erosion wear.

Yue *et al.* (1987) performed erosion-corrosion experiments using a rotating slurry pot apparatus. The apparatus included a three-electrode system to perform electrochemical tests. The experiments studied the corrosion behaviour of industrial materials such as iron, brass, nylon, and Teflon. The slurries used included various electrolytes of high and low pH and alundum sand as the erodent. Anodic and cathodic linear polarization scans were utilized in various flow velocities and slurry concentrations to observe the synergistic relationship between erosion and corrosion. Yue found that in moderate pH environments, the mechanical properties of the material and its erosion resistance were the main factors influencing erosion-corrosion material loss. In low pH environments, the corrosion reaction and synergy between erosion and corrosion had a strong influence on the material loss. The research concluded that the acidity of the electrolyte was a significant contributor to the erosion-corrosion synergy experienced in many metals.

Jiang *et al.* (1993) studied the erosion-corrosion synergy experienced in austenitic stainless steels using a sliding wear apparatus. The apparatus was modified with the addition of a three-electrode setup to perform potentiodynamic scans on the samples while under erosion-corrosion loading to determine corrosion rates. The solution used was 20 wt.% sulphuric acid in deionized water. The total erosion-corrosion was determined using a profilometer to measure the volume of wear. The study determined that 18-8 stainless steel that is known for high erosion resistance exhibited the highest erosion-corrosion synergy. The mechanism involved in erosion accelerated corrosion was determined to be the recovery rate of the broken passive films. Metals with higher re-passivation rates exhibited lower erosion-corrosion and, in turn, lower synergy. Kim *et al.* (1981) carried out erosion-corrosion experiments on M2 tool steel and 52100 low alloy steel used in naval bearings. These experiments also used a sliding wear apparatus with the ability to perform electrochemical tests. The working electrolyte was 0.5 and 3.5 wt.% NaCl brine. The effect of erosion on the corrosion rate was determined by examining the open circuit potential shift and corrosion current densities at various erosion loading rates. Kim determined that in materials that have thick passive films, enhanced corrosion increased. Enhanced corrosion increased from erosion stripping the film which then quickly re-passivated. Increasing erosion also produced a negative open circuit potential shift on the metals. The shift in open circuit potential suggested more active corrosion occurred at higher loading rates. The corrosion current density produced during erosion-corrosion also increased two-fold between static and erosive conditions. This

observation implies that erosion increased the rate of corrosion substantially. Steels that did not produce passive films had no observable shift in corrosion potential during erosive conditions. In similar research, Kotlyar *et al*. (1988) performed erosion-corrosion experiments on high carbon, low alloy (HCLA) steel. A sliding wear apparatus was used with the addition of electrodes to perform electrochemical polarization scans. Tests used 15 vol.% quartz-water slurry with various pH conditions. The objectives of the study were to determine the pure erosion, pure corrosion, and total erosion-corrosion experienced by HCLA. Anodic and cathodic polarization scans determined corrosion rates during varying slurry concentrations. Kotlyar determined that even in conditions where corrosion is small, the erosion-corrosion synergy experienced can be significant. In general, the research concluded that the total erosion-corrosion material loss increased when subject to higher erosive loads, increasing hardness of abrasive, and with decreasing slurry pH.

Neville and Wang (2009) performed experiments aimed to determine the viability of two different corrosion inhibitors in reducing erosion-corrosion material loss. Experiments used test samples of BS080A15 carbon steel and 316L stainless steel. Erosion-corrosion conditions were produced using a recirculating slurry-jet impingement apparatus capable of performing electrochemical tests. The electrolyte consisted of highly carbonated brines typical of gas condensates. AC impedance tests were performed for in-situ corrosion measurements, while specimens were under erosion-corrosion conditions. The experiments suggested that inhibitors used on carbon steel can reduce erosion-corrosion rates significantly. The reduction of erosion-corrosion occurred from inhibitor films forming on the metal surface, reducing the energy of sand impacts along with decreasing the corrosion reaction. Li *et al.* (1995) studied the influence that an applied potential had on the erosion-corrosion behaviour of aluminum (AA1100) in silica sand slurries. Various dilute solutions of phosphate, sodium chloride, carbonate, and acetic acid were used while spanning applied potentials between -2.7 and +2.7 V_{SCE}. The experiments applied a jet-impingement slurry apparatus, including a three-electrode setup. Flat metal specimens were placed under erosion-corrosion while being held under potentiostatic control and then weighed for mass loss. Potentiodynamic scans found the effect of the applied potential on the corrosion current density. The study determined that erosion-corrosion wear was independent of the applied potential below -2.0 V_{SCE}, then followed a linear dependence as potentials increased above -2.0 V_{SCE} in the phosphate and acetic acid solutions. Using the NaCl solution,

similar erosion-corrosion behaviour was observed up until the potential reached the pitting potential. At potentials above the pitting potential, erosion-corrosion material loss increased. The carbonate solution exhibited peculiar behaviour in comparison to the film-forming solutions. The erosion-corrosion rate was shown to be independent of the applied potential below -2.3 V_{SCE}, then decreased as potentials climbed from -2.3 to -0.5 V_{SCE}, and finally increased at potentials higher than -0.5 V_{SCE}. This result showed the effect of surface films on the erosion-corrosion of aluminum.

Xie *et al.* (2003) performed electrochemical experiments on AISI 1020 carbon steel to quantify the effect of erosion on corrosion behaviour. The experiment dry-eroded flat metal samples using an air-sand jet apparatus to induce mechanical strain onto the samples at various sand loading rates and velocities. Directly after erosion, the samples were submerged in both NaCl and Na_2SO_4 solutions (2 g/L) separately. Upon submersion, linear polarization and potentiodynamic scans determined the corrosion rate, polarization resistance, and open-circuit corrosion potential. Xie determined erosion caused a negative shift in the open circuit corrosion potential. The negative shift implied an increase in corrosion activity caused by strain in the metal. As the concentration of erodent increased, the polarization resistance decreased, suggesting an acceleration of the corrosion reaction. Furthermore, the measured corrosion rate increased when using higher concentrations of sand. Excess stored strain caused by the plastic deformation of the metal may have produced the additional corrosion observed during higher slurry concentrations.

Barik *et al.* (2009) carried out erosion-corrosion research on cast NAB metal to determine the relationship between erosion and corrosion that leads to synergistic material loss. Erosion-corrosion tests used a slurry jet-impingement apparatus with modifications that accommodated electrochemical corrosion tests. The slurry used was dilute 3.5 wt.% NaCl brine with silica sand at room temperature. Potentiodynamic polarization scans studied the corrosion behaviour to quantify the synergism in erosion-corrosion. The results displayed that NAB displayed limited erosion-corrosion synergy or enhanced corrosion from increasing the erosion rate. Overall, experiments concluded an inconclusive relationship between erosion and corrosion as NAB displayed neutral synergistic behaviour in the tested conditions.

The above literature displays that three-electrode modified apparatuses are useful in determining erosion-corrosion mechanisms. Electrochemical testing methods give researchers the ability to

study the effect of erosion and environmental parameters on corrosion and erosion-corrosion synergy. However, similar to Section 2.7.1, many of the apparatuses used may not simulate erosion-corrosion conditions accurately. The advantage of the apparatuses chosen in the above literature is the ease in which electrochemical tests can be performed. This suggests research may benefit from incorporating electrochemical cells into apparatuses that more realistically model slurry flow, such as flow loops. Many of the experiments discussed also focussed on dilute brine environments. Research related to saturated brine environments (such as those in many mining industries) may be under-represented. Future erosion-corrosion experiments should use saturated brines to broaden the representation of brine concentration in research. The literature also showed a strong emphasis on material classification – providing data to show which materials are best suited to resist erosion-corrosion. While classification is essential for material selection, research may benefit from experiments performed to understand the fundamental mechanisms into why certain materials perform better than others.

2.7.3 Works Related to the Effect of a Solid Phase on Corrosion in Erosion-Corrosion Systems

Understanding the mechanisms in which corrosion accelerates erosion and vice versa is essential to determine a material's ability to withstand erosion-corrosion. The following literature describes experiments and findings of researchers who have isolated and studied the effect of solids (erosion) on corrosion behaviour. The research includes the effect of solids concentration, and particle size/shape/hardness on the corrosion experienced on various materials.

In a study performed by Rajahram *et al.* (2011), the synergistic effect of solids on the corrosion rate of UNS S31603 stainless steel was explored. Experiments used a slurry pot apparatus capable of in-situ electrochemical corrosion tests. The test samples were cylindrical rods. Experimental tests used a combination of mass loss and linear polarization scans to determine erosion and corrosion mass loss. All experiments utilized a 3.5 wt.% NaCl brine solution with silica sand as the erodent. Flow velocities ranging from 5-9 m/s, sand concentrations ranging from 1-5 wt.%, and various sand sizes were included as experimental variables. The research concluded that faster flow velocities increased corrosion by raising the mass transfer of oxygen

and the kinetic energy of the sand particles. Additionally, as sand concentration increased, the corrosion increased in response. The increased corrosion from larger slurry concentrations occurred due to an increase in the number of impingements that remove corrosion products and passive films. The removal of corrosion products and films is known to increase the rate of dissolution. When particle size was varied, the medium-sized particles (150-300 μm) exhibited the most significant corrosion. The coarse particles (300-600 μm) showed the next highest degree of corrosion, followed by the fine particles (90-150 μm). Particle size experimental results suggested there was a complex effect of size on the corrosion rate. The complexity may be a balance between the number of impacts (which increases with smaller size), and the momentum or energy of each impact (which decreases with smaller size).

In research performed by Guo *et al.* (2005), erosion-corrosion was studied on AISI 1045 carbon steel to investigate the interaction between erosion and corrosion that leads to synergy. Experiments aimed at quantifying enhanced erosion and enhanced corrosion. The effect of anodic current density on metal hardness was also explored. The apparatus used was a modified rotating cylinder electrode. The slurry solution was comprised of 0.1 M Na_2SO_4 in deionized water and silica sand. Pure erosion material loss was measured by placing samples under cathodic protection to inhibit corrosion. Pure corrosion material loss was measured from experiments performed in the absence of an erodent. Potentiodynamic scans, open circuit potentials, linear polarization, and potentiostatic control methods gathered corrosion data while the material was under impingement. Tests used 35 wt.% slurry concentration. Results showed that the impingement of sand did not alter the corrosion rate significantly. It was suggested that the test conditions (flow velocity and sand concentration) might have exceeded the oxygen mass transfer limitation of the corrosion reaction, causing the insignificant erosion-corrosion synergy observed. The study recommended further research into the electrochemical behaviour of carbon steel under erosion-corrosion.

Postlethwaite *et al.* (1974) researched the corrosion rate of ASTM A53 carbon steel pipe samples during flow-assisted corrosion and erosion-corrosion conditions. The aim was to determine the effect flow velocity, and suspended solids had on the in-situ corrosion rate. The apparatus used was a flow loop, including a modified carbon steel pipe sample with a reference electrode built into its center. The counter electrode was placed downstream of the carbon steel pipe. Well water

was used as the test solution to ensure each experiment had the same composition throughout testing months. The solids used varied in size and included silica sand, iron ore, potash, limestone, and coal. Solids concentrations were chosen based on industry practices for each material (generally between 30 – 70 wt.%). An electrochemical approach measured the corrosion rates during experiments. E_{corr} was measured during erosion-corrosion at a set flow velocity and solids concentration. Next, the flow loop was deoxygenated and held at E_{corr} using potentiostatic control. With the sample held at $E_{corr,}$ i_{corr} was measured and converted to a corrosion rate using Faraday's law. The study concluded that for most solid particles tested, the corrosion rate grew from increasing flow velocity and solids concentration. The exception was potash solids/brine in which the corrosion rates stayed consistent regardless of changing flow velocity or solids concentration. The corrosion behaviour in the potash solution was determined to be caused by scale formation on the material's surface. Scale formation with potash solutions may occur at flow velocities slower than 7 ft/s (Postlethwaite *et al.,* 1974). The research recommended that further experiments using potash brines at higher flow velocities be performed.

A study performed by Zeng *et al.* (2016) aimed to measure the corrosion and passivating behaviour of 304 stainless steel elbows during erosion-corrosion. This research was conducted with a flow loop apparatus and a multi-electrode elbow design to allow electrochemical and mass loss measurements at 16 different points within a 90° elbow. Erosion-corrosion tests used a 3.5 wt.% NaCl brine at various flow velocities and a silica-sand concentration of 0.9 wt.%. Mass loss measurements within the elbow were taken to define the total erosion-corrosion. Potentiodynamic scans, EIS, and open circuit potential measurements were performed throughout erosion-corrosion tests to observe corrosion behaviour. Experiments determined that the most considerable erosion-corrosion wear occurred on the outlet of the outer wall. The least wear occurred on the inner side of the inlet. The E_{corr} at the outer outlet wall climbed during the experiment for 2000 seconds and then proceeded to drop. The climbing E_{corr} during the experiment corresponds to the corrosion rate increasing from the rapid depassivation and repassivation caused by particle impingements. Generally, the experiments showed that flow velocity and sand concentration led to increased corrosion rates. The larger corrosion rates may have been caused by faster mass transport of oxygen to the surface of the metal during higher slurry concentrations and flow velocities. Further analysis showed that the various locations

tested in the elbow corroded at different rates. Varying corrosion rates may create local anodes and cathodes, causing galvanic corrosion when these locations are coupled.

Malka *et al.* (2006) conducted experiments to investigate the interaction between erosion and corrosion to quantify erosion-corrosion synergy into its components. The study focussed on sudden pipe expansions and contractions. The experiments utilized a flow loop apparatus testing plain AISI 1018 carbon steel in 1 wt.% NaCl solution mixed with silica sand at 2 wt.%. The solutions acidity was increased by purging the system using a stream of CO_2. The erosion-corrosion test section consisted of a 4-inch diameter pipe contracting into a 2.47-inch, then expanding back to 4-inch. The test sections of pipe contained many slices of metal pipe separated by an insulating material. Each slice had electrodes within to make electrochemical measurements during erosion-corrosion. Measurements included the in-situ corrosion rate via linear polarization scans. Pure erosion was measured by inhibiting corrosion through the displacement of oxygen and measuring the mass loss of the slices during erosion-corrosion conditions. The research observed that pipe expansions and contractions had little effect on the measured corrosion rate. However, a slight increase in corrosion occurred in the 2.47-inch pipe from increased turbulence, the results of a higher Reynolds number. Further analysis found that corrosion increased significantly along the test sections due to erosion. Corrosion caused by the addition of sand was approximately twice that of the pure corrosion rate in the absence of solids. The increased corrosion may have been caused by turbulence and mass transfer rates increasing from the addition of sand. Additionally, corrosion rates may have increased due to impingements roughening the metal surface, adding more corrodible surface area.

Additional experiments on pipe segments were performed by Lotz and Postlethwaite (1990) to determine the enhanced corrosion and erosion-corrosion occurring in sudden expansions and contractions. The aim was to provide insights into erosion-corrosion and synergistic mechanisms. The apparatus used was a flow loop capable of pumping slurries with concentrations of up to 20 vol.% solids. The pipe segments tested had electrochemical cells built within them to enable corrosion measurements during erosion-corrosion loading. Experiments used AISI MT-1015 carbon steel and 304 stainless steel as the pipe materials. The slurry was composed of 3.5 wt.% NaCl brine mixed with 2 vol.% silica sand. Polarization resistance measurements were performed to determine in-situ corrosion rates. The study found that erosion,

corrosion, and erosion-corrosion all increased in the smaller diameter pipe due to an increase in the Reynolds number. It was also determined that corrosion increased with the addition of sand in low concentrations. The increase in corrosion rate was attributed to the removal of corrosion product films, which increased the dissolution of metal. The larger corrosion rates observed under slurry loading may also have been caused by solids increasing the mass transfer of oxygen.

Yang and Cheng (2012) conducted experiments to show how parametric effects such as sand concentration, slurry flow velocity, and impact angle affect erosion-corrosion in oil slurries. The experiments were performed using a slurry jet-impingement apparatus. The slurry jet was modified to use a three-electrode setup for corrosion testing. Measurements performed include polarization scans for corrosion, mass loss measurements for erosion and erosion-corrosion, and surface inspection. Test samples were coupons of X65 carbon steel. The test solution used emulated oil sands slurry using sand as the abrasive. Erosion-corrosion tests were performed at flow velocities ranging from 0-5 m/s, various lengths of time, and slurry concentrations of 0, 5, 10, and 20 wt.%. The research showed that both anodic and cathodic current densities increased with sand concentration. The increase in current densities indicated the synergistic enhancement of corrosion caused by a second phase. The effect of impact angle on the corrosion rate was also shown to be negligible. Further study discovered that when the corrosion potential was relatively negative (cathodic), the process was erosion dominated. When the corrosion potential was relatively positive (anodic), the process was corrosion dominated. The research concluded that enhanced corrosion was likely caused by erosion increasing oxygen diffusion rates or from the removal of protective films.

From the discussed literature, many of the studies performed erosion-corrosion experiments at low solids concentrations between 0 and 5 wt.%. Experiments performed at higher solids concentrations did occur, but usually did so in broad step changes of 5 to 10 wt.%. While valuable insights on the interaction of erosion and corrosion were shown in the above literature, it could be concluded that experiments are required using higher slurry concentrations in smaller step sizes. Research performed using smaller slurry concentration step sizes may provide a more precise indication of how erosion interacts with corrosion on the metal surface. Also, many of the experiments discussed once again use test solutions made of dilute brines. Dilute brines are commonly used as the chemistry associated with low concentration electrolytes is well known.

Erosion-corrosion systems composed of saturated electrolytes should be studied in more depth to account for industries and processes with these environments. Compared to previous experiments discussed in Sections 2.7.1 and 2.7.2, the above literature did succeed well in using pipe or elbow samples. These samples accurately reflect erosion-corrosion in pipe flow and consider how the geometry of the pipe may affect erosion-corrosion.

2.8 Knowledge Gap

As erosion-corrosion is a relevant issue in industry, there is extensive research performed on erosion-corrosion and the corresponding erosion-corrosion synergy. In erosion-corrosion research, many experimental results focus on material classification. When studying material classification, experimental results determine which materials are best suited to withstand erosion-corrosion environments. While material classification is vital for material selection, it speaks little to the interaction between erosion and corrosion. In the abundance of study on erosion-corrosion, the mechanisms that describe their interaction and synergy are not well known. This suggests that experiments to observe and quantify the synergy between erosion and corrosion should be further explored. Understanding how erosion and corrosion interact could lead to a more detailed understanding of why certain materials are more resistant to erosion-corrosion.

In the provided literature, many erosion-corrosion experiments focussed on stainless steel specimens. Stainless steels are commonly used in industry for their corrosion resistance. However, stainless steel is likely not the most abundant metal used in industry. A more common material used, due to its mechanical properties, abundance, and cost, is plain carbon steel. Increased observation and experimentation of the erosion-corrosion interaction on carbon steel should be explored. A better understanding of erosion-corrosion on carbon steel may provide insights into operating parameters that limit material loss or the fundamental mechanisms driving erosion-corrosion synergy.

It was observed that the apparatuses used in many erosion-corrosion experiments may not mimic turbulent pipe flow as experienced in many erosion-corrosion systems. These include slurry-test pots, slurry-jet impingement apparatus, and sliding-wear apparatus, all of which use simulated

erosion-corrosion environments. These apparatuses may not accurately simulate slurry flow or the distribution/hydrodynamics of solids inside of pipelines. These apparatuses also generally use flat coupons or cylindrical samples. Coupons or cylindrical samples may neglect the effect pipe geometry has on the erosion-corrosion process. To achieve realistic results, a flow loop apparatus that simulates slurry flow with actual pipe samples is better suited for erosion-corrosion studies. Observation of pipe elbows, which are among the most targeted regions in erosion-corrosion, would provide additional relevance and importance.

Much of the previous literature discussed used dilute brines or acids/bases as their electrolytes. Dilute brines are beneficial electrolytes for research as the chemistry is less complicated and many industrial process streams have low concentrations of salt. However, in the mineral processing industry many process streams may have much larger concentrations of salts, including saturated brines. This suggests that erosion-corrosion experiments using saturated brines may provide valuable insights. Also, many previous experiments studied low slurry concentrations or increased slurry concentration in large steps. Using large slurry concentration step sizes may limit understanding the erosion-corrosion behaviour between steps or possible transition regions. In addition, using low slurry concentrations in experiments only provides erosion-corrosion data over a small frame of reference. Research using smaller slurry concentration step sizes and higher slurry concentrations overall may provide unforeseen trends in erosion-corrosion behaviour.

While cathodic protection in erosion-corrosion research is widely explored, it is rare to protect the inside of pipes. Internal cathodic protection applied to pipes on a flow loop apparatus may provide interesting insights. Applying cathodic protection to the inside of a pipe may provide a unique opportunity to explore the use of cathodic protection for erosion-corrosion purposes (both applied and experimental). Exploring internal cathodic protection may also lead to observing corrosion behaviour during erosion-corrosion.

From the literature review, it is hypothesized that a methodology to determine the in-situ corrosion rate can be developed from measuring the protection current density of an internally protected pipe segment in slurry and non-slurry flow.

2.9 Objectives

There are five primary objectives in the proposed erosion-corrosion research:

1. Design and develop a cathodic protection system to protect an AISI 1018 carbon steel elbow within a flow loop containing a saturated potash-sand slurry environment;
2. Explore the application of cathodic protection on the inside of a pipe during slurry flow to observe erosion-corrosion, erosion-corrosion synergy, and corrosion behaviour;
3. Determine correlations between flow velocity, slurry concentration, and particle size to the corrosion and enhanced corrosion experienced on the inside of a carbon steel elbow;
4. Explore possible mechanisms that describe the relationships observed between flow velocity, slurry concentration, and particle size to the corrosion rate and enhanced corrosion experienced;
5. Develop a correlation between protection current density and the corresponding corrosion rate being inhibited.

3. Methodology

3.1 Introduction

Laboratory experiments were conducted investigating erosion-corrosion in a saturated potash brine according to the objectives described in Section 2.9. These included experiments performed in a stationary electrolyte using galvanic protection and within a flow loop with impressed cathodic protection. Both types of experiments were performed systematically to compliment one another in the research. This section will present the materials, apparatus, and the experiments and procedures utilized in this research.

3.2 Materials

3.2.1 Test Specimen - Carbon Steel Elbow

The test specimens used in the erosion-corrosion experiments were AISI 1018 carbon steel elbows, as shown in Figure 3.1. The elbows had a radius of curvature (R) of 38.1 mm and inner diameter (r) of 27.0 mm. The radius of curvature was chosen to reflect the tight curves observed in many process piping settings. The elemental composition of the elbows is displayed in Table 3.1. During this research, elbows were ordered in large batches from the same manufacturer (Apex Distribution Inc.) to ensure all experiments used samples with similar composition, dimensions, and mechanical properties (see Appendix E for the manufacturer's material datasheet). Before inserting an elbow into the flow loop, they were sandblasted to clean the surface and remove coatings or films.

Table 3.1. Elemental composition of AISI 1018 carbon steel elbows.

Elbow Material	**Chemical Composition % Maximum**										
	C	**Mn**	**P**	**S**	**Si**	**Cr**	**Mo**	**V**	**Ni**	**Cu**	**Ce(2)**
	x 10^{-2}	**x 10^{-2}**	**x 10^{-3}**	**x 10^{-3}**	**x 10^{-2}**	**x 10^{-2}**	**x 10^{-2}**	**x 10^{-2}**	**x 10^{-2}**	**x 10^{-2}**	**x 10^{-2}**
AISI 1018 Carbon Steel	20	49	22	10	25	3	0.2	0.4	2	3	29

Figure 3.1. AISI 1018 carbon steel elbow from Apex Distribution Inc. (Model #: A234-WPB-WE1SL9B) used for erosion-corrosion testing on the flow loop.

3.2.2 Electrolyte

The test solution used for each experiment was saturated potash brine. Processed, untreated potash ore was procured from a Nutrien pilot plant facility located at the University of Saskatchewan campus. The potash came in five-gallon containers in a ground, sand-like consistency. Potash is primarily composed of KCl. However, various other compounds and salts may also be present. Table 3.2 shows the composition of the potash used in this research's experiments. Material safety data sheets (MSDS) for the potash ore are found in Appendix E.

Each experiment performed on the flow loop used 18 L of saturated potash brine. A saturation table of KCl in water was utilized to determine the correct potash-water ratio required to make 18 L of brine. The saturation value for each batch of brine was 34.4 g KCl per 100 g H_2O. The density of saturated potash brine is 1.182 kg/L. Using the density of saturated potash brine and the potash-water ratio, the required mass of water and potash to combine was determined. Each 18 L mixture of brine contained approximately 15.820 kg of water and 4.646 kg of potash.

Table 3.2. Composition of potash as provided by Nutrien.

Compound Name	**Abbrev.**	**Composition wt.%**
Potassium Chloride	KCl	95.0 - 99.8
Sodium Chloride	NaCl	1.0 – 4.0

3.2.3 Sand Abrasive

Simulated potash slurry was created by adding silica sand as the second phase abrasive. Slurry experiments tested two sizes of sand particles. The sand particles had an average nominal diameter of 1.05 mm and 0.55 mm, respectively. These particle sizes were chosen to reflect the crystals found in overstaured brines, as well as to ensure an observable variance between the data attained. Both grains of sand were angular/sub-rounded and filter grade to ensure a narrow particle diameter distribution. The 1.05 mm sand was Grade 10-20 manufactured by Target Products Ltd and had a size distribution shown in Table 3.3. The 0.55 mm sand was Grade 4095 manufactured by Granusil Mineral Fillers and had a size distribution shown in Table 3.4. Please refer to Appendix E for Material data sheets of each sand size.

Table 3.3. Target Products Ltd Grade 10 - 20, 1.05 mm diameter, particle size distribution measured as the % passing through each sieve.

Sieve Size		**Sand Type, Cumulative Passing Through (%)**
ASTM	**Metric**	**Grade 10 - 20**
No. 8	2.36 mm	100
No. 10	2.00 mm	99 - 100
No. 12	1.70 mm	90 - 100
No. 16	1.18 mm	10 - 35
No 20	0.850 mm	0 - 3
No 30	0.600 mm	0 - 1
No 40	0.420 mm	0
No 50	0.300 mm	0
No. 70	0.212 mm	0
No. 80	0.180 mm	0
Effective Size, d_{10} (mm)		0.85 - 1.25

Table 3.4. Granusil Mineral Fillers Grade 4095, 0.55 mm diameter, particle size distribution measured as % retained on each sieve.

Sieve Size		**Sand Grade, Typical Mean % Retained on Individual Sieves**
ASTM	**Metric**	**Grade 4095**
No. 12	1.70 mm	0
No. 16	1.18 mm	0
No 20	0.850 mm	1.3
No 30	0.600 mm	34.9
No 40	0.420 mm	58.7
No 50	0.300 mm	4.2
No. 70	0.212 mm	0.7
No. 100	0.150 mm	0.2
No. 140	0.106 mm	0
No. 200	0.075 mm	0
No. 270	0.053 mm	0
No. 325	0.045 mm	0
Effective Size, d_{10} (mm)		0.55

3.3 Apparatus

3.3.1 Flow Loop

For non-stagnant flow, a vertically oriented flow loop was designed and built at the University of Saskatchewan. Flow loop apparatuses are proficient at recreating erosive-corrosive conditions and providing a platform for erosion-corrosion research. A labelled diagram of the flow loop is shown in Figure 3.2. This figure presents the overall configuration and various elbow locations. The loop contains a peristaltic pump capable of pumping slurries to velocities between 0 and 4.5 m/s. The system also contains a dampener to reduce pressure oscillations caused by the positive displacement peristaltic pump. Some experiments in erosion-corrosion benefit from or require the inhibition of corrosion. Corrosion can be inhibited on the flow loop using a nitrogen tank, which purges the fluid/slurry of oxygen. During experimentation, each piping loop contains four elbow locations where test specimens can be placed. Straight pipe specimens can also be installed within the flow loop for erosion-corrosion testing. Piping and flow loop specifications are given in Table 3.5.

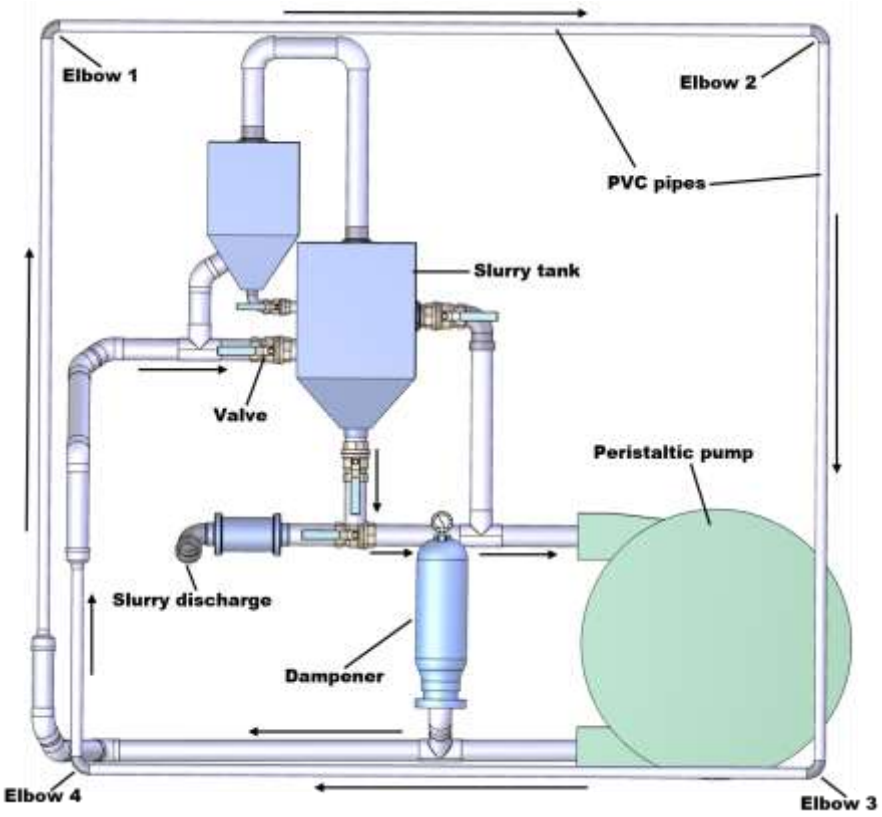

Figure 3.2. Schematic of the University of Saskatchewan flow loop – reproduced from Elemuren *et al.* (2018) with permission from Elsevier.

Table 3.5. University of Saskatchewan's flow loop specifications.

Flow Loop Variable	**Specification**	**Unit**
Pump Speed	0 - 80	Hz
Flow Velocity	0 - 4.5	m/s
Slurry Concentration	0 - 70	wt.%
Pipe Inner Diameter	25.4	mm
Pipe Schedule	40	-
Pipe Material	PVC	-
Pipe Section Length (between elbows)	2.44	m

Most flow loop components are made of PVC to allow simple retrofitting of the pipe design to fit a variety of experiments. PVC is also easily replaceable and has excellent resistance to degradation and corrosion in slurry environments (Yabuki *et al*., 2000). The length-to-diameter ratio used in each section of the pipe ensures that flow is fully developed before the position of elbow samples. Generally, turbulent, fully developed flow can occur at lengths between 10 to 40

times the diameter of the pipe (Cimbala and Cengal, 2006). All pipe sections used in the flow loop were greater than 40 times the diameter.

From the previous schematic in Figure 3.2, there are four possible elbow locations for experimentation. In this research, the use of cathodic protection to inhibit corrosion limited experiments to one elbow location due to design constraints. To ensure this research yielded the best possible results, data collected by a previous researcher's calibration on the same flow loop was analyzed. Table 3.6 shows the calibration test data from previous researcher Raheem Elemuren (2020). The calibration data helped to select the appropriate elbow location for the study. In the table, each elbow location's erosion-corrosion range, along with the uncertainty depicting the repeatability and accuracy of each elbow location, is shown. Elbow 3 was selected for study in this research as it experienced the highest degree of erosion-corrosion.

Table 3.6. The corresponding erosion-corrosion uncertainties and erosion-corrosion range at elbow locations 1-4 found at 3.0 m/s and 20 wt.% sand concentration in potash brine (Elemuren, 2020)

Elbow Location	**Erosion-corrosion Range (g/m^2hr)**	**Uncertainty (%)**
1	16.38 - 17.00	4.6
2	10.85 - 11.47	6.9
3	17.44 - 18.68	8.6
4	12.0 - 12.64	6.6

The corrosion rate of materials is generally affected by temperature. As such, the temperature of the electrolyte or slurry was kept constant during experiments to mitigate experimental error. The temperature of electrolyte or slurry used, unless otherwise specified, was 30 °C. This temperature was maintained using a VWR Heat Circulator (1400W/2200W) heat exchanger attached to the flow loop.

3.3.2 Test Elbow Holder

Silicone sleeves were used to secure the elbows onto the flow loop. The silicone sleeve acts as a flexible, durable intermediate between the metal elbow and the PVC flow loop piping. The

silicone sleeve worked by inserting the elbow into the bend, followed by attaching the sleeve to the PVC piping at Elbow 3. Due to the severe erosion experienced at the exit of the elbow, a 102.5 mm (4-inch) carbon steel pipe section was placed on the discharge end. The discharge pipe was generally replaced after 200 hours of use and had the same elemental composition as the test elbows.

Two wide, ring style pipe clamps secured and aligned the straight pipe section with the exit of the elbow. The same clamps secured and aligned the entrance PVC pipe to the entrance of the elbow. The alignment of the PVC and steel discharge pipe with the elbow was vital in the experimental preparation to achieve accurate and repeatable results. Figure 3.3 shows the complete setup of a test elbow in the silicone sleeve.

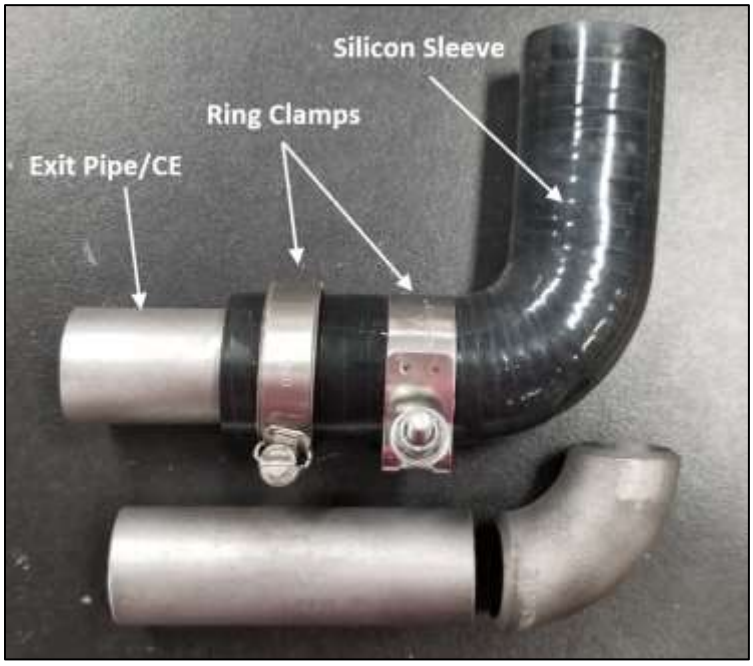

Figure 3.3. Alignment and setup of an AISI 1018 carbon steel elbow and exit pipe within a silicon sleeve.

3.3.3 Potentiostat and Reference Electrode

Many of the experiments in this research required the use of a potentiostat to perform electrochemical tests. A potentiostat is a device used to run a variety of electrochecical tests on

conductive materials using various configurations of electrodes. The tests performed in this research using the potentiostat are described in Section 3.4.2. The potentiostat used in this research was a Parstat 3000, as made by Princeton Applied Research (Model #: 15021486) shown in Figure 3.4. The Parstat 3000 can perform a variety of electrochemical experiments using the six electrical leads. The potentiostats maximum potential range and current capacity were 30 volts and 1 amp, respectively.

Figure 3.4. Princeton Applied Research Parstat 3000 Potentiostat (Model #:15021486).

Potentiostats commonly work in conjunction with reference electrodes to perform potential measurements in electrolytes. In this research, all electrochemical tests used a saturated calomel electrode (SCE) made by Accumet (Model #: 13 620-52). Figure 3.5 shows the SCE used in conjunction with the Parstat 3000. Throughout experimentation, the SCE was regularly

calibrated to a new SCE made by the same manufacturer. The KCl solution in the SCE was replaced if the calibration showed a potential difference greater than five millivolts.

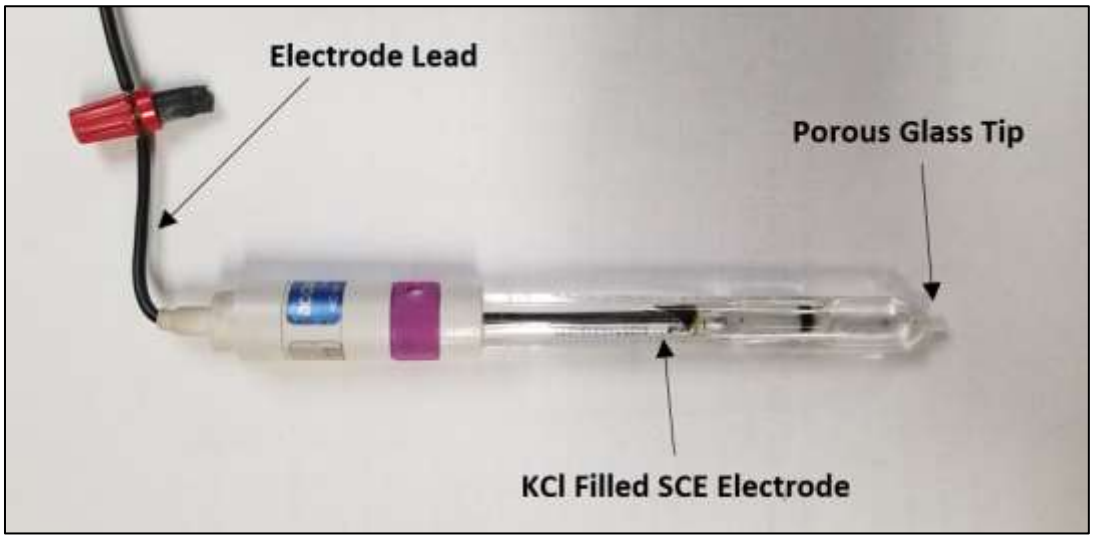

Figure 3.5. Saturated calomel electrode (SCE) made by Accumet (Model #:13 620-52).

3.3.4 Phase I Experimental Apparatus

Phase I experiments required an apparatus that would cathodically protect the inside surface of a steel pipe in saturated potash brine. The experiments aimed to determine the E_{prot} and i_{prot} of the steel. Figure 3.6 shows the apparatus used for Phase I experiments. The apparatus consisted of a 102.5 mm (4-inch) steel pipe and a 152.4 mm (6-inch) magnesium rod submerged vertically in a bucket of saturated potash brine. Th6e pipe was coated in a thick enamel to inhibit corrosion on the external surfaces. Coating the outside of the pipe ensured only the inside pipe walls interacted with the brine. Cathodic protection was applied by connecting the pipe and magnesium rod by a wire. Each wire connection (on the pipe and magnesium) was soldered in place and covered in epoxy. Many of the apparatus pieces were designed using Solidworks and 3-D printed. All 3-D printed apparatus pieces (see red objects in Figure 3.6) were made using a MakerBot Replicator 2.

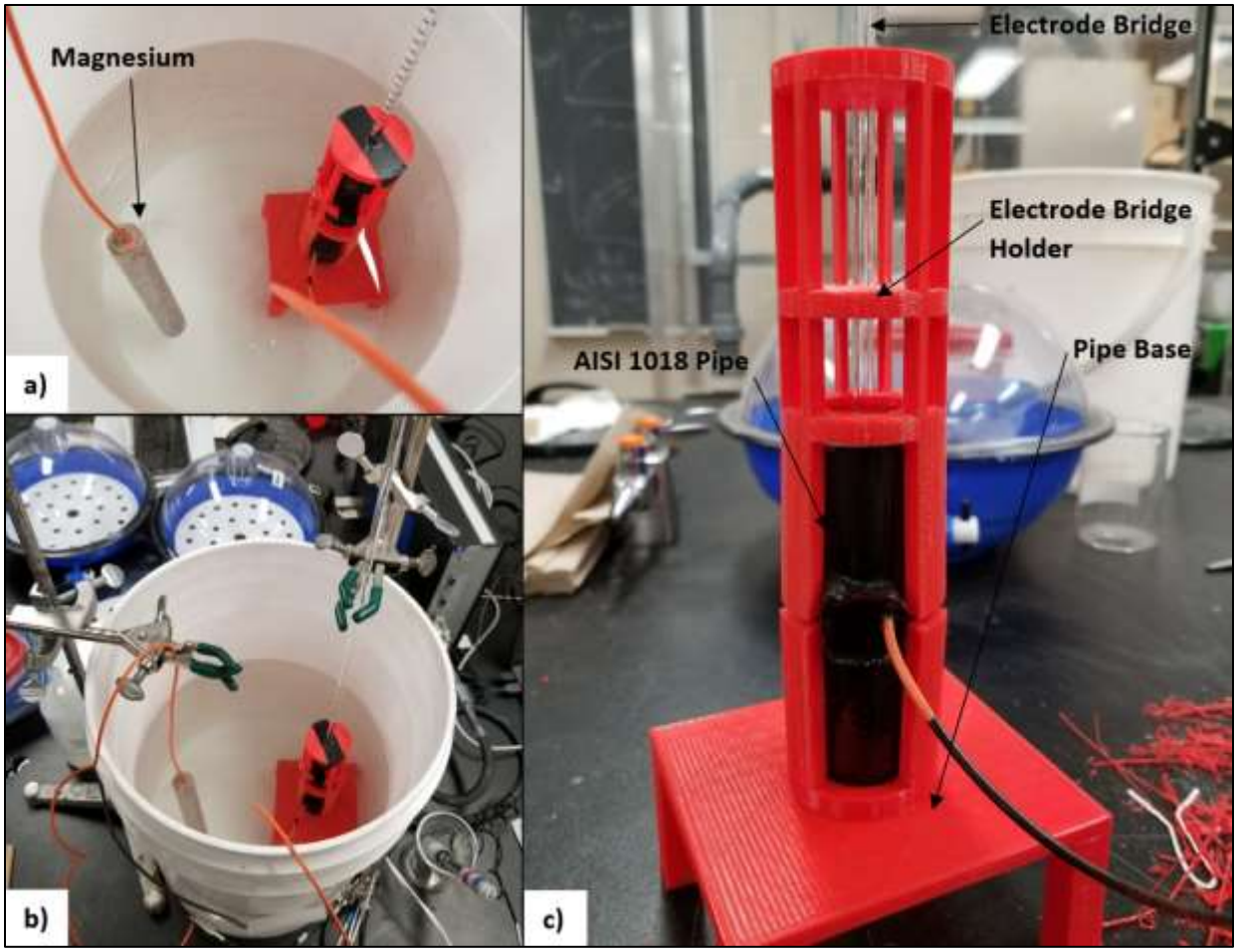

Figure 3.6. Experimental setup for Phase I to determine E_{prot} and i_{prot}: (a) Setup before coupling magnesium and steel pipe; (b) Steel pipe and magnesium rod coupled electrically and placed in saturated brine with reference electrode through center; (c) 3-D printed apparatus used to hold carbon steel pipe submerged vertically in brine.

3.3.5 Impressed Cathodic Protection System

The impressed cathodic protection system (ICPS) was designed and built for this research. The function of the ICPS was to apply impressed cathodic protection to the inside surface of an elbow during slurry flow operation. The apparatus was made to be compatible with the vertical flow loop. The ICPS was utilized in Phase II, Phase III, and Phase IV experiments.

As stated in the literature review, applying cathodic protection to the inside of pipes is rarely performed due to poor economics and large throwing power requirements. Furthermore, the

application of cathodic protection in slurry environments is rare and generally not performed on flow loops. Impressed cathodic protection systems require the following three electrodes:

1) Working electrode (WE): the material being observed or protected.
2) Counter electrode (CE): a material acting as a surface for anodic reactions, and which completes the electrical circuit between the electrolyte and the WE.
3) Reference electrode (RE): a known half-cell electrode used to measure the potential between the working electrode and the surrounding aqueous environment.

An issue of applying impressed cathodic protection on the inside of pipelines is the placement of the RE and CE. The CE must be placed in the electrolyte near the WE, but not in direct contact. The RE must also be placed in the electrolyte, being as close to the WE as possible. Within a small diameter pipe, space for the CE and RE may be limited. The placement of the CE and RE inside the pipe may also affect the flow regime and change either process or experimental operating parameters.

Monitoring and applying cathodic protection using a slurry electrolyte adds difficulty. This research used an aqueous medium containing a mixture of saturated potash brine and high concentrations of silica sand. Placing a RE inside a pipe with an abrasive slurry would likely degrade the delicate glass tube and porous tip. The effect of slurry flow velocity and direction on cathodic protection systems was also a consideration. Flow velocity and direction can affect the transmission of electric fields and current from upwinding (Heppner and Evitts, 2005). Upwinding was a consideration for the placement of the CE, to determine if the impressed electrical current would flow co-current or counter-current to the slurry direction.

The ICPS fabricated and used is shown in Figure 3.7. Many design choices addressed the constraints discussed in previous paragraphs. The RE was placed in electrical contact with the slurry, but not in physical contact. The electrical contact of the RE to the slurry electrolyte was achieved by placing a T-joint directly after the CE and attaching an electrode bridge with a porous wooden plug to the top. The electrode bridge contained saturated KCl brine and housed the RE. The porous wooden plug at the electrode bridge base was a barrier to the slurry inside the pipe while allowing an electrical connection to the RE. The T-joint setup ensured the slurry could not damage the RE.

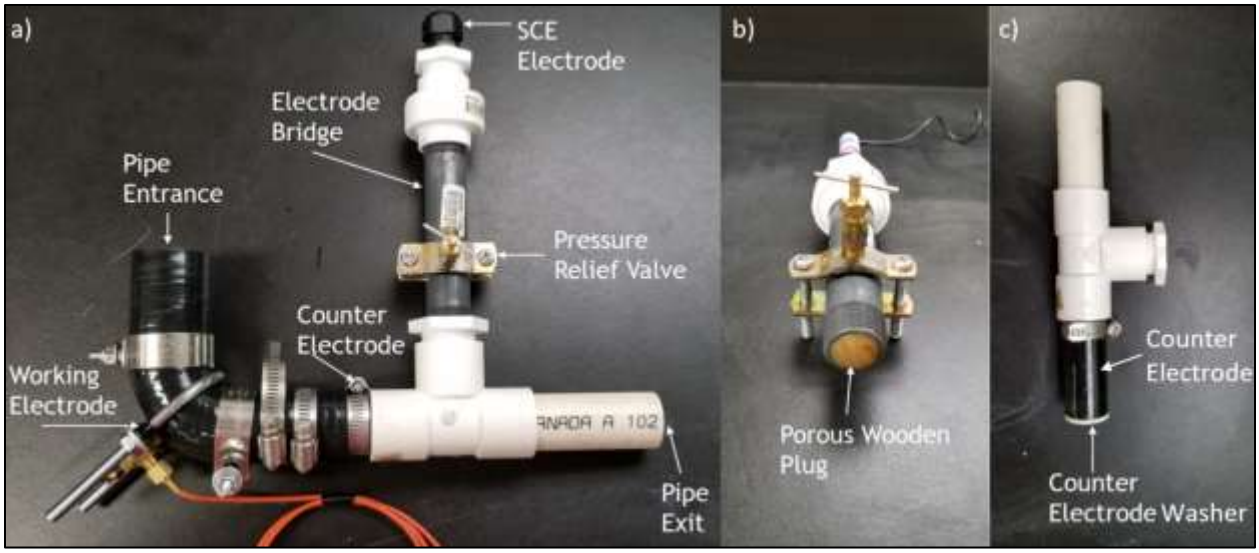

Figure 3.7. (a) The Internal Cathodic Protection System (ICPS) schematic as shown in totality; (b) Diagram of the electrode bridge and porous wooden plug filled with saturated KCl brine; (c) Diagram of the counter electrode, washer, and pipe segments that connect to the ICPS.

The CE selected was a straight, 102.5 mm (4-inch), AISI 1018 carbon steel pipe placed directly on the exit of the WE (see Figure 3.7c). The CE worked conveniently, as when using concentrated slurries, the flow loop required a steel exit pipe regardless of applying cathodic protection. The electrical isolation of the CE from the WE was achieved using a 2 mm PVC washer. Separation of the CE from the WE ensures the protective current is flowing through the electrolyte and not short-circuiting. The surface area of the CE was also considered. The counter electrode was given roughly twice the surface area of the WE to support the cathodic protection current load.

A silicone sleeve contained the WE (elbow), which could be attached and detached from the flow loop. Impressed cathodic protection requires an electrical connection to the elbow within the sleeve and the potentiostat. The electrical connection was achieved using a brass needle compressed against the curved surface of the sleeve. The brass needle could be slowly screwed to extend through the sleeve and against the elbow. Attached to the needle was a 20 gauge insulated wire lead that connected to the potentiostat. All electrodes on the ICPS are connected to the potentiostat using leads. Figure 3.8 shows the ICPS installed on the flow loop.

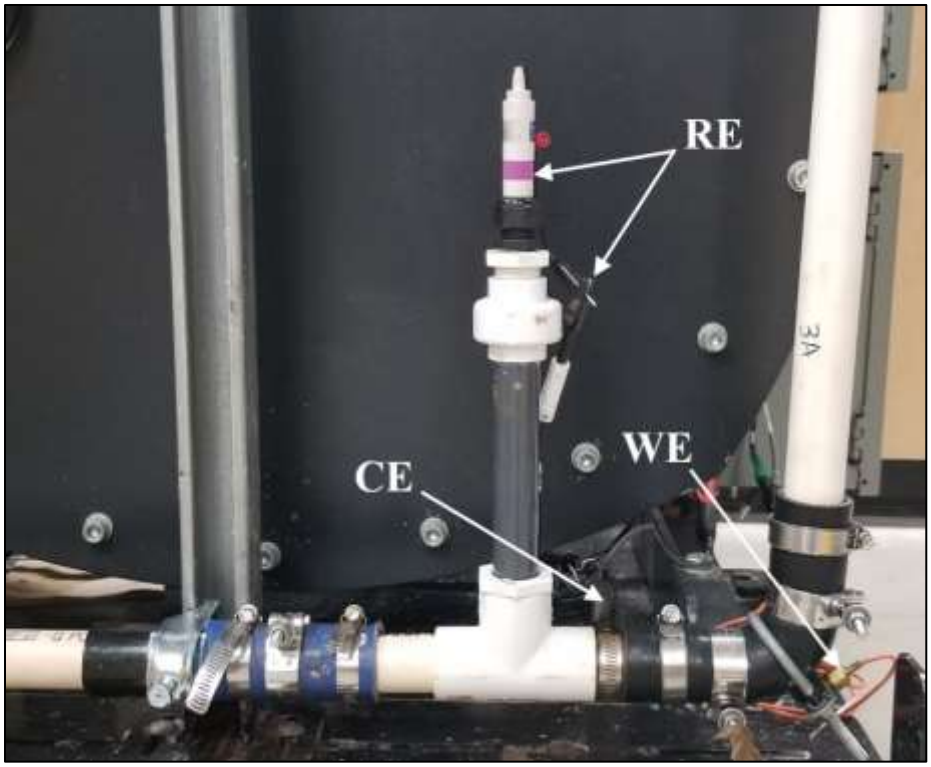

Figure 3.8. ICPS installed on the flow loop with leads on the RE, WE, and CE connected to the potentiostat.

3.4 Experiments and Procedures

The experiments and procedures of this research were split into four distinct phases. Figure 3.9 shows a detailed flow diagram of the experimental phases.

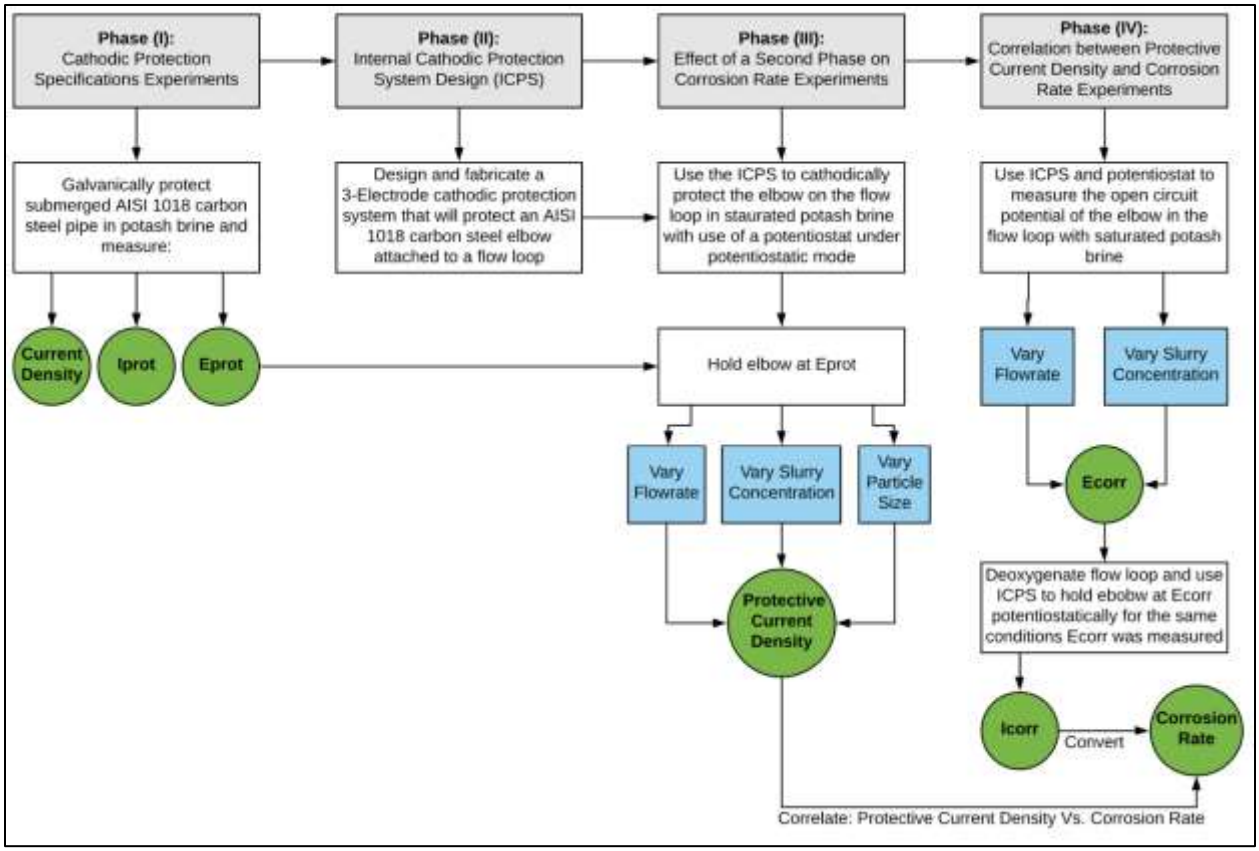

Figure 3.9. Flow diagram showing the four procedural phases of research.

Phase I involved determining cathodic protection parameters for carbon steel pipes fully submerged in saturated potash brine. The parameters measured were the protective potential (E_{prot}) and the protective current density (i_{prot}).

Phase II involved the design and fabrication of the ICPS apparatus to protect the inside of a carbon steel elbow attached to the flow loop during solid-liquid slurry flow. Phase II was completed by testing the ICPS on the flow loop.

Phase III experiments determined the effect a second phase had on the in-situ corrosion inside carbon steel elbows. Phase III experiments cathodically protect the elbows and vary flow velocity, slurry concentration, and sand-size while measuring i_{prot}. The changes observed in the value of i_{prot} were used to infer the corrosion activity occurring inside the elbow.

Phase IV focussed on determining the correlation between i_{prot} and the corrosion rate occurring inside the carbon steel elbow. However, the correlation is likely specific to the corrosion

environment tested (material, environment, and flow parameters). Therefore, the correlation determined would be specific to this research. Phase IV utilized an experimental method developed by corrosion researcher Postlethwaite (1974). Postlethwaite's research determined the corrosion rate occurring at various flow velocities and slurry concentrations within a pipe on a flow loop. Postlewaite's method, in conjunction with Phase III data, was used to correlate i_{prot} and corrosion rate of the elbow.

3.4.1 Phase I Experiments – Determining i_{prot} and E_{prot}

In this research, cathodic protection was used to study the interaction of erosion and corrosion on elbows in saturated potash brine. In order to apply cathodic protection in this research's environment, the operating parameters of E_{prot} and i_{prot} were required. The following Phase I experiment(s) were designed to mimic protecting carbon steel submerged in saturated brine and determine E_{prot} and i_{prot}.

Two separate experiments were performed where a coated AISI 1018 carbon steel pipe sample (25.4 mm diameter, 102.5 mm in length) was submerged vertically in saturated potash brine. The pipe was placed in the 3-D printed apparatus previously shown in Section 3.3.4. The pipe sample was subsequently placed under cathodic protection using a magnesium rod submerged 15 cm away in the same brine.

The first experiment was performed to determine E_{prot}. Once the pipe and magnesium were submerged in the brine and electrically connected, the system was left for 30 minutes to allow the cathodic protection current to stabilize. After 30 minutes, the open-circuit potential between the electrolyte and the inner pipe wall was recorded using the potentiostat in conjunction with a KCl salt bridge and an SCE. These potential measurements may also be called structure-to-electrolyte potentials. For more detail on the open-circuit mode of the potentiostat, refer to Section 3.3.2. During E_{prot} experiments, structure-to-electrolyte potentials were taken at various depths through the center of the pipe by lowering a reference electrode in 5 mm intervals. The electrode was lowered from the top to the bottom edge, a total length of approximately 100 mm and a total of 20 measurements. The experiment was repeated a minimum of three times, allowing two hours in-between experiments for the pipe metal to rest. The potentials measured

through the pipe center could be analyzed to determine E_{prot}. Additional open-circuit potentials were measured between the pipe wall and the electrolyte while the pipe was not cathodically protected. Comparing the potentials from the protected and unprotected steel displayed the overpotential. The overpotential could verify if the protection criteria was achieved.

The second experiment was used to determine i_{prot}. The coated steel pipe was submerged in potash brine and protected galvanically using the magnesium rod. A multimeter connected in between the magnesium rod and the steel pipe measured the current supplied to the steel. Dividing the average current measured once the system had stabilized by the inside surface area of the pipe produced i_{prot}. A current reading was taken every five minutes over the course of one hour to develop a plot of i_{prot} over time.

3.4.2 Phase II Experiments – ICPS Verification and Operating Procedure

The objectives of this research required the ICPS apparatus to be developed, as previously discussed in Section 3.3.5. The ICPS was used to protect the inside surface of a carbon steel elbow while attached to the flow loop during slurry flow. Using the ICPS, experiments verified the functionality of the system and developed the general procedures for its operation. A single experiment was performed using the ICPS on the flow loop. This experiment verified the ICPS was sufficiently protecting the inside of an elbow and gathered preliminary data. The preliminary data was collected to observe the effect of slurry concentration and flow velocity on the i_{prot}. This data aided in defining future experimental parameters.

In the experiment performed, the ICPS was used on the flow loop to cathodically protect a carbon steel elbow at a static potential of -1.10 V_{SCE}. The static potential was determined in Phase I experiments. The flow loop was filled with 18 L of 0.5 M sodium chloride brine. Four trials were performed protecting the elbow at flow velocities of 2.5, 3.0, 3.5, and 4.0 m/s. During each flow velocity trial, the slurry concentration was increased by adding silica sand in 10 wt.% steps to a maximum of 30 wt.%. At each flow velocity and slurry concentration, the elbow was cathodically protected for 220 seconds. During cathodic protection, the potentiostat measured and recorded the current required to hold the metal at the static potential. When the measured current was divided by the inner surface area of the elbow, i_{prot} could be determined and plotted

against the changing variables. Table 3.7 shows the test trials performed during the ICPS verification experiment. The data collected at each slurry concentration and flow velocity aimed to show how i_{prot} varied during different operating conditions. This experiment also ensured the ICPS could cathodically protect the elbow for future experiments and provided data that aided in the experimental design of future phases.

Table 3.7. ICPS trial testing on the flow loop using 0.5 M NaCl brine and 1.05 mm silica sand particles.

Experiment	Slurry Velocity (m/s)	Slurry Concentration (wt.%)
1	2.5	0
		10
		20
		30
2	3.0	0
		10
		20
		30
3	3.5	0
		10
		20
		30
4	4.0	0
		10
		20
		30

Many different electrochemical experiments could be performed using the ICPS apparatus. The two specific electrochemical tests performed within this research using the ICPS in conjunction with the potentiostat include:

1) Potentiostatic Mode (Cathodic Protection):

    - In this setup, all three electrodes were connected to the potentiostat, and the system software was programmed to hold the WE to a user set potential with respect to the RE. The potentiostat impressed the required current between the CE and WE to meet the user set potential. During potentiostatic mode operation, the

system software records the potential (V), current (A), and elapsed time (s). Within the system software, the user can define how many data points (voltage and current pairs) were recorded every second. The potentiostatic mode was used in this research to impress cathodic protection on the elbow specimen.

2) Open-circuit Mode:

- This mode only required the WE and RE to be connected to the potentiostat. In open-circuit mode, the software measured the potential of the WE with respect to the RE. The voltage was recorded over any duration of time specified, and the time between subsequent voltage measurements could be set.

Throughout the future experimental phases of this research, the above procedural ICPS mode(s) are used and referenced.

3.4.3 Phase III Experiments - Effect of Slurry Concentration and Flow Velocity on i_{prot}

Phase III experiments focussed on exploring the effect various flow loop operating conditions have on the current density required to protect the carbon steel elbow. The experiments were primarily designed to observe the role erosion had on the corrosion rate during erosion-corrosion. By measuring the i_{prot} required to protect the elbow, the effect of erosion on corrosion was observed. Phase III experiments observed three trends:

1. The effect of slurry concentration on i_{prot}
2. The effect of particle size on i_{prot}
3. The effect of flow velocity on i_{prot}

The first experiment(s) observed the effect of slurry concentration and flow velocity on i_{prot}. These experiments consisted of adding 18 L of saturated potash brine to the flow loop, choosing a flow velocity (2.5, 3.0, 3.5, or 4.0 m/s), and adding sand to the flow loop in small step sizes to increase the slurry concentration. Slurry concentration was added using standard quartz silica sand with an average nominal diameter of 1.05 mm. The sand was increased by 1 wt.% steps, from 0 to 35 wt.%. At each slurry concentration, the elbow was cathodically protected using the

ICPS for 220 seconds. The elbow was held at an E_{prot} of -1.20 V_{SCE}, a value chosen from data collected in Phase I experiments. The setup and operation of the ICPS follow the procedure(s) in Section 3.3.2. At each slurry concentration, the protection current in amps (A) along with the elapsed time in seconds (s) were measured and recorded. Once the elbow had been cathodically protected at all slurry concentrations at the fixed flow velocity, the experiment was complete. This experiment was repeated for each new flow velocity. Similarly, the experiment was repeated using a smaller sand size of 0.55 mm to observe the effect of particle size on i_{prot}. A new elbow was inserted for each experiment. Table 3.8 displays all experimental conditions.

Table 3.8. Experimental conditions tested for finding the effect of solids concentration and size on i_{prot}.

Particle Size (mm)	Slurry Velocity (m/s)	Slurry Concentration (wt.%)
1.05	2.5	0 - 35
	3	0 - 35
	3.5	0 - 35
	4	0 - 35
0.55	2.5	0 - 35
	3	0 - 35
	3.5	0 - 35
	4	0 - 35

Data from Phase III experiments were performed such that data sets measured at different flow velocities were comparable to each other. Having comparable data sets was done by measuring a datum point before each experimental run on the flow loop. The datum point was the i_{prot} measured at a flow velocity of 2.5 m/s and a slurry concentration of 0 wt.%. The value of i_{prot} at the datum was determined by averaging i_{prot} over nine experimental trials at the datum conditions. Once the datum and confidence interval was known, before any future experiment began, the flow loop was set to a flow velocity of 2.5 m/s and a slurry concentration of 0 wt.%, and i_{prot} was measured. If the i_{prot} measured at the datum corresponded to the known average, the experiment proceeded. The datum point method for data collection on the flow loop was used for both particle sizes.

3.4.4 Phase IV Experiments - Determining the Correlation between i_{prot} and Corrosion Rate

In this research, it was presumed that $i_{prot,}$ and the corrosion rate it inhibits, are related and can be described by a correlation. Additionally, the correlation between i_{prot} and the corrosion rate was assumed to be specific to the environmental conditions; the same correlation may not fit all environments (i.e. electrolytes). Phase IV of this research performed experiments to determine the correlation between i_{prot} and corrosion rate. In these experiments, the corrosion rate of the elbow was measured at select slurry concentrations and flow velocities used in Phase III research. The measured corrosion rates could then be plotted against i_{prot} to determine a correlation.

The method chosen to measure the corrosion rate of the elbow was found in a journal paper written by Postlethwaite in 1974. Postlethwaite's method used a combination of simple electrochemical tests that better handle the current and voltage measurement fluctuations caused by slurry flow. The general process followed six steps:

1. Choose a set of operating conditions (flow velocity and slurry concentration).
2. Measure E_{corr} of the elbow at the chosen operating condition using the ICPS in open-circuit mode.
3. Deoxygenate the flow loop to inhibit corrosion on the elbow.
4. Use the ICPS in potentiostatic mode to hold the elbow at the measured E_{corr} and record the corresponding current density required. This current density is i_{corr}.
5. Using Faraday's equation, convert i_{corr} into a corrosion rate.
6. Repeat steps 2 – 6 for another set of operating conditions.

Postlewaite's method was reproduced in this research using two experiments performed in series. The first experiment measured E_{corr} and the second measured i_{corr}.

During E_{corr} experiments, a new carbon steel elbow was placed into the ICPS and attached to the flow loop. The flow loop was filled with 18 L of saturated potash brine and set to the desired flow velocity and slurry concentration. Once the flow loop was operating, the potentiostat was set to open-circuit mode to measure E_{corr}. The experiment measured the open-circuit potential for 5-6 hours, allowing E_{corr} to stabilize. The data recorded included the open-circuit potential (E_{corr}) in volts (V) and the duration in seconds (s). Upon completion, the flow loop was drained and

cleaned. This experiment was repeated for six different slurry concentration and flow velocity pairs. All operating conditions chosen for Phase IV experimentation were previously used in Phase III experiments. The chosen operating conditions ensured there was a corresponding i_{prot} measured at the same flow velocity and slurry concentration for comparison in the correlation.

The second experiment measured the i_{corr} required to hold the elbow at the recorded E_{corr}. The i_{corr} was measured by deoxygenating the flow loop and using the ICPS to hold the elbow at E_{corr}. Postlethwaite's method states that the current required to hold the elbow at E_{corr} is the same amount of current as i_{corr}. The experiment began by filling the flow loop with 18 L of saturated potash brine and setting the slurry concentration and flow velocity to one of the same operating conditions E_{corr} was measured. The brine was deoxygenated using nitrogen gas fed at 2 g/s into the slurry container of the flow loop. The top of the slurry container was wrapped in saran wrap and sealed to ensure no oxygen leaked into the flow loop. During deoxygenation, the slurry flow was set to 2.5 m/s and purged of oxygen for approximately an hour. A Hanna dissolved oxygen (DO) meter (Model #: HI98193) ensured the DO content was zero before electrochemical measurements began. Once the brine was deoxygenated, the ICPS held the elbow at E_{corr} for 220 seconds. The experiment measured the current (A) to achieve $E_{corr,}$ and the elapsed time (s) the experiment was performed. This procedure was repeated at every slurry concentration and flow velocity pair that E_{corr} was measured. The i_{corr} is determined by dividing the current required to hold the elbow at E_{corr} by the inside surface area.

The slurry concentration and flow velocity pairs chosen for Phase IV experiments were selected such that the entire range of i_{prot} measured in Phase III was represented. Table 3.9 shows the six slurry concentration and flow velocity pairs used for both E_{corr} and i_{corr} experiments. The first five pairs shown in the table were used to create the correlation between the i_{corr} and corrosion rates. The sixth pair, bolded in the table, was used as a validation point and was selected at random. Once the correlation was made, it was used to predict the corrosion rate at the slurry concentration and flow velocity of the validation point (5.0 wt.% and 2.5 m/s). The predicted corrosion rate could be compared to the actual corrosion rate measured at the validation point.

Table 3.9. Experimental conditions used to measure E_{corr} and i_{corr} to create a correlation between i_{prot} and corrosion rate.

Slurry Velocity (m/s)	Slurry Concentration (wt.%)
2.5	0
3	0
3.5	0
4	0
4	5
2.5	**5**

3.4.5 Statistical Analysis

All data attained for this thesis was performed to meet a 95% confidence interval, as found using the Student's t-test. Phase I results were repeated 3-9 times, depending on the type of experiment performed. Confidence intervals for Phase I data were calculated according to the number of repetitions performed for each data point. Data collected from experiments performed on the flow loop was time-consuming and laborious. For this reason, the statistical error associated with the flow loop data in Phase III was represented by repeating the initial experiment at a flow velocity of 2.5 m/s, from 0 to 35 wt.% slurry concentration, a total of nine times. The confidence interval calculated was applied to all later flow loop experiments performed at higher flow velocities. This confidence interval method for the flow loop data was also repeated when the sand size was changed. The above method drastically reduced the number of experiment iterations required while still providing meaningful and statistical significance to the flow loop data. Experiments in Phase IV repeated each data point between 3-6 times to calculate confidence intervals. The Student's t-test was utilized to determine the uncertainty in the experiments as the sample sizes in this thesis are small, and the standard deviation of the population was unknown. The statistical uncertainty was calculated using Eq. [3.1] below:

$$P = t \cdot \frac{S}{\sqrt{N}} \qquad [3.1]$$

where P is the random uncertainty of the sample measurement, t is the statistical value as found in a t-distribution table for various confidence levels, S is the standard deviation of the sample, and N is the number of samples in the data set.

The value of t is dependant on the degrees of freedom (n) associated with the sample size (where n is the sample size (N) less one) as well as the level of confidence selected. As many different experiments were performed throughout this thesis, the t value varied from experiment to experiment. The t values used to calculate the uncertainty for each experiment are shown in Table 3.10, along with the sample size and specific conditions.

Table 3.10. List of t-values used for 95% confidence intervals in all performed experiments.

Experiment Type			**Sample Size "*N*"**	**t-value**
Phase	**Description**	**Conditions**		
I	E_{prot} measurement at various depths through the center of an AISI 1018 pipe in saturated potash brine	0 - 102.5 mm	9	1.86
I	i_{prot} experiments for AISI 1018 pipe submerged in saturated potash brine	-	3	2.92
III	The effect of 1.05 mm sand on the i_{prot} of AISI 1018 elbows	2.5 m/s 0 to 35 wt.%	9	1.860
III	The effect of 0.55 mm sand on the i_{prot} of AISI 1018 elbows	2.5 m/s 0 to 35 wt.%	10	1.833
IV	Measurement of E_{corr} for the AISI 1018 elbows	2.5, 3.0, 3.5, and 4.0 m/s 0 wt.%	4	2.353
IV	Measurement of E_{corr} for the AISI 1018 elbows	4.0 m/s 5 wt.%	3	2.920
IV	Measurement of E_{corr} for the AISI 1018 elbows	2.5 m/s 5 wt.%	5	2.132
IV	Measurement of i_{corr} for the AISI 1018 elbows held at E_{corr}	2.5, 3.0, 3.5, and 4.0 m/s 0 wt.%	5	2.132
IV	Measurement of i_{corr} for the AISI 1018 elbows held at E_{corr}	2.5 and 4.0 m/s 5 wt.%	6	2.015

4. Results and Discussion

4.1 Introduction

This section presents the results and discussion from each of the experimental phases presented in Section 3 (Phase I through Phase IV). All experimental data recorded is contained in Appendix A-D. Experiments conducted in Phase I determined the electric potential required for cathodic protection of an AISI 1018 carbon steel pipe submerged in stationary saturated potash brine. Phase I findings of E_{prot} and i_{prot} are shown and discussed. Experimental results from Phase II (for testing of the ICPS in a dilute NaCl brine) demonstrate the viability of the ICPS to protect carbon steel elbows in the flow loop. Experimental results from Phase III show the relationships between i_{prot} and the slurry concentration and flow velocity. A further discussion of the results from Phase III explores the relationship between particle size and i_{prot} at various slurry concentrations and flow velocities. Experimental results from Phase IV assist in correlating i_{prot} to the internal corrosion rate. The importance of critical findings from the correlation were also explored. Combining the results from Phase III and IV, the effect of slurry concentration, particle size, and flow velocity on the internal corrosion rate were analyzed. Further analysis quantified the synergistic corrosion experienced by the carbon steel elbow under various flow velocities and slurry concentrations.

All the results discussed serve to meet the objectives of this thesis, namely, to explore the use of cathodic protection inside of pipelines and to find the effect of a second phase on the corrosion experienced in carbon steel elbows.

4.2 Phase I Results – Determining E_{prot} and i_{prot} in Saturated Potash Brine

4.2.1 Determining i_{prot}

The magnitude of the protection current for AISI 1018 in a potash brine was investigated to determine an appropriate power source for the ICPS. It was assumed that a magnesium anode would provide suitable galvanic protection in this environment and provide reasonable current requirements. According to methods described in Section 3.4.1, a magnesium anode was used to

protect an outer coated AISI 1018 carbon steel pipe galvanically. From the experiments, the i_{prot} was measured and plotted against time, as shown in Figure 4.1. The plot displays the averaged results of the experiment over three iterations with a confidence interval of ±0.31 mA/cm^2. The observed trend showed that when cathodic protection was first applied, there was an initial increase in the amount of current density required to protect the steel. The increase continued until it reached a maximum after approximately 10 minutes. After this maximum, the magnitude of current density decreased and gradually approached a value of approximately 1.10 mA/cm^2. This value of 1.10 mA/cm^2 was then assumed to be the i_{prot} required to inhibit corrosion on AISI 1018 carbon steel in a stagnant potash brine.

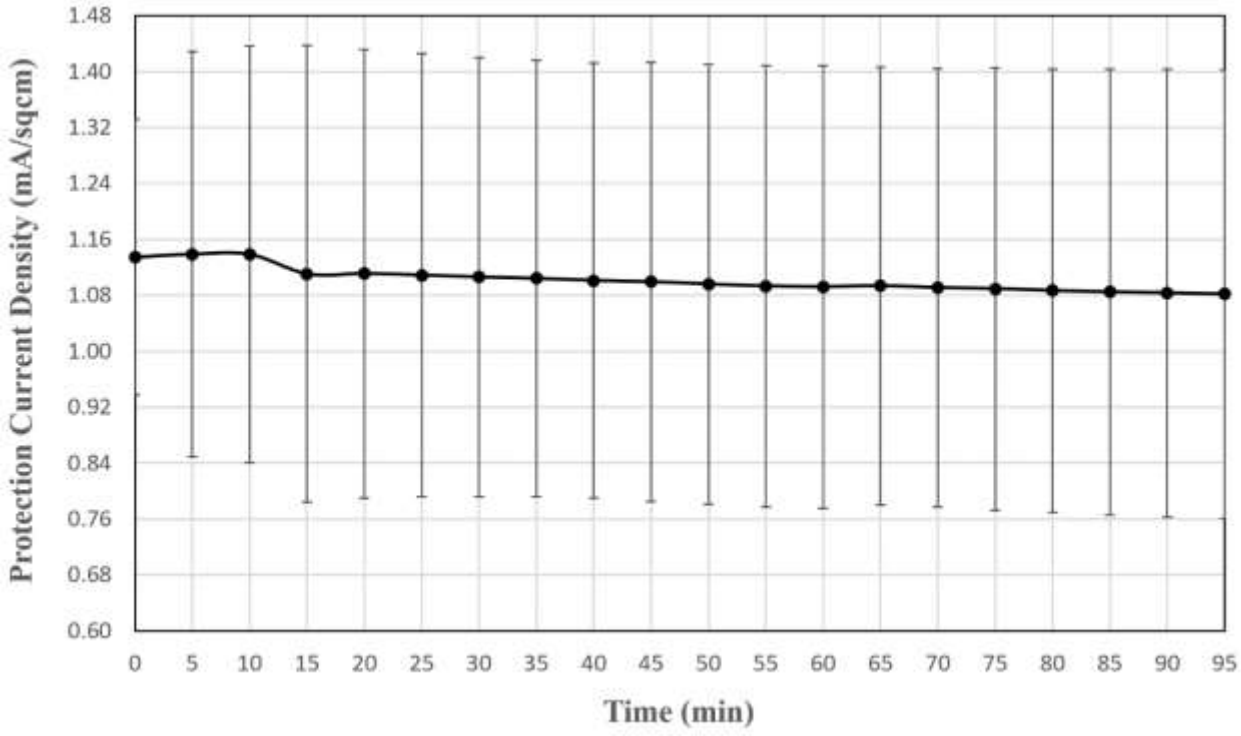

Figure 4.1. The i_{prot} required to protect the inner surface of an AISI 1018 carbon pipe submerged in stagnant saturated potash brine.

The value of i_{prot} (1.10 mA/cm^2) was used to estimate if the Parstat 3000 would be capable of providing cathodic protection to the carbon steel elbows in future experiments. Based on the inner surface area of the elbow and the i_{prot}, it was determined the potentiostat was required to

supply 55 mA to protect the elbow; well below the 1 A upper operating limit of the Parstat 3000. These results determined that the Parstat 3000 was adequate to provide cathodic protection to the carbon steel elbows. See Appendix A for all raw and calculated data in Phase I experiments.

4.2.2 Determining E_{prot}

Following the methods as described in Section 3.4.1, the E_{prot} required to inhibit corrosion of AISI 1018 carbon steel in stagnant saturated potash brine was determined. This experiment observed the structure-to-electrolyte potentials at various depths through the pipe and explored how cathodic protection behaves inside a fully submerged pipe. Upon completion of the experiments, the potentials were plotted against depth and are shown in Figure 4.2. The plot displays an average confidence interval of ±5 mV. From the plot, 0 mm is defined as the top edge of the pipe, while 102.5 mm is the bottom edge. The parabolic curve of the potential as the measurements were taken throughout the pipe center showed different levels of polarization were occurring at different depths. The pipe ends had a higher overpotential when compared to the center of the pipe. The parabolic curve denotes the attenuation of potential within the pipe from the application of cathodic protection. Generally, due to the size of the magnesium anode used in the experiment, the whole system at every depth tested should be sufficiently protected. From the plot, it was determined that the least over-protected potential at the center of the pipe (depth = 50 mm) was a stable value to define as E_{prot}. Although the E_{prot} at 50 mm was -1.21 V_{SCE}, the chosen E_{prot} was rounded up to -1.20 V_{SCE} to account for the magnesium likely over-polarizing the metal.

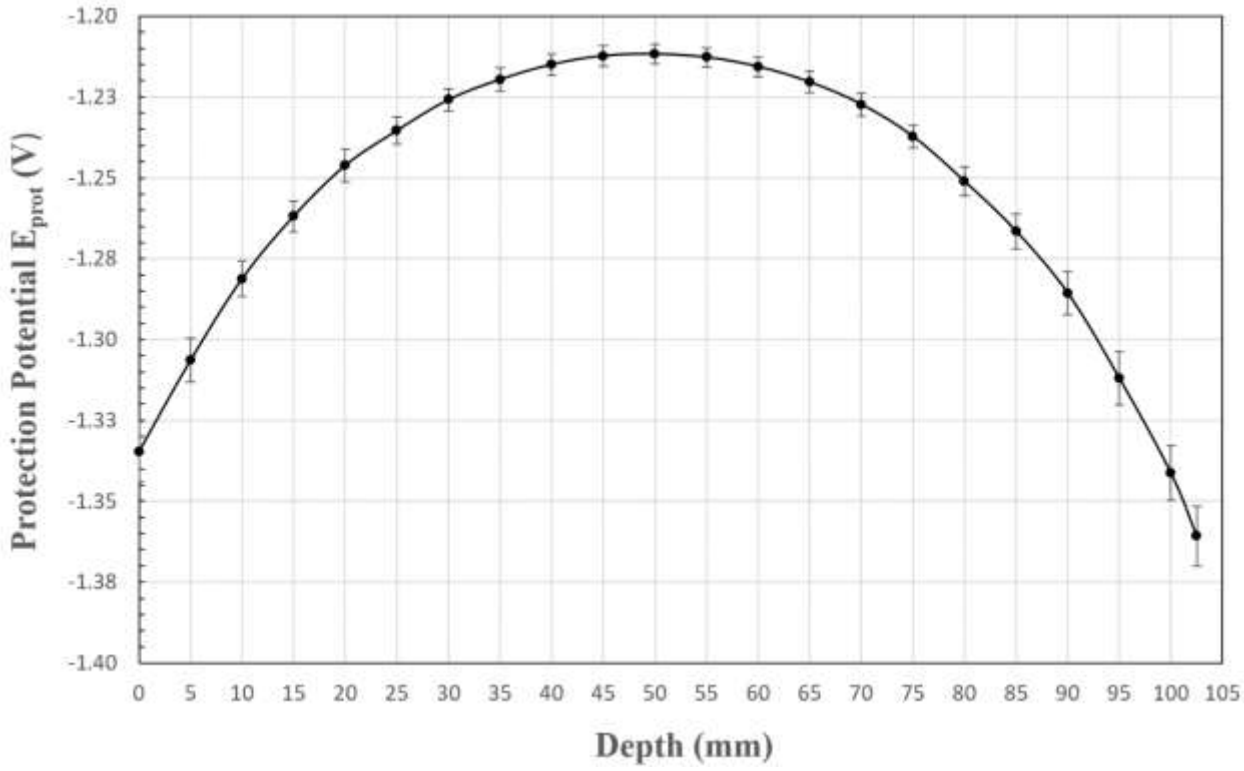

Figure 4.2. Measurement of E_{prot} from applying galvanic cathodic protection on an AISI 1018 carbon steel pipe in saturated potash brine measured at various pipe depths.

Further experimentation was performed due to the parabolic potential curve observed in Figure 4.2. The experiments aimed to determine if the parabolic trend was caused by the composition of the potash solution or by properties of electric fields acting within the pipe. The same above experiment performed in a saturated potash brine was performed in various other brines, as prior conceptions held the potential through the pipe should have been uniform. Therefore, the experiment was re-performed in saturated NaCl, KCl, and $MgCl_2$ brines to find the effect brine composition had on the structure-to-electrolyte potential through the pipe. The results from these experiments were plotted and are shown in Figure 4.3. The plot showed that each brine exhibited a parabolic structure-to-electrolyte potential trend, similar to the saturated potash brine results. The saturated NaCl solution showed the least parabolic trend. Saturated $MgCl_2$ brine experienced the steepest and most severe potential change of all brines tested. Pure KCl seemed to mimic the curve of the potash brine with the addition of a small negative step change. The similar results between pure KCl and potash brine intuitively align as potash is almost entirely KCl. It was

ultimately determined that the composition of the potash solution did not cause the parabolic trend of the structure-to-electrolyte potential, as many brines showed similar behaviour.

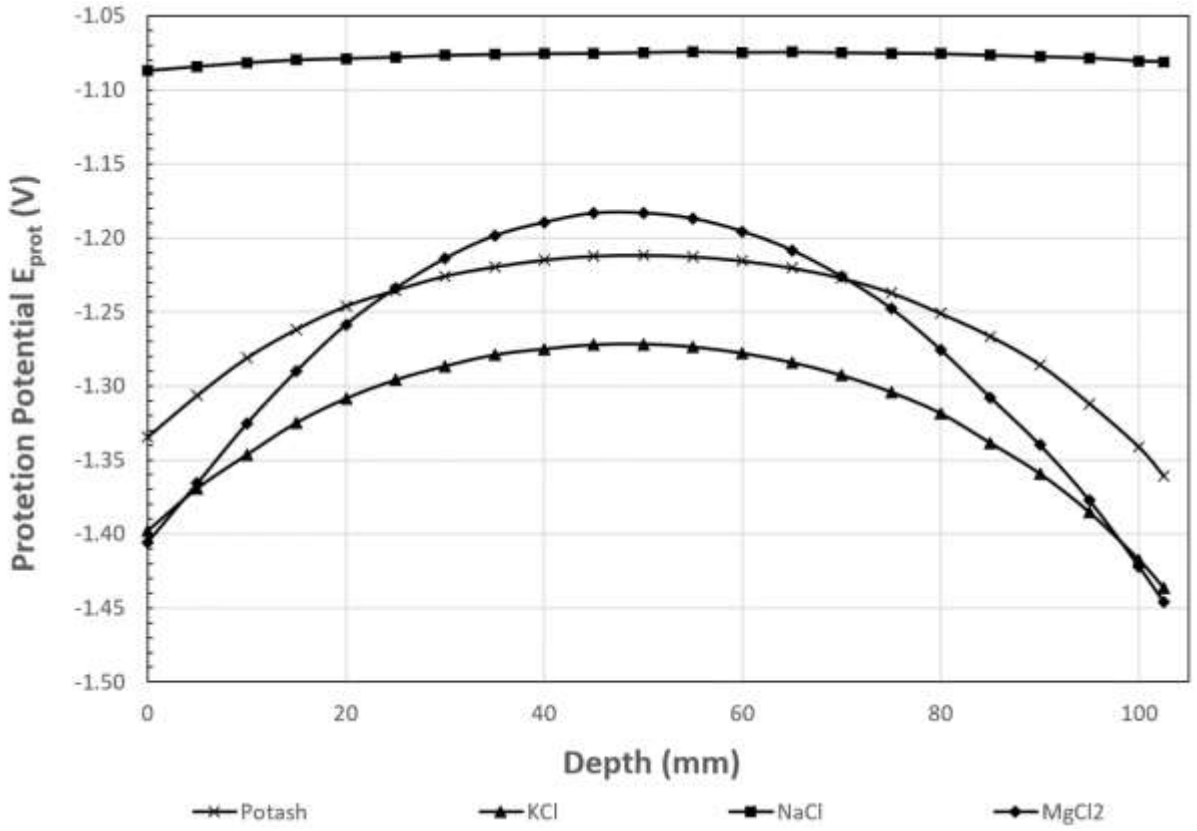

Figure 4.3. Measurement of E_{prot} from applying galvanic protection to an AISI 1018 carbon steel pipe in stagnant saturated brines of NaCl, pure KCl, $MgCl_2$, and potash measured at various pipe depths.

4.2.3 Discussion of Phase I Results

Phase I determined that the E_{prot} required to protect carbon steel submerged in saturated potash brine was approximately -1.20 V_{SCE}. To confirm this measured voltage likely inhibits corrosion in the potash brine, a Pourbaix diagram depicting a similar iron-chloride-water environment was consulted (see Figure 4.4). The Pourbaix diagram shown below was created using saturated NaCl (7 M) at 25 °C as the electrolyte. While the Pourbaix diagram is not using the same salt as this research (NaCl instead of KCl), the chloride ion is the major contributor to the corrosiveness of

the environment. Therefore, the concentrated NaCl solution should closely relate to saturated KCl within reason. From the displayed Pourbaix diagram, at a neutral pH of 7, the immunity region is found at potentials more electronegative than -0.625 V_{SHE}. Converting the measured E_{prot} of -1.20 V_{SCE} into terms of a SHE, a value of -0.956 V_{SHE} was calculated. This placed E_{prot} well within the theoretical immunity region for iron in a saturated chloride solution. While the use of Figure 4.4 does not provide exact verification of protection, it does provide a good approximation.

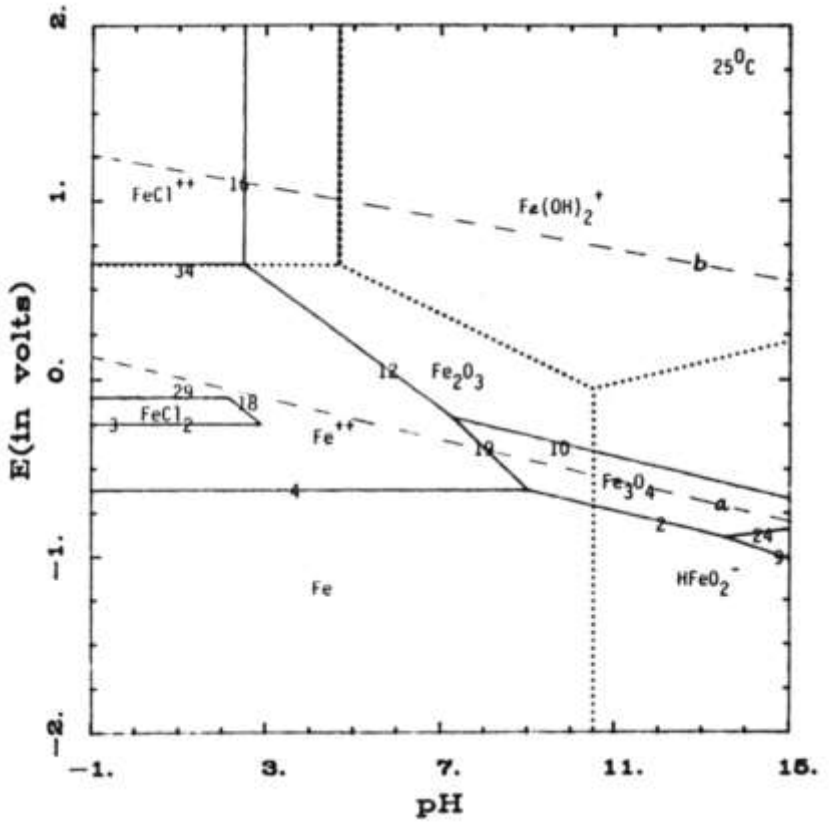

Figure 4.4. Pourbaix diagram of Fe-Cl-H_2O in saturated 7 M NaCl at 25 °C - reproduced from Kesavan *et al.* (1959) with permission from NACE International.

As discussed in the literature review, a similar experiment cathodically protected AISI 1018 carbon steel in a slurry pot by lowering the potential to -0.90 V_{SCE} to inhibit corrosion (Lu and Luo, 2006). While -0.90 V_{SCE} is less electronegative compared to the potential of -1.20 V_{SCE}

measured in this research, the solution used by Lu and Luo was process-recycled cooling water with low concentrations of ions, and zero chlorides. As chlorides are a significant contributor to corrosion, highly chlorinated environments may require a more electronegative potential to inhibit corrosion.

The current density required to protect the carbon steel in saturated potash brine was measured to be 1.10 mA/cm^2. In conventional cathodic protection on external structures, a current density of 0.001-0.021 mA/cm^2 (1-20 mA/ft^2) is typical depending on the resistance of the environment (Applegate, 1973). The measured i_{prot} for carbon steel in saturated potash brine represents anywhere from 50-1100 times the current density required for external structures. While the measured i_{prot} was large, when the approximate resistances of the two environments were accounted for, the results are clearer. Typical soil environments have resistivities of 10-10000 Ohm·m, depending on the soil composition and moisture content (Syed and Siddiqui, 2012). Typical saturated salt solutions such as concentrated KCl will have near-zero resistivities. The low resistance associated with concentrated electrolytes creates an environment in which the throwing power required (the ability to pass current) increases drastically as the resistivity decreases (Evitts, 2005). Industrial applications of cathodic protection have confirmed this as impressed systems cannot efficiently push the large currents required to protect piping in low resistance solutions (Evitts, 2005). The low resistance of the potash brine and resulting high throwing power may be why the i_{prot} to protect the carbon steel was relatively high.

Due to the values of E_{prot} and i_{prot} required to protect carbon steel in this research, hydrogen embrittlement of the steel was considered. Cathodic protection is a known cause of embrittlement from the high number of reduction reactions occurring on the working electrode, which creates hydrogen gas. Hydrogen embrittlement occurs from individual hydrogen atoms diffusing into the metal surface by weakening the cohesion of the lattice (Schmidtchen, 2009). The diffusion of hydrogen into the metal occurs from the creation of a concentration gradient. Experiments by Zheng *et al.* (2000) applied cathodic protection on steels over a wide range of negative potentials and current densities during erosion-corrosion and measured the mass loss. The experiments showed that all samples had the same mass loss regardless of the severity of cathodic protection applied. Zheng concluded that had hydrogen embrittlement occurred at lower cathodic potentials, the mass loss should have increased from more significant wear on the

weaker metals. Additonally, Yao *et al.* (1995) performed similar experiments and also confirmed that mid-range cathodic potentials could inhibit corrosion without additional wear from hydrogen embrittlement. The research in this thesis applied cathodic protection in 220-second intervals with total experiments lasting no longer than 3-hours, less than the 4-hour experiments performed by Zheng. From the above literature, hydrogen embrittlement was determined to be a consideration for discussion, but not a concern for experimentation.

Phase I plots showed that the E_{prot} measured through the center of a coated, submerged pipe in potash brine was parabolic in shape. These results were re-tested in various brines to ensure the trend was not specific to potash brine. Each brine tested experienced the same parabolic trend, confirming the trend was a natural function of applying cathodic protection to submerged pipes in salt electrolytes. A similar experiment was performed in seawater by Morgan in 1959 (Morgan, 1959). In Morgan's experiment, E_{prot} was measured at various depths through an externally coated carbon steel pipe half-submerged in seawater. Figure 4.5 shows the results Morgan's experiment. Morgan's results showed that the protection potential decreased from -0.70 to -1.10 V_{SCE} from the center of the pipe (at the surface of the electrolyte) to the pipe end. This result matches the parabolic trends observed in Phase I for all brines tested. Phase I experiments showed E_{prot} being highest at the center of the pipe, curving slowly to more electronegative potentials near the pipe ends. Morgan's study provides evidence that confirms the parabolic trends observed in Phase I. Continued discussion in Morgan's research mentions the curves matched those predicted by mathematics; however, he does not provide any explanation or citations that confirm the relationship.

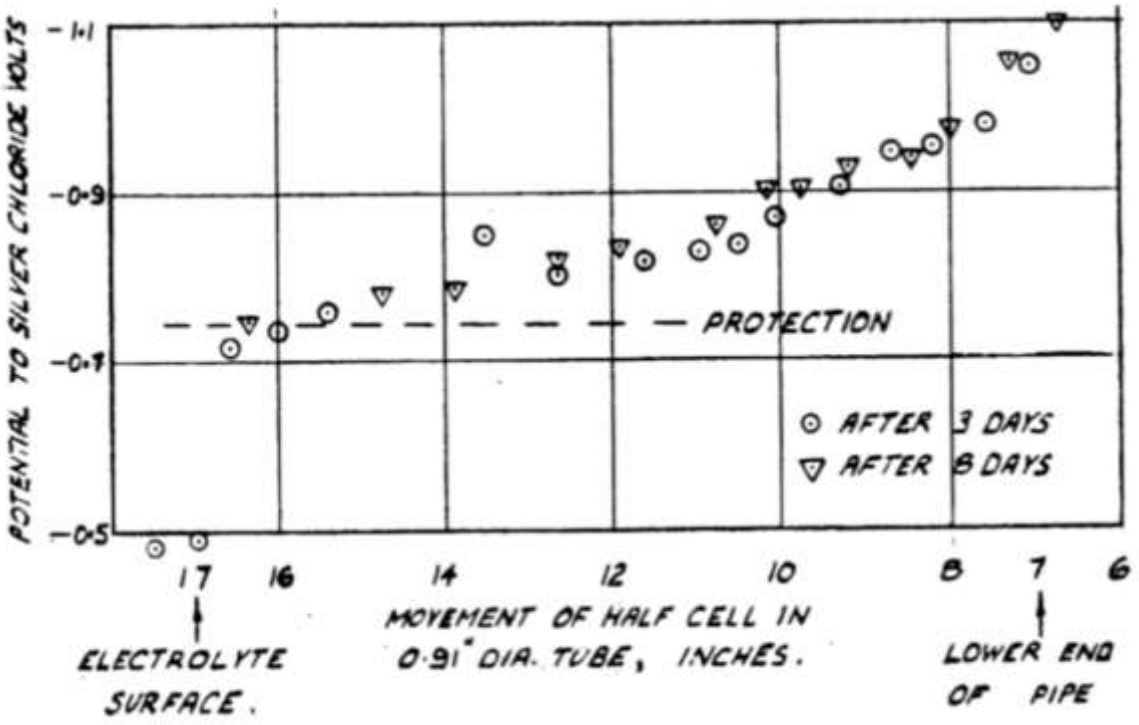

Figure 4.5. E_{prot} measured through the center of a 0.91-inch diameter coated carbon steel pipe half submerged in seawater – As measured from the electrolyte surface to the pipe end – reproduced from Morgan (1959) with permission from NACE International - Corrosion Society.

4.4 Phase II Results – ICPS Verification

4.4.1 ICPS Verification Test

Upon completing the design and fabrication of the ICPS, the apparatus was tested by cathodically protecting the elbow samples during slurry flow on the flow loop. The experiments were performed to gather preliminary data on erosion-corrosion and verify/troubleshoot the ICPS. In these experiments, an elbow was placed under cathodic protection in dilute NaCl brine. While under cathodic protection, flow velocity and slurry concentration were changed while measuring the current required to protect the steel. The experiments followed the methods outlined in Section 3.4.2. A sample of the data measured at a flow velocity of 3.0 m/s and a slurry concentration of 10 wt.% is shown in Figure 4.6. The current required to protect the elbow (i_{prot}) was found by averaging the current between 60-220 seconds. This method of averaging the

cathodic current between the 60-220 seconds was the standard method used to determine the i_{prot} for all experiments in Phase III and IV as well. The 60-220 second time interval was chosen qualitatively. As seen in Figure 4.6, after 60 seconds of cathodic protection, the current became stable, forming a horizontal line. The trend of current stability past 60 seconds was observed in all cathodic protection experiments.

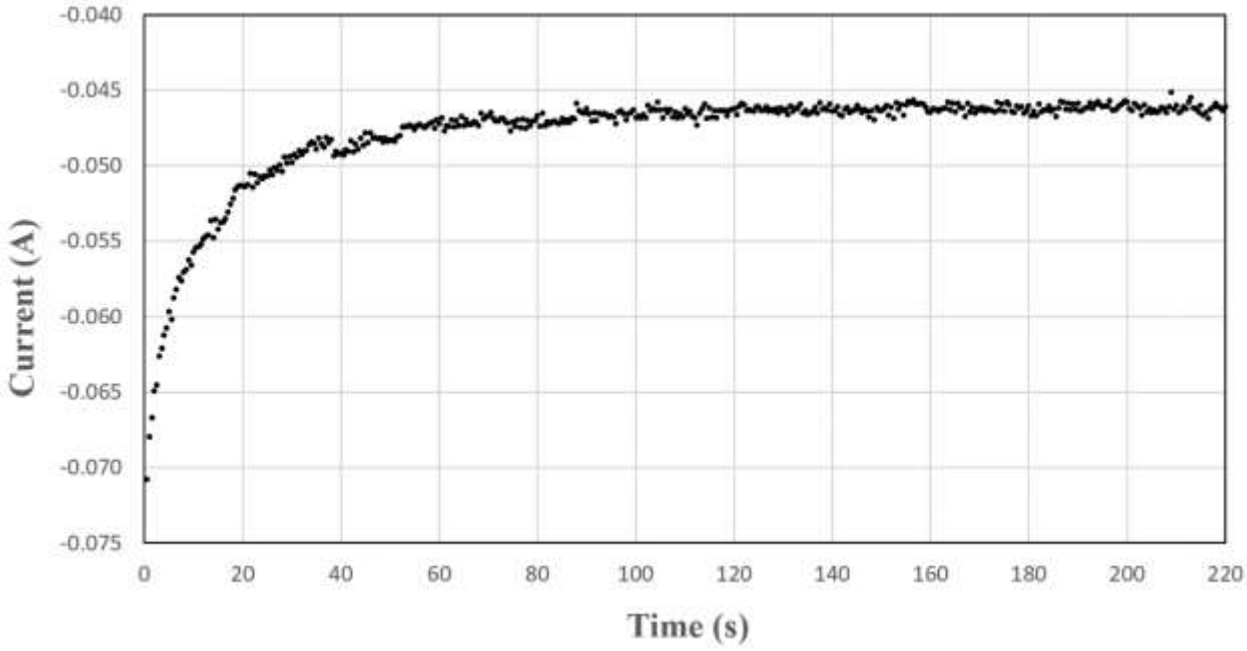

Figure 4.6. Raw data attained from the cathodic protection of an AISI 1018 carbon steel elbow at 3.0 m/s and 10 wt.% slurry concentration.

The results from Phase II experiments are shown in Figure 4.7. This figure shows a plot of i_{prot} as a function of flow velocity at various slurry concentrations. As this experiment was intended to verify the functionality of the ICPS, the experiments were not repeated and do not have error bars. However, the results were relevant as it showed how to gather data using the ICPS, how to analyze the data, and the general trends observed while varying flow velocity and slurry concentration, trends that would be later explored in detail. It is evident from the figure that there is a relationship between flow velocity and slurry concentration on the amount of i_{prot} required to protect the elbow. Generally, as the flow velocity of the slurry increased, i_{prot} increased in response. Slurry concentration, conversely, showed a more complicated relationship with i_{prot}.

From slurry concentrations between 0 to 10 wt.%, i_{prot} was shown to increase. Past 10 wt.%, i_{prot} decreased sequentially at each higher slurry concentration. The rise and fall of i_{prot} suggest there is a non-linear relationship between slurry concentration and i_{prot}. It is also interesting to note how the addition of solids (sand) affected the slope of the current trend lines. Trend lines for slurry concentrations of 10, 20 and 30 wt.% all exhibited similar slopes, while the slurry concentration at 0 wt.% showed a steeper rate of change. This relationship was most apparent between the 0 wt.% and the 30 wt.% trend lines. As such, the addition of solids was observed to weaken the effect flow velocity had on i_{prot}. This finding predicts an interaction between flow velocity and slurry concentration that affects the corrosion occurring on the surface of the elbow. All raw and calculated data from Phase II experiments can be found in Appendix B.

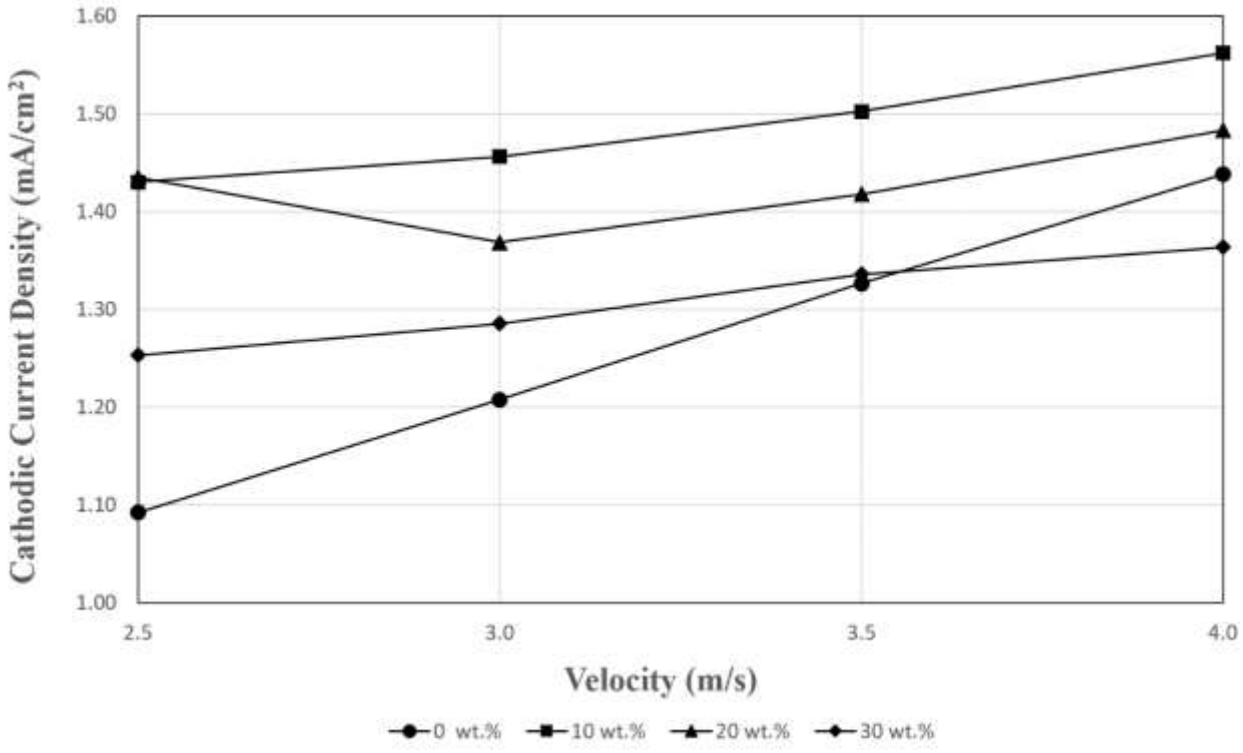

Figure 4.7. Experimental results from the ICPS showing the cathodic current density as a function of flow velocity at 0, 10, 20, and 30 wt.% solids concentration in 0.5 M NaCl brine.

4.4.2 Discussion of Phase II Results

During Phase II experiments, i_{prot} was determined from data recorded using the ICPS. The analysis chosen to determine i_{prot} averaged the protection current density between 60-220 seconds of cathodic protection. The chosen time interval i_{prot} was averaged over was selected as the protection current density stabilized to a linear line after 60 seconds. In situations where the potential response is slow, which may be the case in higher resistance environments or when the anode and cathode are far apart, the time required to reach a stable current density may be more substantial. Due to this research's electrolyte being a low resistance, the close proximity of the anode to the cathode, and small surface area being protected, the time required for the current to stabilize was short.

The test findings of the ICPS were influential to observe the response of i_{prot} from changing flow velocity and slurry concentration. However, as the experiments were not repeated, the findings had relatively low significance. Phase II experiments mainly aided in the design of Phase III and IV experiments. While the results of Phase II experiments did not provide concrete evidence for their findings, many of the results shown were confirmed in later experiments.

4.5 Phase III Results – The Effect of Flow Velocity, Slurry Concentration, and Particle Size on i_{prot}

4.5.1 Overview

Phase III experiments aimed to find the effect of flow velocity, slurry concentration, and particle size on the current density required to protect a carbon steel elbow in saturated potash-sand slurry flow. The experiments measured i_{prot} at flow velocities between 2.5 to 4.0 m/s and slurry concentrations from 0 to 35 wt.%. The experiments also utilized two particle sizes; a 1.05 mm diameter and a 0.55 mm diameter particle. Refer to Appendix C for data from Phase III experimentation.

4.5.2 The Effect of Slurry Concentration and Flow Velocity using 1.05 mm Sand

This section describes the results of Phase III experiments using the 1.05 mm particle size. The experiments and procedures follow the methodology stated in Section 3.4.3. Cathodic protection was applied to the elbow during flow loop operation at flow velocities of 2.5, 3.0, 3.5, and 4.0 m/s while changing the slurry concentration from 0 to 35 wt.% in 1% steps. During cathodic protection, i_{prot} was recorded for each step change.

As stated in the methodology for Phase III, datum points were used to ensure that data sets collected on the flow loop were consistent with each other. The datum was the i_{prot} measured at a flow velocity of 2.5 m/s and a slurry concentration of 0 wt.%. Experimental results over nine trials determined the datum point to have an average current density of 0.926 ± 0.070 mA/cm^2. Prior to each experiment at higher flow velocities, a datum measurement was performed. Table 4.1 shows the averaged datum measurements recorded prior to experiments performed at 3.0, 3.5, and 4.0 m/s. From the table, all experiments performed at higher flow velocities had average datums that match the value of 0.926 mA/cm^2 within the confidence interval. The matching datums ensure the data recorded was repeatable and comparable to each other.

Table 4.1. List of datum point measurements found at 2.5 m/s and 0 wt.% slurry concentration to ensure the comparability of data within different data sets at higher flow velocities.

Trial Flow Velocity (m/s)	**Datum Measurement at 2.5 m/s and 0 wt.% (mA/cm^2)**	**95% Confidence Interval (±mA/cm^2)**
2.5	0.926	0.070
3.0	0.888	0.070
3.5	0.902	0.070
4.0	0.909	0.070

The main experimental results using the 1.05 mm sand were plotted as i_{prot} as a function of slurry concentration and shown in Figure 4.8. From the figure, a complex relationship can be seen between slurry concentration and i_{prot}. At all flow velocities, i_{prot} increased with slurry concentration up to a peak, after which i_{prot} decreased with the further addition of sand. From Figure 4.8, the flow velocity trendlines at 2.5, 3.0, 3.5 and 4.0 m/s depict that i_{prot} is a maximum at slurry concentrations of 9, 8, 7, and 5 wt.%, respectively. As the flow velocity increased, the

amount of slurry concentration required to reach the maximum i_{prot} decreased. This result suggests that flow velocity and slurry concentration may have competing mechanisms that change the current density required to protect the elbow. Further investigation of Figure 4.8 shows at flow velocities of 2.5, 3.0, and 3.5 m/s, i_{prot} decreased substantially with the further addition of sand past the peak i_{prot}. At the flow velocity of 4.0 m/s, i_{prot} remained constant beyond 5 wt.% slurry concentration. While the trendlines produced in the figure all follow a similar shape, there is a slightly more considerable shift in i_{prot} between the flow velocities of 3.0 and 3.5 m/s compared to the others.

From an industrial perspective, the results showed that regardless of flow velocity, there is a specific slurry concentration that corresponds to a peak i_{prot} or a peak corrosion rate. This result may be useful in scenarios where corrosion is the dominant mechanism in erosion-corrosion, and the slurry concentration can be varied.

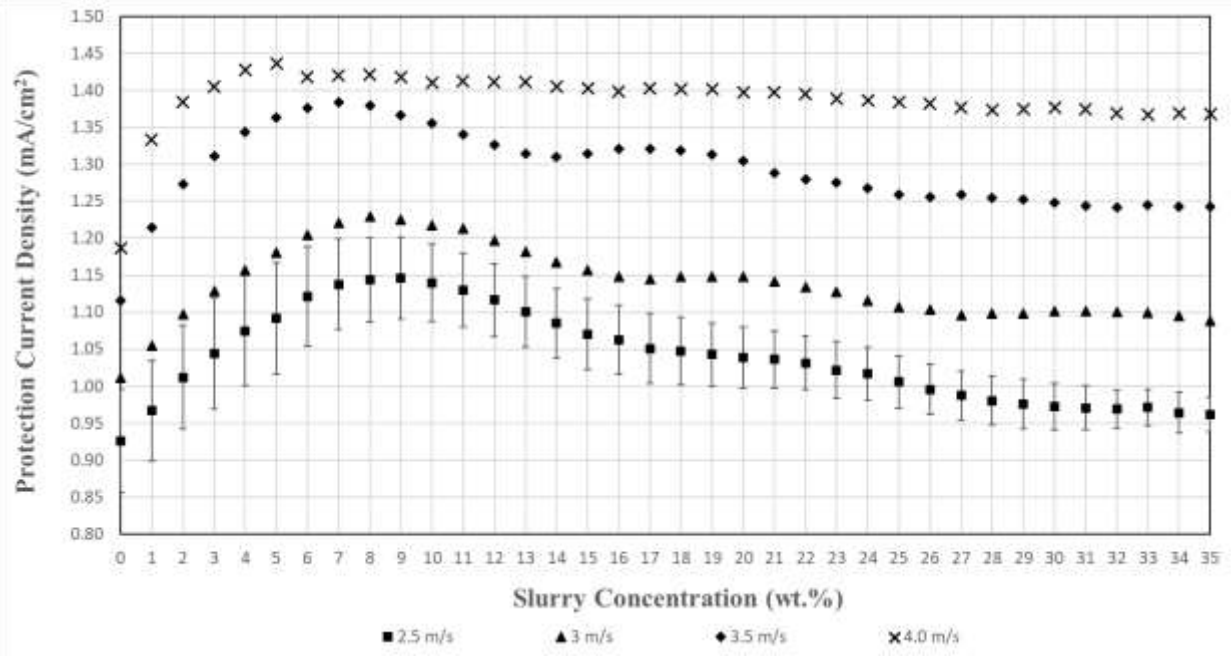

Figure 4.8. i_{prot} as a function of slurry concentration at flow velocities of 2.5, 3.0, 3.5, and 4.0 m/s as measured from cathodically protecting an AISI 1018 carbon steel elbow in saturated potash brine using 1.05 mm diameter silica sand.

Each flow velocity trendline shown in Figure 4.8 follows a similar shape with the addition of a shift in i_{prot} as flow velocity increased. The similar trendline shapes implied flow velocity could have a linear relationship to i_{prot}. The relationship between flow velocity and i_{prot} was plotted and is shown in Figure 4.9. The confidence interval of the data is shown for the 0 wt.% trendline for reference. From the figure, the slopes of the 10, 20, and 30 wt.% trendlines were all similar, while the slope of the 0 wt.% trendline showed an apparent deviation. The difference in slopes between the lines with slurry concentration and the line without may suggest an interaction occurs between erosion and corrosion in which the rate of change of current density was altered. The addition of slurry concentration increased the rate at which current density increases with the flow velocity. These results imply that a possible synergistic relationship was occurring between erosion and corrosion.

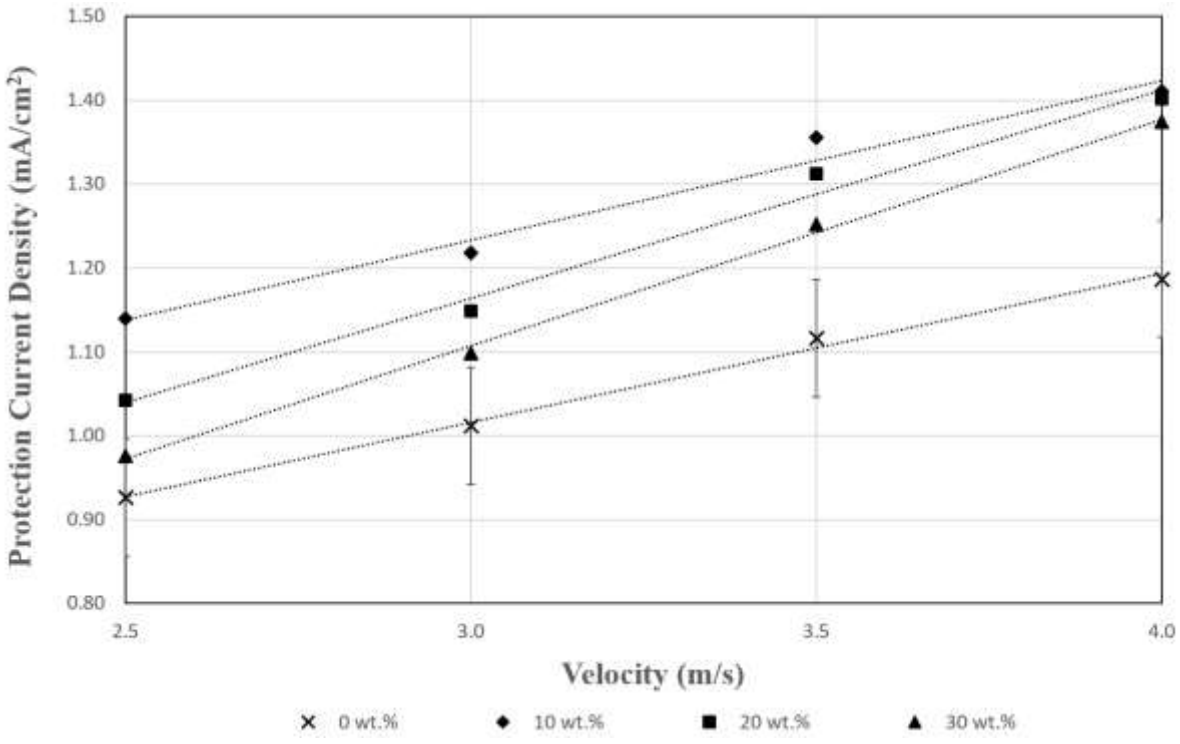

Figure 4.9. The effect of flow velocity on i_{prot} at 0, 10, 20, and 30 wt.% sand concentration using 1.05 mm diameter sand in saturated potash brine.

4.5.3 The Effect of Slurry Concentration and Flow Velocity using 0.55 mm Sand

This section describes the results of Phase III experiments using the 0.55 mm particle size. The experiments and procedures follow the methodology stated in Section 3.4.3. Cathodic protection was applied to the elbow during flow loop operation at flow velocities of 2.5, 3.0, 3.5, and 4.0 m/s while changing the slurry concentration from 0 to 35 wt.% in 1% steps. During cathodic protection, i_{prot} was recorded for each step change.

As stated in the methodology for Phase III, datum points were used to ensure that data sets collected on the flow loop were consistent with each other. The datum was the i_{prot} measured at a flow velocity of 2.5 m/s and a slurry concentration of 0 wt.%. Experimental results over nine trials determined the datum point to have an average current density of 0.926 ± 0.039 mA/cm^2. Prior to each experiment at higher flow velocities, a datum measurement was performed. Table 4.2 shows the averaged datum measurements recorded prior to experiments performed at 3.0, 3.5, and 4.0 m/s. From the table, all experiments performed at higher flow velocities had average datums that match the value of 0.926 mA/cm^2 within the confidence interval. The matching datums ensure the data recorded was repeatable and comparable to each other.

Table 4.2. List of datum point measurements found at 2.5 m/s and 0 wt.% slurry concentration to ensure the comparability of data within different data sets at higher flow velocities.

Trial Flow Velocity (m/s)	**Datum Measurement at 2.5 m/s and 0 wt.% (mA/cm^2)**	**95% Confidence Interval (±mA/cm^2)**
2.5	0.926	0.039
3.0	0.924	0.039
3.5	0.929	0.039
4.0	0.888	0.039

The main experimental results using the 0.55 mm sand were plotted as i_{prot} as a function of slurry concentration and shown in Figure 4.10. Figure 4.10 shows similar trends as observed for the 1.05 mm particle size. At each flow velocity, i_{prot} increased to a maximum, after which the further addition of sand acted to decrease the current load. The maximum i_{prot} occurred at slurry concentrations of 10, 11, 6, and 5 wt.% for flow velocities of 2.5, 3.0, 3.5, and 4.0 m/s.

Following the larger particle size results, the trendlines in Figure 4.10 appear to have relatively equal step changes as the flow velocity increases. This finding further supports the previous conclusion of a linear relationship between flow velocity and i_{prot}. Many of the general relationships and findings occurred in both the 0.55 mm and 1.05 mm particle size, and the results follow the analysis of the 1.05 mm particle size with the exception of larger i_{prot} values.

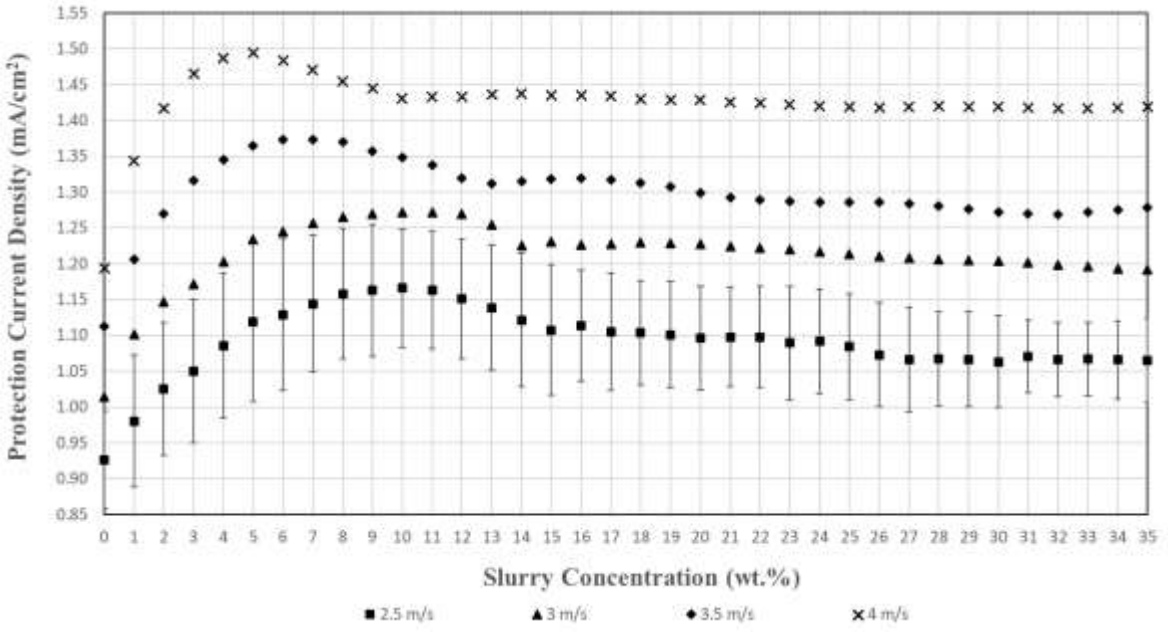

Figure 4.10. i_{prot} as a function of slurry concentration at flow velocities of 2.5, 3.0, 3.5, and 4.0 m/s as measured from cathodically protecting an AISI 1018 carbon steel elbow in saturated potash brine using 0.55 mm diameter silica sand.

4.5.4 The Effect of Particle Size on i_{prot}

From the results of the two different particle sizes, the particles were compared to show the effect of sand size on i_{prot}. Individual plots were constructed that displayed the data of both particles at a single flow velocity.

Figure 4.11 shows the comparison of both particles at a flow velocity of 2.5 m/s. From the figure, it is evident that many differences exist between the two sand sizes. At slurry concentrations below 5 wt.%, both particles behaved similarly to each other. As the slurry

concentration increased beyond 5 wt.%, different behaviour of the particles was observed, and their trendlines separated. The first distinct difference between the particles was the slurry concentration where the maximum i_{prot} occurred and the value of the maximum i_{prot}. The figure shows that the smaller particle's i_{prot} peaked at 10 wt.% slurry concentration while the larger particle's i_{prot} peaked at approximately 9 wt.%. This finding may suggest that smaller particles increase the range of slurry concentrations that affect the corrosion occurring and corresponding i_{prot}. The maximum i_{prot} produced by the two particles was also different. The smaller particle reached a slightly larger value of i_{prot}. The larger value of i_{prot} may indicate that the smaller particle size would produce larger amounts of corrosion. The most distinct difference between the two particles was observed at high slurry concentrations. The smaller particle required significantly more current density to protect the metal at high slurry concentrations. The large separation of the two trendlines at high slurry concentrations leads to the conclusion that smaller particles may induce more severe corrosion than larger particles. The difference in the corrosion produced by various particle sizes may be most evident at high slurry concentrations.

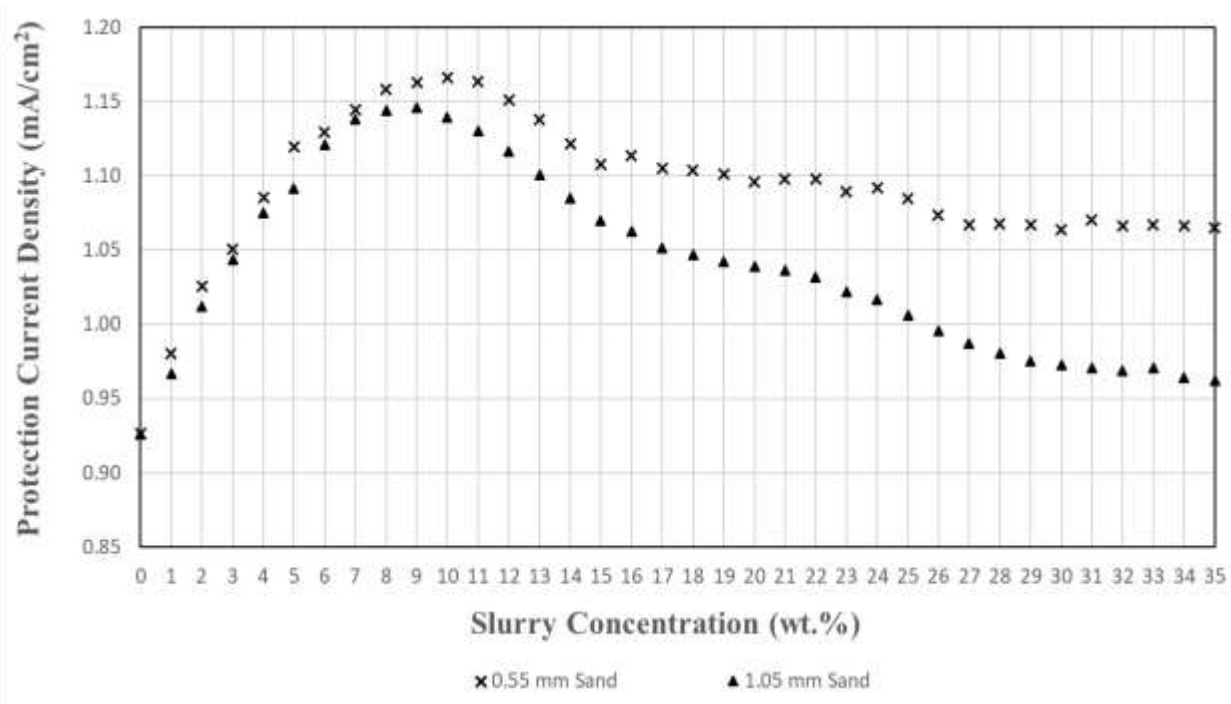

Figure 4.11. Comparison of 1.05 mm and 0.55 mm sand particles at a flow velocity of 2.5 m/s on the i_{prot} required to inhibit corrosion of an AISI 1018 carbon steel elbow in saturated potash brine.

Figure 4.12 shows the comparison of both particles at a flow velocity of 3.0 m/s. The small step change in flow velocity from 2.5 to 3.0 m/s mainly enhanced the trends previously discussed in Figure 4.11. Between 0 - 4 wt.% slurry concentration, both particles behaved similarly. Beyond 4 wt.% slurry concentration, the varying trends of each particle became evident. Again, both particles exhibited a local maximum i_{prot}. From the figure, the smaller particle required a higher slurry concentration to reach the maximum i_{prot}. The smaller particle's i_{prot} peaked at 10 wt.% slurry concentration while the larger particle peaked at 7 wt.%. Compared to the particle size results at a flow velocity of 2.5 m/s, this is a more significant difference between the slurry concentrations where the maximum i_{prot} was observed. This finding may suggest higher flow velocities could enhance the effect of particle size on i_{prot}. Figure 4.12 also shows a considerable difference in the value of the maximum i_{prot} produced by each particle. The smaller particle had a maximum i_{prot} of 1.31 mA/cm^2 while the larger particle achieved a maximum of 1.23 mA/cm^2. The difference in maximum i_{prot} values may conclude that smaller particles create a more corrosive environment. In addition, as previously shown in Figure 4.11 and now again in Figure 4.12, the smaller particle also required a larger i_{prot} at higher slurry concentrations. Increasing the flow velocity from 2.5 to 3.0 m/s caused the i_{prot} separation between the particle trendlines to become larger at higher slurry concentrations. These results suggest there may be a complicated relationship between flow velocity and particle size on the corrosion rate occurring in the elbow, and the amount of current density required to inhibit corrosion.

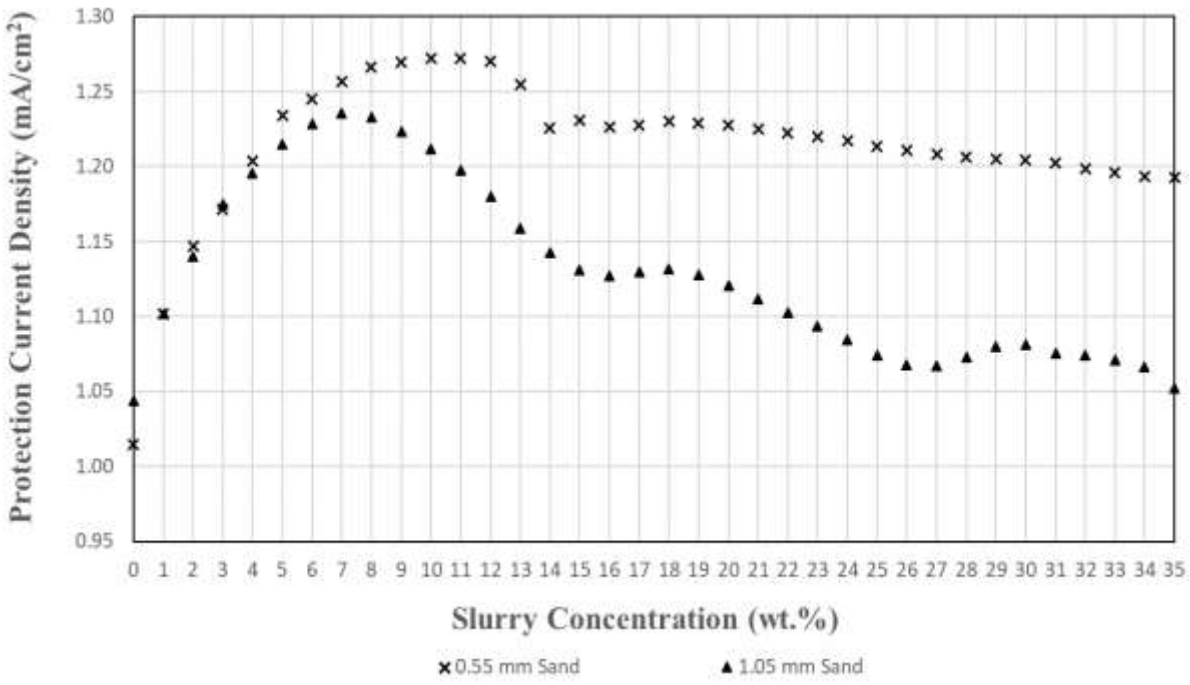

Figure 4.12. Comparison of 1.05 mm and 0.55 mm sand particles at a flow velocity of 3.0 m/s on the i_{prot} required to inhibit corrosion of an AISI 1018 carbon steel elbow in saturated potash brine.

Figure 4.13 shows the comparison of sand size at a flow velocity of 3.5 m/s. The results at 3.5 m/s show a reversal in trends found at flow velocities of 2.5 and 3.0 m/s. Figure 4.13 shows the two particle sizes appear to act in unison, showing little difference in corrosive activity. A small deviation occurred at slurry concentrations past 23 wt.% solids, in which the smaller particle required slightly more current density for protection. The smaller particle requiring larger i_{prot}'s at high slurry concentrations is consistent with previous results shown for flow velocities of 2.5 and 3.0 m/s. The previous trends, which displayed varying maximum i_{prot}'s between the particle sizes, was not continued at a flow velocity of 3.5 m/s. This could suggest at higher flow velocities (past 3.0 m/s), the effect of particle size on the corrosion rate may be negligible.

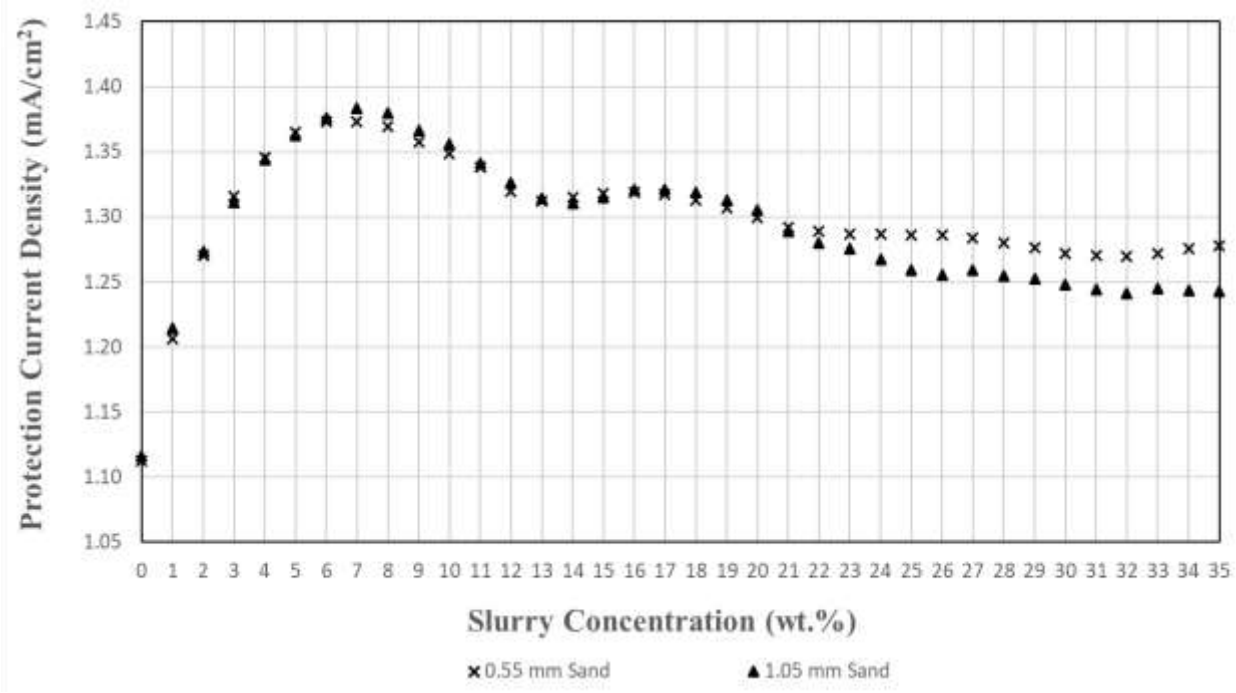

Figure 4.13. Comparison of 1.05 mm and 0.55 mm sand particles at a flow velocity of 3.5 m/s on the i_{prot} required to inhibit corrosion of an AISI 1018 carbon steel elbow in saturated potash brine.

Figure 4.14 shows the comparison of sand size at a flow velocity of 4.0 m/s. The results at a flow velocity of 4.0 m/s are similar to those shown at 3.5 m/s. While there was noticeably more separation observed between the particle size trendlines at a flow velocity of 4.0 m/s compared to at 3.5 m/s, from the confidence interval of the experiment (as shown in Figure 4.8 and 4.10), the trends were very similar. At a flow velocity of 4.0 m/s, the maximum i_{prot} for both the 0.55 and 1.05 mm particles occurred at a slurry concentration of 5 wt.%, with the magnitude of the smaller particles i_{prot} being marginally larger. While the particle trendlines shown in Figure 4.14 are incredibly similar in shape and value, the smaller particle overall exhibited a slightly larger i_{prot} required at most slurry concentrations. The smaller particle requiring larger i_{prot} to provide protection again indicates that smaller particles may produce more corrosive environments. The results at the flow velocity of 4.0 m/s also reinforce the suggestion that higher flow velocities may reduce the effect particle size has on the observed corrosion rate and corresponding i_{prot}.

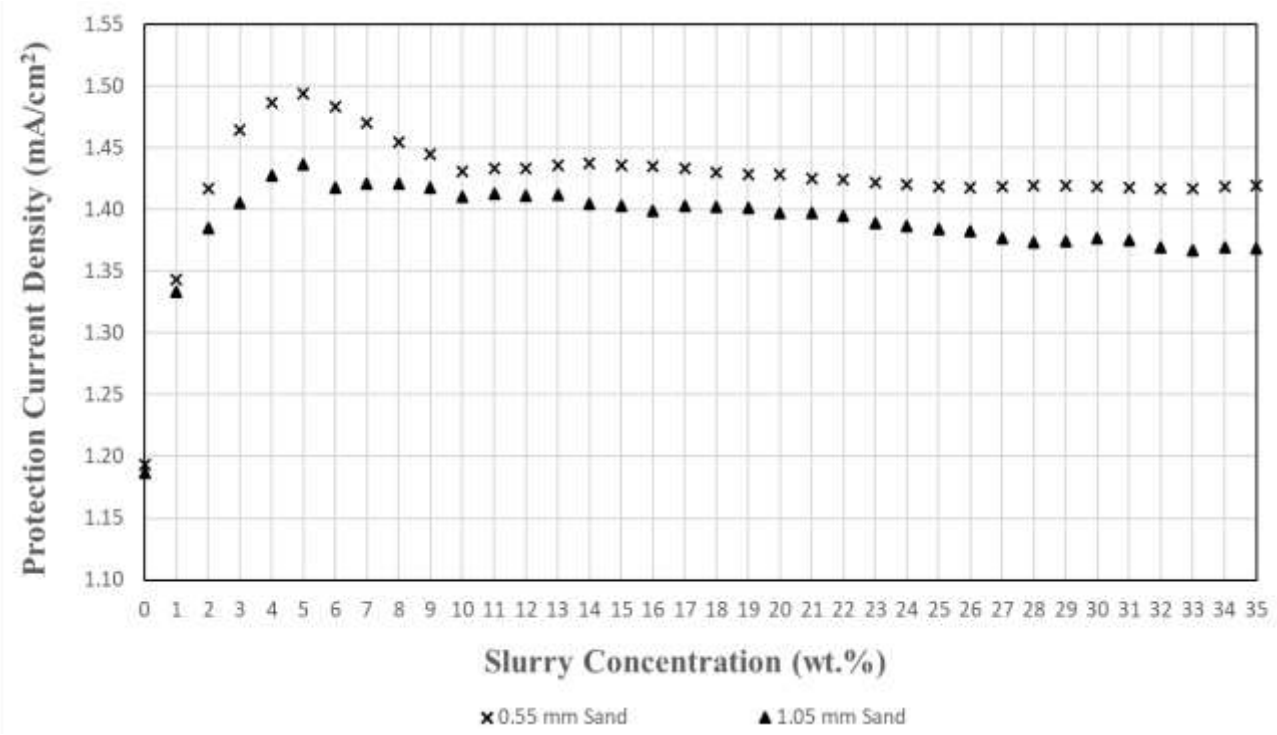

Figure 4.14. Comparison of 1.05 mm and 0.55 mm sand particles at a flow velocity of 4.0 m/s on the i_{prot} required to inhibit corrosion of an AISI 1018 carbon steel elbow in saturated potash brine.

4.5.5 Discussion of Phase III Results

Phase III results showed, regardless of particle size, that each flow velocity produced trends in which i_{prot} increased with slurry concentration, peaked, and then decreased with the further addition of sand. Protection current density in this research was assumed to be related to the corrosion rate occurring on the metal surface. As the corrosion rate increases, the i_{prot} required to inhibit corrosion would also increase. Therefore, when i_{prot} increased or decreased, this research inferred that the theoretical corrosion rate was also increasing or decreasing. Further discussion of the relationship between i_{prot} and the corrosion rate is provided in Section 4.6.

In each experiment, i_{prot} increased with slurry concentration until the maximum i_{prot} was produced. One possible reason slurry concentration caused the increase in i_{prot} may be from the sand particles increasing the local mass transfer of oxygen to the metal surface. Higher mass transfer rates of oxygen occur from particles increasing fluid mixing and turbulence (Guo H. ,

2006). Oxygen is a primary reactant of the corrosion reaction. The mass transfer of oxygen is well-known to be a rate-determining step in the corrosion reaction. Therefore, as the slurry concentration rises, the mass transfer rate of oxygen, and thus i_{prot}, may also increase. Erosion of the metal will also increase with the increase of slurry concentration. Erosion occurring on the metal surface could act to increase the stored strain in the metal from particle impingement. Research has shown that increased stored strain creates more active anodic sites and higher corrosion rates (Xie *et al.*, 2003). Work hardened metal forming from particle impingements on the metal surface has also been shown to increase the corrosion experienced on steels (Wang and Stack, 2000). This effect occurs from corrosion preferentially attacking harder metals. The above mechanism(s) could in part, or in whole, cause the increase in i_{prot} observed in the results.

After the maximum i_{prot} point at all flow velocities tested, i_{prot} was shown to decrease with the further addition of slurry concentration. The reduction in i_{prot} may be evidence of a complex interaction of mechanisms that forced corrosion to decrease. Beyond the maximum i_{prot} at each flow velocity, it is possible that further addition of sand no longer increased the turbulence or mixing of the fluid that elevates the mass transfer of oxygen. The results suggest the particles may be interacting with each other to decrease the turbulence they provide in the bulk fluid. Therefore, the more particles there are, the less turbulence would be achieved. One such particle interaction could be the increase in viscosity of the slurry created at higher sand concentrations. Research has shown at higher slurry concentrations, the mass transfer of dissolved gases in solution decreases from increasing slurry viscosity (Li *et al.*, 1996). Larger slurry viscosities may then cause lower mass transfer rates of oxygen and a smaller i_{prot}. In addition, the further increase of sand concentration may create a mass transfer barrier on the surface of the metal. As the test sample in these experiments was an elbow, centrifugal forces could push the concentration of particles to be greatest along the outer surface of the bend. At higher slurry concentrations, the sand could blanket the metal surface in a dense layer of particles, limiting the transfer of corrosion reactants to the metal. The layer could, in theory, also limit the diffusion of corrosion products from the surface to the bulk solution. The limiting of corrosion reactants and products to and from the metal surface could cause the observed decrease in corrosion and i_{prot} at higher slurry concentrations.

For each flow velocity tested, the maximum i_{prot} occurred at different slurry concentrations. The 1.05 mm particle experiments displayed maximum i_{prot} values at 9, 8, 7, and 5 wt.% slurry concentration for flow velocities of 2.5, 3.0, 3.5, and 4.0 m/s. Similarly, the 0.55 mm particle displayed maximum i_{prot} values at 10, 11, 6, and 5 wt.% slurry concentration. One possible explanation for the decreasing trend is that each maximum i_{prot} slurry concentration represents the conditions in which the mass transfer rate of oxygen is at a maximum with respect to the corrosion reaction. This theory implies that at each maximum i_{prot} slurry concentration, the mass transfer of oxygen to the anode would no longer be the rate-determining step in the corrosion reaction. Instead, the rate-determining step would be the consumption rate of oxygen in the corrosion reaction. The corrosion reaction cannot go quicker than the rate it can consume oxygen. Therefore, the corrosion reaction inside the flow loop could have a mass transfer *ceiling* for oxygen. When the maximum mass transfer rate of oxygen is achieved, increasing it further would not affect the corrosion rate. This explanation assumes that at each flow velocity, i_{prot} would increase with slurry concentration until the *ceiling* was reached. At higher flow velocities (which increases the mass transfer of oxygen), the ceiling would occur at lower slurry concentrations.

Further results showed that the flow velocity was linearly related to i_{prot}. Flow velocities' main contribution to changing the corrosion rate, and thus i_{prot}, was likely by increasing or decreasing the mass transfer of oxygen to the metal surface. Faster flow velocities provide larger oxygen mass transfer rates, which accelerate the corrosion reaction. Chemically speaking, the mass transfer rate of any species is proportional to each species individual velocity. As flow velocity increases, the convection and velocity of individual diffusive species increase proportionally (Bird *et al.*, 2007). Therefore, the mass transfer of any species is proportional to the bulk fluid velocity. In addition, corrosion rates under cathodic control are proportional to the mass transfer rate of oxygen as the kinetics of the corrosion reaction can only proceed as fast as the supply of oxygen (Yabuki A. , 2011). Therefore, combining the linear relationships that the mass transfer of oxygen is proportional to flow velocity and the corrosion rate is proportional to the mass transfer of oxygen, it could be concluded the correlation between flow velocity and the corrosion rate is also linear.

In Figure 4.9, the plot of i_{prot} versus flow velocity for the 1.05 mm particle showed a unique response to the addition of slurry concentration. The slopes of each trendline depicting 10, 20 and 30 wt.% slurry concentration were similar and shallow. The slope of the 0 wt.% slurry concentration trendline, however, was steeper. This result may indicate that the addition of solid particles decreased the rate at which i_{prot} changed due to flow velocity. The differing slopes of slurry concentration trendlines suggest that while adding slurry concentration may increase the overall mass transfer of oxygen and corresponding i_{prot}, it may weaken the influence fluid velocity has on the mass transfer rate of oxygen. The mechanism in which slurry concentration increases the mass transfer of oxygen (mixing, turbulence) could hinder how fluid velocity increases the mass transfer of oxygen. A possible explanation of how the mechanisms interact may be related to the mass transport boundary-layer thickness near the pipe wall. During high(er) slurry concentrations, the boundary-layer thickness near the pipe wall may be increased from the larger slurry viscosity. A thicker boundary layer would increase the distance and path oxygen diffuses through to reach the metal surface (Bird *et al*., 2007). The change in boundary layer thickness may also change the velocity profile within the boundary layer. The combination of a larger boundary layer thickness and different velocity profiles within the layer may explain the reduction in fluid velocities effect on the mass transfer of oxygen in the presence of slurry concentration.

Both the 1.05 and 0.55 mm particle size results were compared in Figures 4.11 and 4.12 to show the effect of particle size on i_{prot} at flow velocities of 2.5 and 3.0 m/s. The figures showed that the 0.55 mm particle required larger i_{prot}'s overall and shifted the maximum i_{prot} to occur at higher slurry concentrations. The magnitude of the maximum i_{prot} also increased using the 0.55 mm particle. These results suggest smaller particles may create a more corrosive environment within the elbow, therefore increasing the i_{prot} required. The two parameters in erosion-corrosion that change by altering the particle size are the number of impingements and impact energy of each impingement. Both parameters can affect the corrosion activity occurring on the metal surface.

As the size of the particles increase, the number of impingements will decrease. Impingements will produce enhanced corrosion through synergistic mechanisms such as the strain effect and work hardening (discussed in Section 2.5.2). The strain effect is a mechanism where impingements on a metal surface produce large amounts of internal strain, which increases the

number of dislocations inside the metal (Xie *et al.*, 2003). Dislocations act as active anodic sites for corrosion to occur. Work hardened steel from particle impingements may also be preferentially attacked by corrosion due to more dislocations in the metal (Wang and Stack, 2000). Therefore, more impingements may result in increased corrosion activity. Conversely, the impact energy of impingements will increase with particle size. Larger particles produce higher energies upon impact, causing increased wear damage. Therefore, impact energy may have a stronger relationship with erosion wear compared to corrosion. In studies where the effect of particle size on erosion was observed, larger particles generally exhibited more wear (Song and Du, 2017). In terms of this research, the effect of particle size on corrosion, and the corresponding i_{prot}, may be more dependent on the number of impingements on the metal surface. Smaller particles, which exhibit more impacts per unit time, required a larger i_{prot} at flow velocities of 2.5 and 3.0 m/s.

Both the 1.05 and 0.55 mm particle size results were compared in Figures 4.13 and 4.14 to show the effect of particle size on i_{prot} at flow velocities of 3.5 and 4.0 m/s. From the figures, the trends previously observed at lower flow velocities stopped. At higher flow velocities, the particle sizes began to exhibit similar behaviour, in some cases being indistinguishable from each other. This result suggested at sufficiently high flow velocities, the difference between the 0.55 and 1.05 mm particles on the corrosion of the elbow was negligible. At lower flow velocities, the 0.55 mm particle was shown to require larger i_{prot}'s, possibly caused by the increase in particle impingements compared to the larger particle. Similar to decreasing particle size, higher flow velocities will also increase the number of impingements. The results of this research found at higher flow velocities indicate the possibility of an interaction between the number of impingements and the impact energy of each impingement on the corrosion activity. The interaction may explain why both particle sizes display similar trends at 3.5 and 4.0 m/s. Larger particles at higher flow velocities would impact the surface at faster rates and produce more strain from their larger size, producing similar corrosion results to the smaller particles.

4.6 Phase IV - Correlation of Cathodic Protection Current Density to Corrosion Rate

4.6.1 Overview

The purpose of Phase IV experiments was to correlate i_{prot} to corrosion rates. Phase IV consisted of experiments using an analytical method to determine the in-situ corrosion rate in the metal elbow during slurry flow. The experimental method utilized was performed using the procedures previously discussed in Section 3.4.4. The following sections will discuss how the operating conditions for Phase IV experiments were chosen, the results of E_{corr} and i_{corr} experiments, the corresponding corrosion rates determined, and the correlation developed between i_{prot} and the corrosion rate. All results from Phase IV experiments, raw and calculated data, can be found in Appendix D.

4.6.2 Determining Phase IV Experimental Conditions

The main objective in determining the slurry concentration and flow velocity pairs used for experimentation was to encompass the entire range of i_{prot} measured in Phase III experiments. Figure 4.15 shows a graphical representation of Phase III results and how the operating conditions for Phase IV experiments were chosen. From the figure, five sets of operating conditions (both a flow velocity and slurry concentration) were selected, which encompassed the entire i_{prot} range. The five conditions included 2.5, 3.0, 3.5 and 4.0 m/s at 0 wt.% slurry concentration, and 4.0 m/s at 5 wt.% slurry concentration.

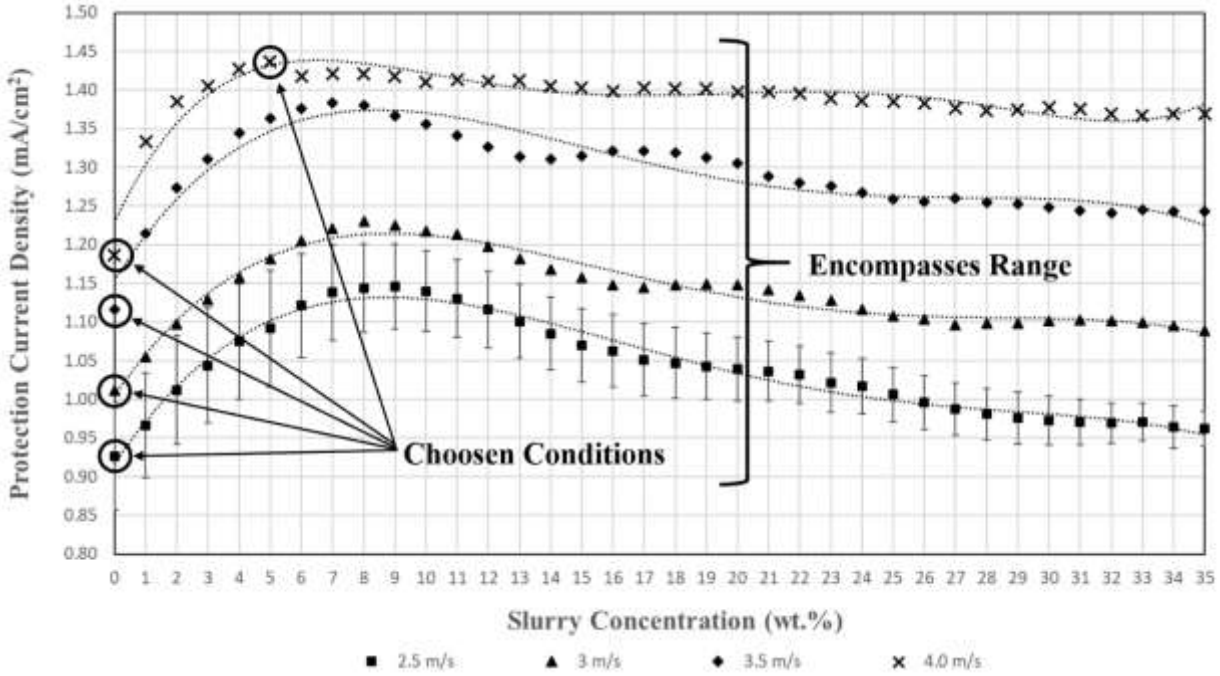

Figure 4.15. Operating conditions selected to determine the correlation between i_{prot} and the corrosion rate for the 1.05 mm sand.

6.6.3 Determining E_{corr} Experiments

E_{corr} was measured by operating the flow loop at one of the five chosen conditions and measuring the open-circuit potential of the elbow for 5-6 hours. At each of the five conditions, E_{corr} was measured a minimum of three times and averaged. A typical plot of the data measured during the experiment is shown in Figure 4.16. From the figure, E_{corr} was determined by drawing a sloped line that followed the trendline once the corrosion potential had stabilized. The point at which the plot deviates from the drawn line indicates the potential where E_{corr} becomes stable. In this research, E_{corr} generally occurred at 7500 seconds or just over two hours.

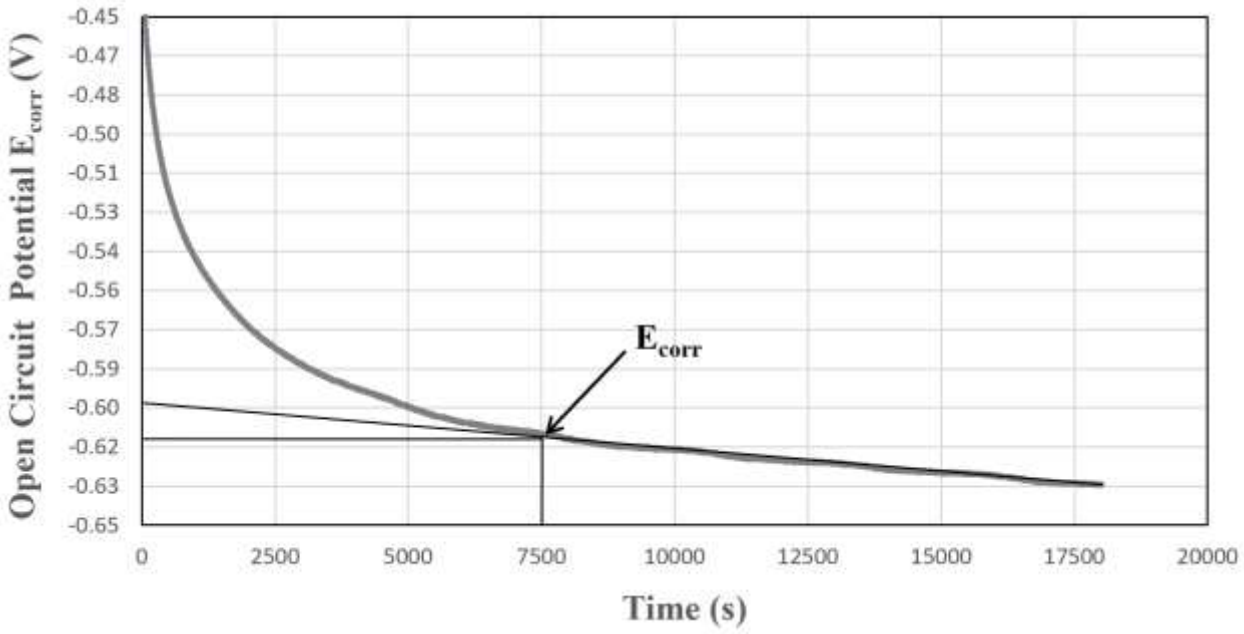

Figure 4.16. E_{corr} plot of an AISI 1018 carbon steel elbow at 3.5 m/s at 0 wt.% slurry concentration in saturated potash brine for the 1.05 mm particle size.

Results from the analysis of all E_{corr} plots measured at each operating condition were averaged and are displayed in Table 4.3. From the table, E_{corr} was shown to increase with increasing flow velocity and slurry concentration. The positive shift in E_{corr} could be an indication of increased anodic activity. Each positive shift in E_{corr} appeared to be similar in size following an increase in flow velocity. Figure 4.17 shows a plot of the tabulated E_{corr} data at a slurry concentration of 0 wt.%. From the figure, the correlation between flow velocity and E_{corr} at a constant slurry concentration was linear. This relationship may be useful in situations where E_{corr} is challenging to measure, but the flow velocity and slurry concentration of the environment are known.

Table 4.3. Average E_{corr} of an AISI 1018 carbon steel elbow in a potash-sand slurry using a 1.05 mm particle size.

Condition	Operating Variables		Average E_{corr} (V)	95% Confidence Interval (V)
	Slurry Velocity (m/s)	Slurry Conc. (wt.%)		
1	2.5	0	-0.620	0.020
2	3.0	0	-0.610	0.024
3	3.5	0	-0.596	0.020
4	4.0	0	-0.584	0.008
5	4.0	5	-0.566	0.018

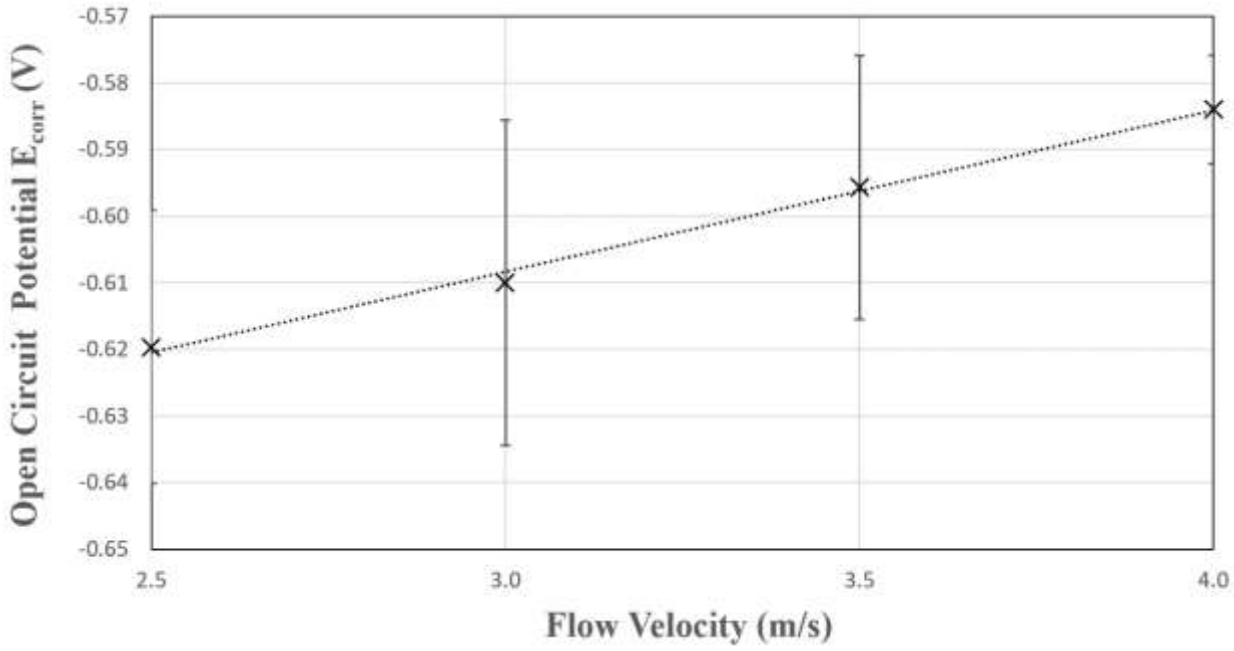

Figure 4.17.Plot of E_{corr} as a function flow velocity at 0 wt.% slurry concentration for an AISI 1018 carbon steel elbow in saturated potash brine using a 1.05 mm particle.

4.6.4 Determination of i_{corr} and Corresponding Corrosion Rates

The i_{corr} was determined by running the deoxygenated flow loop at the selected operating conditions while holding the elbow at E_{corr}. These experiments were performed using the procedures as detailed in Section 3.4.4. Each experiment measuring i_{corr} was repeated a minimum of five times, with the resulting values averaged.

The average i_{corr} measured at each test condition is displayed in Table 4.4. Similar to the E_{corr} results in Section 4.6.3, there appeared to be a relationship between i_{corr} and the flow velocity. With each increase in flow velocity at a constant slurry concentration, the corresponding i_{corr} increased in equal steps. This observation may imply that increasing flow velocity increases the rate of corrosion. An additional increase in i_{corr} was observed from the addition of 5 wt.% slurry concentration (measured at a flow velocity of 4 m/s). This result could suggest that slurry concentration may also increase the rate of corrosion.

Table 4.4. Average i_{corr} values of an AISI carbon steel elbow in saturated potash-sand slurry using a 1.05 mm particle size.

Condition	**Operating Variables**		**Average i_{corr} (mA/cm^2)**	**95% Confidence Interval (mA/cm^2)**
	Flow Velocity (m/s)	**Slurry Concentration (wt.%)**		
1	2.5	0	0.200	0.026
2	3.0	0	0.240	0.023
3	3.5	0	0.296	0.023
4	4.0	0	0.341	0.023
5	4.0	5	0.405	0.084

To further investigate the effect of flow velocity on i_{corr}, a plot shown in Figure 4.18 was developed using the results at 0 wt.% slurry concentration. The figure shows a clear linear relationship between corrosion current density (i_{corr}) and the flow velocity. Figure 4.18 implies that the corrosion rate, which is determined by i_{corr}, is perhaps linearly proportional to flow velocity.

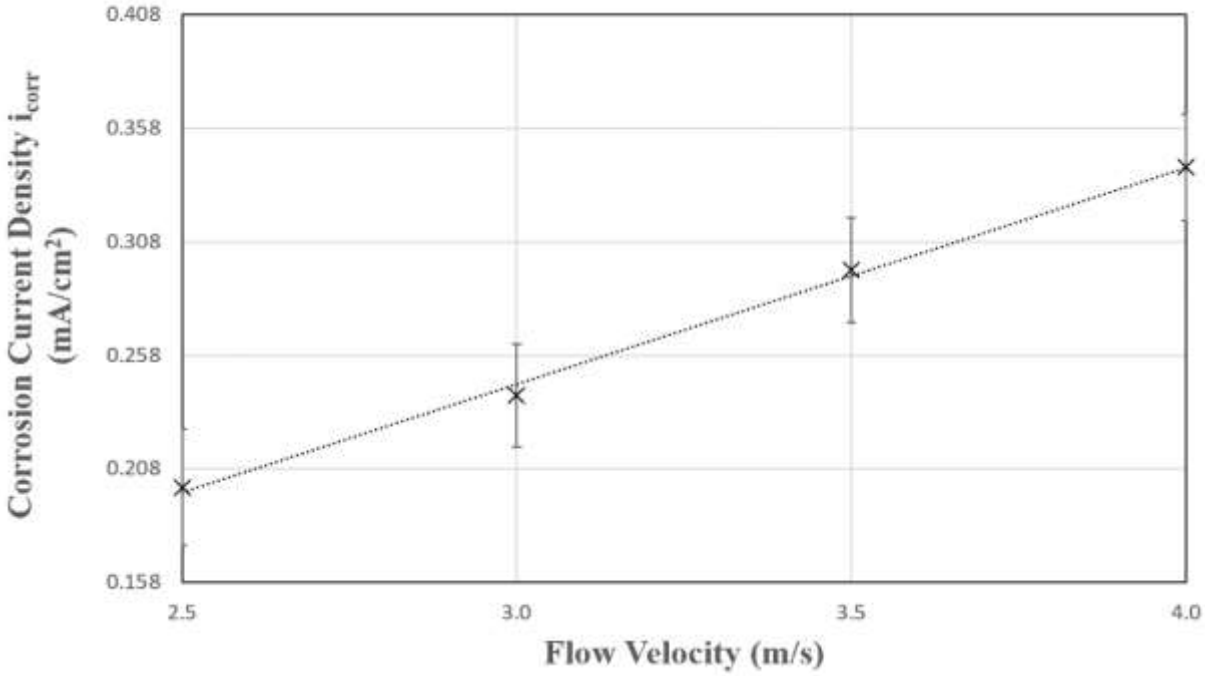

Figure 4.18. Plot of i_{corr} as a function flow velocity at 0 wt.% slurry concentration for an AISI 1018 carbon steel elbow in saturated potash-sand slurry for using a 1.05 mm particle size.

Corrosion rates were determined from Table 4.5 using the measured i_{corr} and placing them into Eq. [2.5] shown in Section 2.2.2. A sample of the calculation can be found in Appendix F. The corrosion rates at each tested condition are displayed in Table 4.5. The corrosion rate results follow the same trends as found for i_{corr}. As the flow velocity increases, the corrosion rate increased proportionally. The addition of 5 wt.% slurry concentration at 4.0 m/s also showed a corresponding increase in the corrosion rate.

Table 4.5. Average corrosion rates of an AISI 1018 carbon steel elbow in a saturated potash-sand slurry using a 1.05 mm particle size.

Condition	Operating Variables		Average Corrosion Rate (g/m^2hr)	95% Confidence Interval (g/m^2hr)
	Slurry Velocity (m/s)	Slurry Concentration (wt.%)		
1	2.5	0	2.09	0.27
2	3.0	0	2.51	0.24
3	3.5	0	3.09	0.24
4	4.0	0	3.56	0.24
5	4.0	5	4.66	0.56

4.6.5 Correlating i_{prot} to the Corrosion Rate

Phase IV corrosion rates were combined with Phase III i_{prot} values to produce a correlation displaying the relationship between the i_{prot} and the corrosion rate it inhibits. The correlation used the i_{prot} values measured at the five conditions discussed in Section 4.6.2 and plotted them against corrosion rates measured at the same parameters.

Figure 4.19 shows the correlation between the i_{prot} and corrosion rates. Observing the figure, the relationship between i_{prot} and the corrosion rate was a linear line with a slope of 5.09. The average error of the correlation was ± 0.84 g/m^{2}hr. The linear correlation suggests corrosion rates could be predicted based on the amount of cathodic protection current required to protect the steel. The linear relationship also suggests that i_{prot} may be proportional to the corrosion rate regardless of the flow velocity or slurry concentration tested in this research. Therefore, it may be possible to predict the corrosion rate at any given operating condition (flow velocity and slurry concentration) if the i_{prot} is known. Observing the error bars in Figure 4.19 shows that the last data point had a significantly larger confidence interval than the first four. The first four data points were measured at 0 wt.% slurry concentration, while the 5th data point was measured at 5 wt.%. Therefore, the last point's larger confidence interval may result from how slurry concentration reduced the consistency of the experimental measurements. However, the average of the measurement still fits well with the linear approximation.

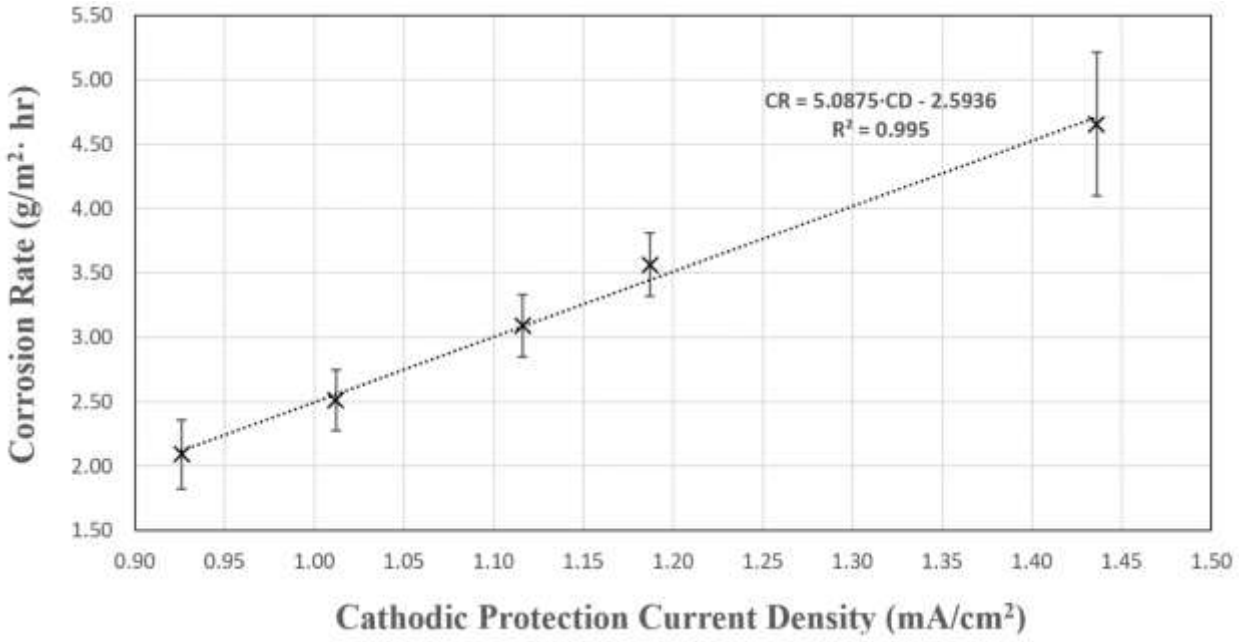

Figure 4.19. Correlation of corrosion rate to the amount of protective current density required to protect an AISI 1018 carbon steel elbow in saturated potash-sand slurry flow.

A verification point was measured to validate Figure 4.19 results and compare a theoretical and actual corrosion rate. The verification point was randomly selected to be the corrosion rate at a flow velocity of 2.5 m/s and 5 wt.% slurry concentration using the 1.05 mm sand particle. From Phase III data, the current density required to protect the elbow at those parameters was 1.09 mA/cm^2. Using Equation [4.1] found from Figure 4.19, where *CR* denotes the corrosion rate, and *CD* denotes the i_{prot}, the following theoretical corrosion rate occurring at a flow velocity of 2.5 m/s and 5 wt.% slurry concentration was made:

$$CR = 5.09 \cdot CD - 2.59 \pm 0.38 \frac{g}{m^2 hr} \quad [4.1]$$

$$CR = \left(5.09 \frac{\frac{g}{m^2 hr}}{\frac{mA}{cm^2}} \cdot 1.09 \frac{mA}{cm^2}\right) - 2.59 \frac{g}{m^2 hr} \quad [4.2]$$

$$CR = 2.96 \pm 0.38 \frac{g}{m^2 hr} \quad [4.3]$$

The correlation predicts the corrosion rate occurring at a flow velocity of 2.5 m/s and 5 wt.% slurry concentration to be 2.96 ± 0.38 g/m^{2}hr (see Equation [4.3]). This prediction was compared to the actual corrosion rate to check the accuracy of the correlation. The actual corrosion rate was measured using the methods discussed in Section 3.4.4. The data collected to determine the actual corrosion rate is shown in Table 4.6 (see Appendix D for the complete data set). As shown in the table, the actual corrosion rate was measured to be 3.43 ± 0.74 g/m^{2}hr.

Table 4.6. Actual corrosion rate measurement results found at 2.5 m/s and 5 wt.% slurry concentration for an AISI 1018 carbon steel elbow in saturated potash-sand slurry flow.

Operating Condition	E_{corr} **(V)**	i_{corr} **(mA/cm^2)**	**Corrosion Rate (g/m^{2}hr)**	**95% Confidence Interval (g/m^{2}hr)**
2.5 m/s and 5 wt.%	-0.596	0.302	3.43	0.74

The results from both the predicted and measured corrosion rates, when compared, showed that the correlation was able to predict the corrosion rate within experimental error. The actual corrosion rate of 3.43 ± 0.74 g/m^{2}hr was within the predictions range of 2.96 ± 0.38 g/m^{2}hr. A visual representation of the comparison is shown by plotting the actual and predicted corrosion rate points on the correlation in Figure 4.20. As shown in the figure, the actual corrosion rate measured overlaps the predicted point within error. This validation experiment was sufficient to verify this correlation's use to predict corrosion rates using i_{prot} (within the bounds of this research). The correlation was used to replot Phase III results of both sand sizes in terms of the corrosion rate, and are shown in Figure 4.21 and 4.22.

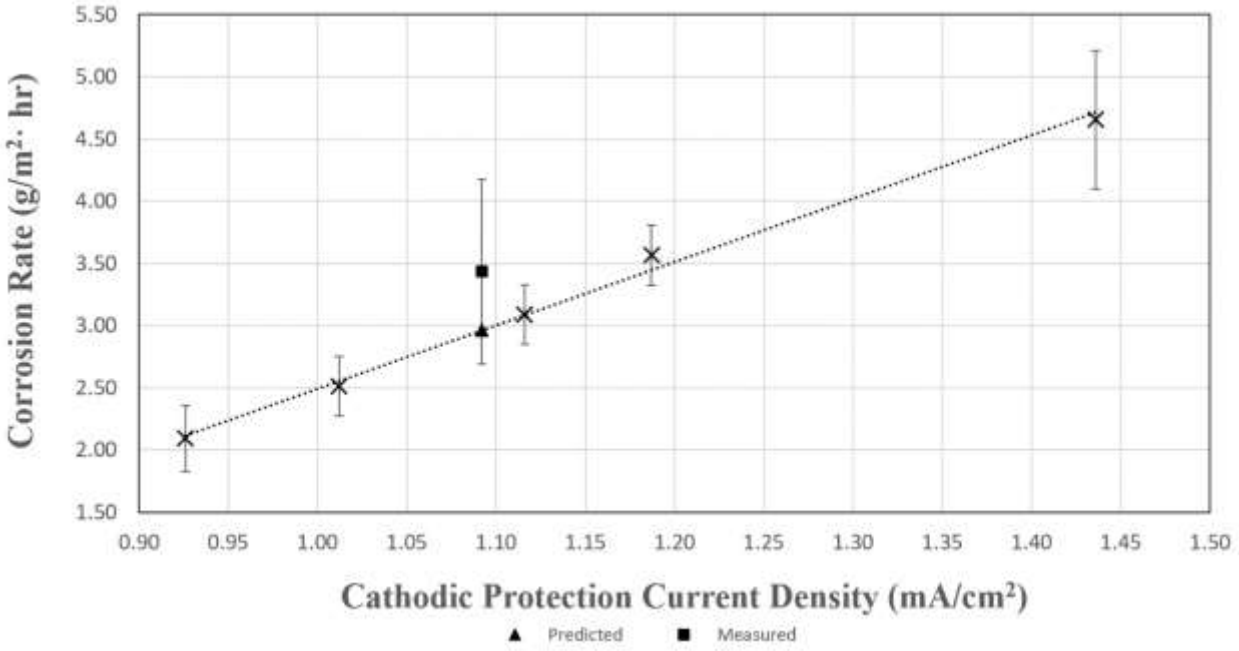

Figure 4.20. The predicted and actual corrosion rate measured at a flow velocity of 2.5 m/s and 5 wt.% slurry concentration for an AISI 1018 carbon steel elbow in a saturated potash-sand slurry using the 1.05 mm particle size.

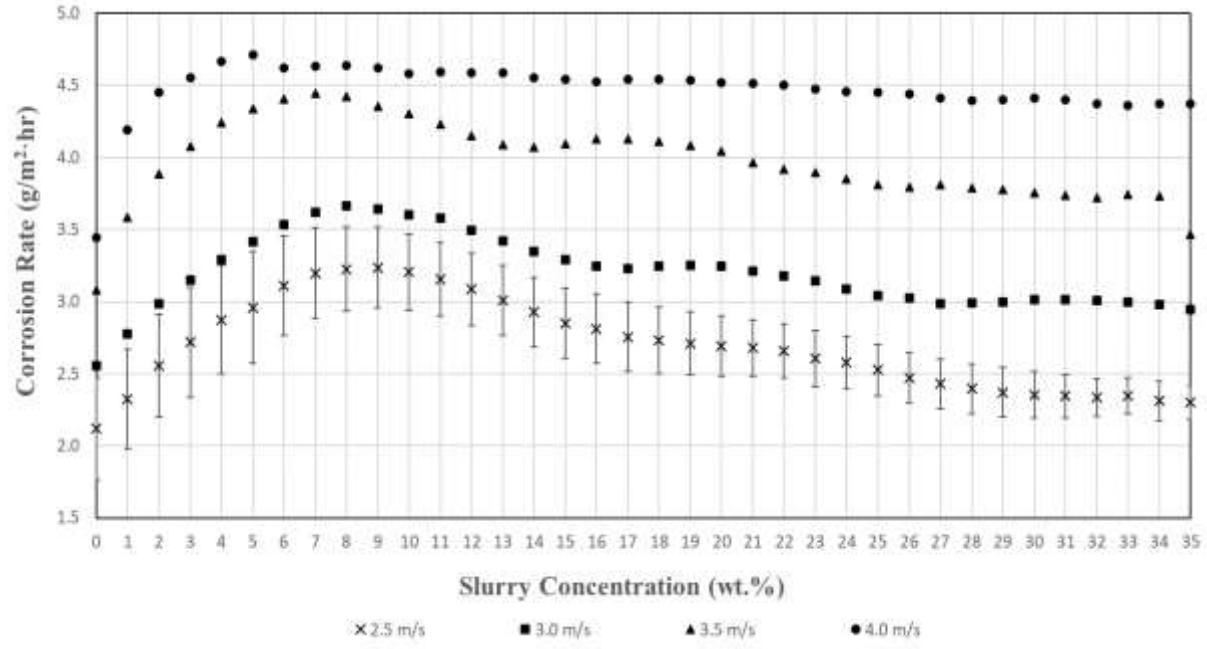

Figure 4.21. Plot of corrosion rate as a function of slurry concentration for an AISI 1018 carbon steel elbow in a saturated potash-sand slurry using the 1.05 mm particle size.

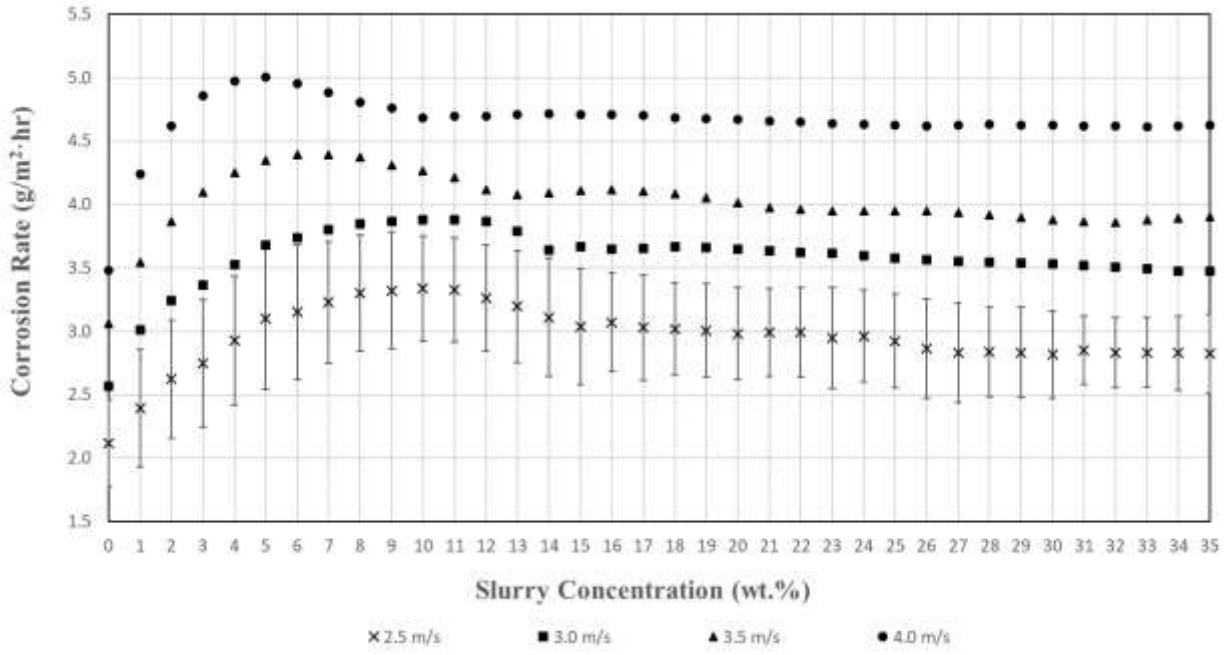

Figure 4.22. Plot of corrosion rate as a function of slurry concentration for an AISI 1018 carbon steel elbow in a saturated potash-sand slurry using the 0.55 mm particle size.

4.6.6 Discussion of Phase IV Results

Phase IV results discussed that E_{corr} linearly increased with increasing flow velocity. The E_{corr} of a metal is directly related to the corrosion rate occurring on the surface. The corrosion rate has been shown to be proportional to the mass transfer of oxygen (Yabuki A. , 2011). Therefore it could be suggested E_{corr} is linearly proportional to the mass transfer of oxygen in solution. Concurrently, the mass transfer of oxygen to the metal's surface has also been shown to be linearly proportional to the fluid's flow velocity (Bird *et al.*, 2007). Therefore, the above literature suggests that the connection between flow velocity and the E_{corr} is also linear. As the flow velocity of a system increases, the metal becomes more anodic, which results in a positive shift in E_{corr}. The above explanation also suggests how i_{corr} and the corrosion rate all increased linearly with flow velocity.

Figure 4.19 showed the correlation between i_{prot} and the corrosion rate. The figure showed that the corrosion rate increased linearly with i_{prot}. The correlation implied that the metal's corrosion rate might be predicted from providing cathodic protection and measuring the impressed current.

The correlation may prove there is an underlying mathematical explanation with further experimentation and modelling. The relationship between i_{prot} and corrosion rate opens many avenues for laboratory and industrial use cases. Using cathodic protection cells to measure the corrosion rate could be explored in environments where sensitive corrosion measurements are difficult or impossible, such as in furnaces, reactors, or pipelines. Cathodic protection cells could also be placed in bridges and reinforced concrete structures to provide rebar integrity data. Cathodic protection data is also electrical and can be measured and stored remotely, giving the ability to monitor corrosion from a distance. Cathodic protection is a well known, well-understood area of infrastructure integrity and is often already present in most pipelines, tanks, and bridges. The widespread adoption of cathodic protection, both by industry and legislation, provides a strong foundation for this methodology to be adopted. The knowledge that the current density supplied by cathodic protection could be used as a scale to measure corrosion may have more useful applications not explored in this thesis.

4.7 Determining Enhanced Corrosion

4.7.1 Overview

This section discusses the corrosion caused by synergistic factors between erosion and corrosion in Phase III and IV experiments. In erosion-corrosion, synergy is the interaction of erosion and corrosion that may lead to additional mass loss. From the data collected in Sections 4.5 and 4.6, the synergistic corrosion or enhanced corrosion was determined. The results aim to show how solids increase the corrosion rate by quantifying the synergistic interaction between erosion and corrosion. All data used to determine the enhanced corrosion can be found in Appendix C and D.

4.7.2 Determining Enhanced Corrosion

Enhanced corrosion was determined by subtracting the pure corrosion with no solids present in the flow loop from the total corrosion rate observed at any erosion-corrosion condition. In the experiments performed, the pure corrosion rate was assumed the corrosion observed at any flow

velocity with 0 wt.% slurry concentration. This definition of pure corrosion ensures the effect of flow velocity was considered and can also be referred to as *flow assisted corrosion*. While the flow assisted corrosion observed with zero slurry concentration was used as the pure corrosion in this study, this was an assumption. Carbon steel will experience erosion and corrosion from fluid flow, even with no solids present. However, the effect of fluid flow causing erosion in the absence of solids was assumed to be negligible compared to the corrosion experienced. The short length of experiments also aids the assumption that erosion is insignificant in mass loss during pure fluid flow. With the definition that the flow assisted corrosion is the pure corrosion rate at 0 wt.% slurry concentration, Figures 4.21 and 4.22 from Section 4.6 were analyzed to determine the synergistic corrosion experienced.

Figure 4.23 demonstrates how enhanced corrosion was determined at all slurry concentrations and flow velocities. This analysis was performed for each particle size to determine the enhanced corrosion experienced. From the figure, it is evident that erosion increased the rate of corrosion in the elbow. Over the slurry concentration range tested, there was no point where enhanced corrosion did not exist as a positive value. From the trend(s), it may be possible that beyond 35 wt.% slurry concentration, the enhanced corrosion could become zero or even negative. The analysis of Figure 4.23 was performed for all flow velocities and particle sizes, and all exhibited positive enhanced corrosion results at slurry concentrations greater than zero. Maximum enhanced corrosion of the 1.05 mm particle occurred at 9, 8, 7, and 5 wt.% solids for flow velocities of 2.5, 3.0, 3.5 and 4.0 m/s, respectively. Furthermore, the maximum enhanced corrosion of the 0.55 mm particle occurred at 10, 11, 6, and 5 wt.% solids for flow velocities of 2.5, 3.0, 3.5, and 4.0 m/s.

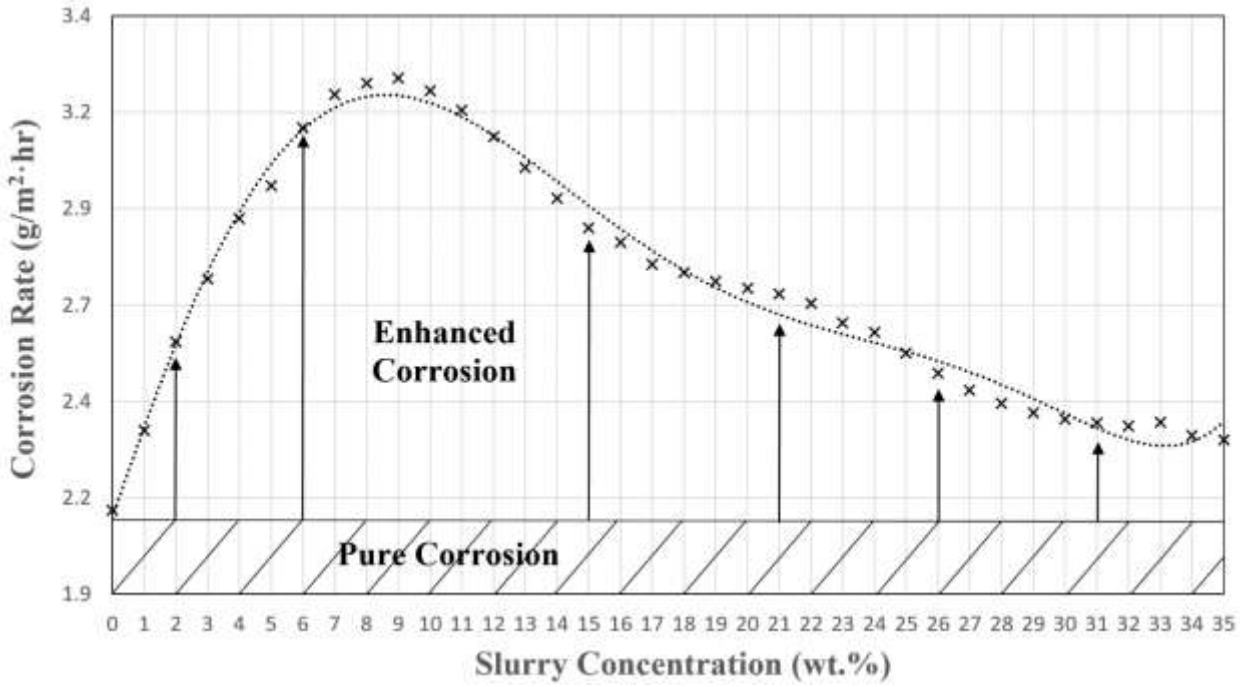

Figure 4.23. Analysis performed to determine the enhanced corrosion and pure corrosion of an AISI 1018 carbon steel elbow at 2.5 m/s in a saturated potash-sand slurry using the 1.05 mm particle size.

4.7.3 Effect of Slurry Concentration and Flow Velocity on Enhanced Corrosion - 1.05 mm Particles

The elbows' enhanced corrosion using the 1.05 mm particle size was examined at peak corrosion conditions (the slurry concentration and flow velocity at which i_{prot} was a maximum) to determine correlations. Enhanced corrosion is most extensive at the peak corrosion conditions, hence the analysis being performed in this manner. The study compared the value of enhanced corrosion as well as enhanced corrosion's overall percent contribution to the total corrosion experienced.

A plot of the corrosion experienced at each peak condition is shown in Figure 4.24. The figure expresses the maximum corrosion experienced at each flow velocity in terms of pure corrosion and enhanced corrosion. As expected from prior results, the pure corrosion rate increases linearly with increasing flow velocity. The total corrosion, depicted by the addition of both bars, also appears to increase linearly, even though the maximum corrosion rates occurred at different

slurry concentrations. Flow velocities of 2.5 and 3.0 m/s showed very similar magnitudes of enhanced corrosion, both shown as 1.1 g/m^{2}hr. The largest magnitude of enhanced corrosion was experienced at a flow velocity of 3.5 m/s and 7 wt.% slurry concentration and was measured to be 1.4 g/m^{2}hr. At 4.0 m/s and 5 wt.% solids, the enhanced corrosion decreased.

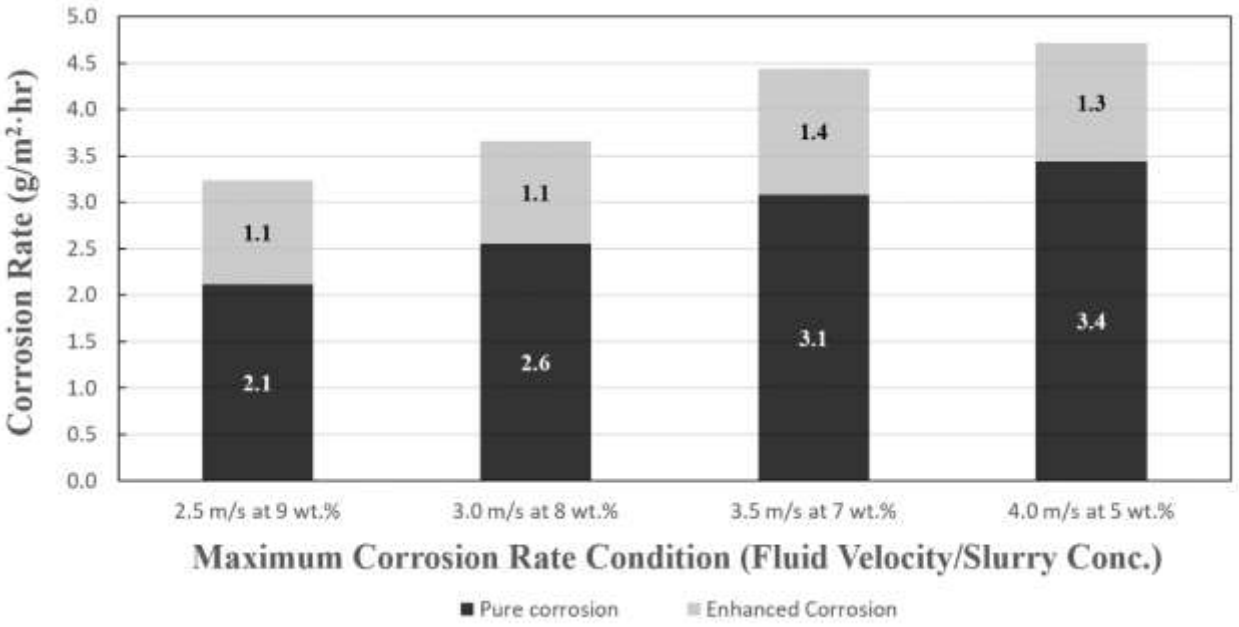

Figure 4.24. Total corrosion experienced at peak operating conditions using the 1.05 mm particle size.

A plot of the enhanced corrosion as a percentage of the overall corrosion experienced is shown in Figure 4.25. Figure 4.25 strongly contrasts the data displayed in Figure 4.24. From the figure, a clear trend of decreasing synergistic contribution as flow velocity increases is shown. Enhanced corrosion had the most considerable effect on the overall corrosion experienced at a flow velocity of 2.5 m/s and 9 wt.% slurry concentration measuring 34.6%. Enhanced corrosions contribution at higher flow velocities steadily decreased to 26.9% at a flow velocity of 4.0 m/s and 5 wt.% slurry concentration. These results provide evidence that enhanced corrosion and the synergism between erosion and corrosion may be most influential at lower flow velocities. The evidence suggests the interaction between erosion and corrosion that leads to enhanced corrosion

may become weaker at higher flow velocities, even while the overall enhanced corrosion increases.

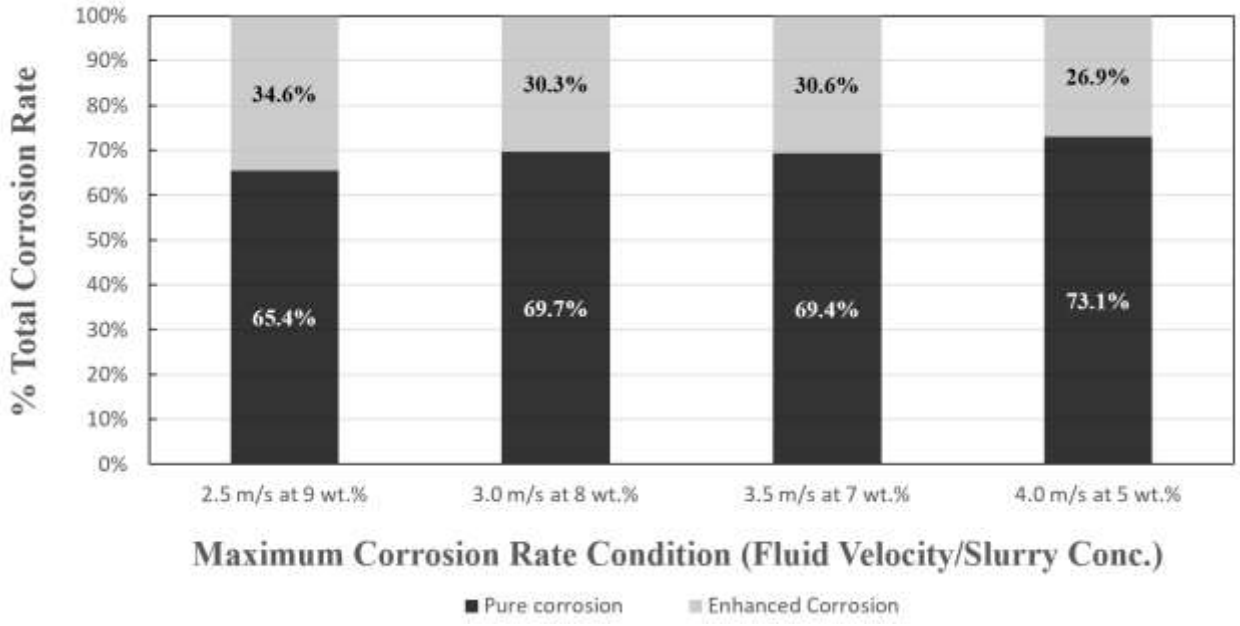

Figure 4.25. Percent contribution of pure (flow assisted) corrosion and enhanced corrosion to the total corrosion experienced at peak operating conditions using the 1.05 mm particle size.

4.7.4 Effect of Slurry Concentration and Flow Velocity on Enhanced Corrosion – 0.55 mm Particles

Similar to the analysis of Section 4.7.3, the enhanced corrosion was examined for the 0.55 mm particle size at their peak corrosion conditions.

A plot of the corrosion experienced at each peak condition is shown in Figure 4.26. The figure expresses the maximum corrosion experienced at each flow velocity in terms of pure corrosion and enhanced corrosion. Again, the pure corrosion rate increases linearly with increasing flow velocity. The total corrosion, depicted by the addition of both bars, also appears to increase linearly, even though the maximum corrosion rates occurred at different slurry concentrations. The enhanced corrosion was smallest at a flow velocity of 2.5 and 10 wt.% slurry concentration

with a magnitude of 1.2 g/m^{2}hr. Enhanced corrosion generally increased with flow velocity up to 1.5 g/m^{2}hr measured at a flow velocity of 4.0 m/s and 5 wt.% slurry concentration.

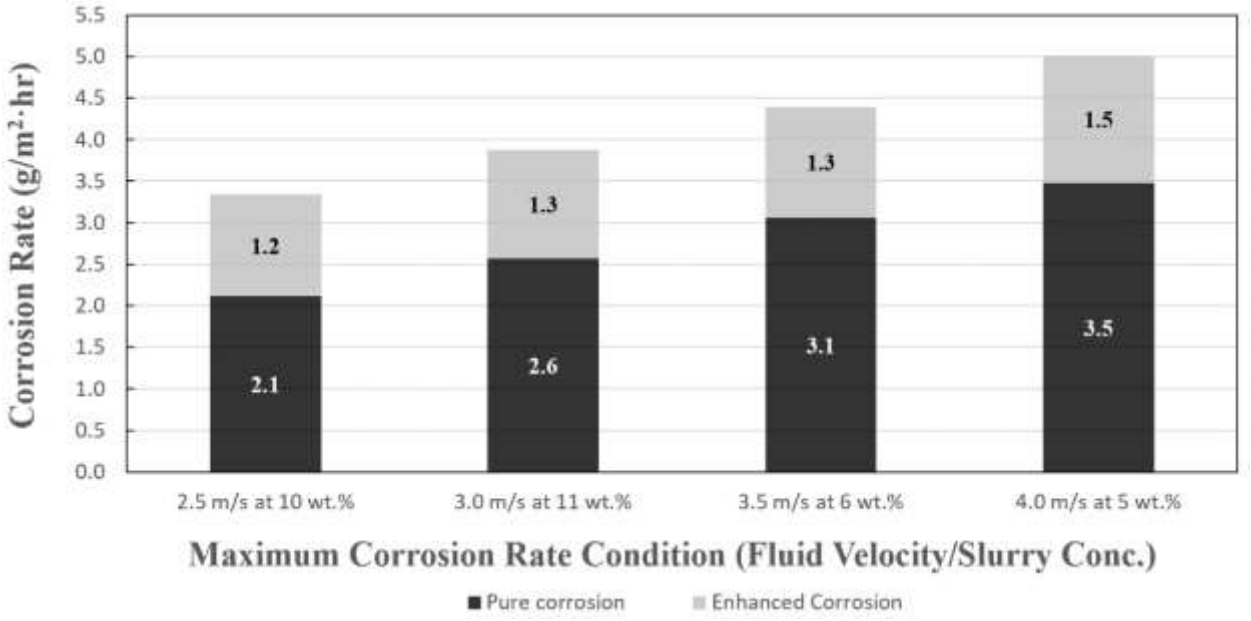

Figure 4.26. Total corrosion experienced at peak operating conditions using the 0.55 mm particle size.

A plot of the enhanced corrosion as a percentage of the overall corrosion experienced is shown in Figure 4.27. These results show more clearly which conditions have the most synergistic interaction between erosion and corrosion. Similar to the 1.05 mm particle results, enhanced corrosion's contribution to the total corrosion rate generally decreased with the increasing flow velocity. Enhanced corrosion had the most considerable contribution at a flow velocity of 3.0 m/s and 11 wt.% solids measured at 36.5%. The smallest contribution from enhanced corrosion was observed at a flow velocity of 3.5 m/s and 6 wt.% solids measured at 30.3%. Although a definitive trend was unclear as the percent contributions increased and decreased with changing conditions, a general decreasing trend was assumed when observed from 2.5 m/s to 4.0 m/s. These results suggest lower flow velocities (2.5 and 3.0 m/s) produce more significant enhanced corrosion than higher flow velocities (3.5 and 4.0 m/s). Therefore, the mechanisms which drive enhanced corrosion may be more prominent at lower flow velocities and lower energy particle

impacts. At higher flow velocities, the process may become erosion dominated and the contribution of enhanced corrosion decreases.

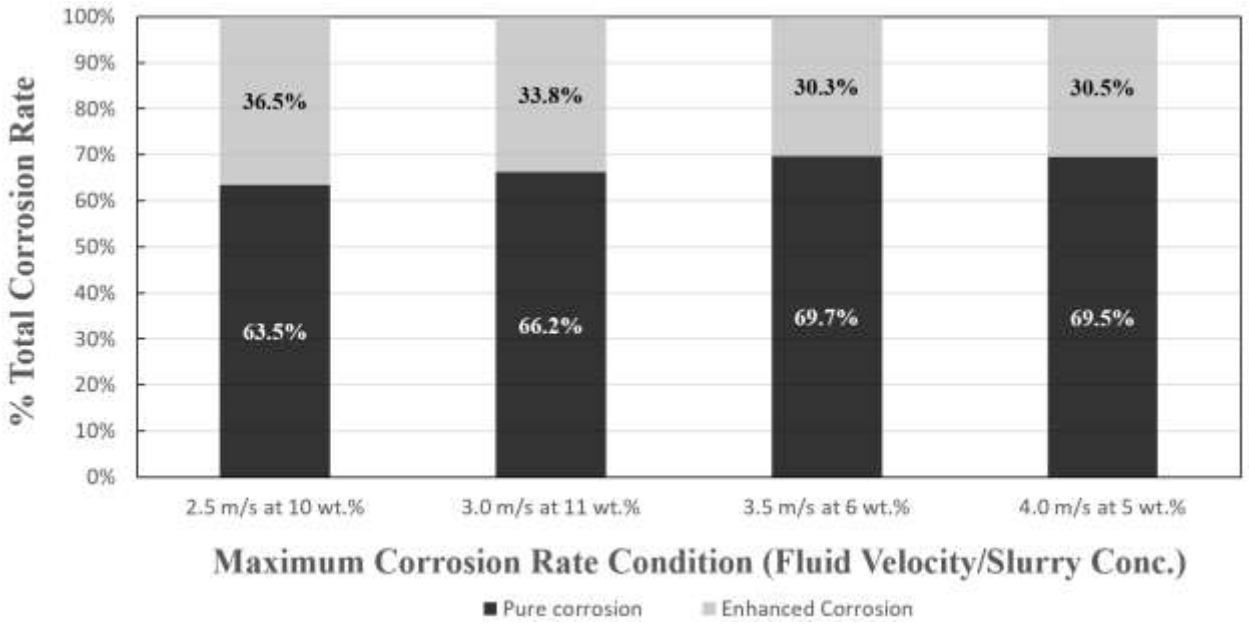

Figure 4.27. Percent contribution of pure (flow assisted) corrosion and enhanced corrosion to the total corrosion experienced at peak operating conditions using the 0.55 mm particle size.

4.7.5 The Effect of Particle Size on Enhanced Corrosion

The particle size effect on the enhanced corrosion was determined using the results from Sections 4.7.3 and 4.7.4. The most meaningful comparison between the particle sizes and the enhanced corrosion they produce was the absolute magnitude and relative contribution to the total corrosion experienced. The peak corrosion conditions of the 1.05 mm particle were 9, 8, 7, and 5 wt.% slurry concentration for flow velocities of 2.5, 3.0, 3.5, and 4.0 m/s. The peak corrosion conditions of the 0.55 mm particle were 10, 11, 6, and 5 wt.% for flow velocities of 2.5, 3.0, 3.5, and 4.0 m/s, respectively. At each peak corrosion condition, the enhanced corrosion occurring is also a maximum.

Figure 4.28 compares the magnitude of the enhanced corrosion found at the peak corrosion condition for each flow velocity and particle size. From the figure, there is evidence of a distinct

separation in the enhanced corrosion experienced between the particle sizes. The smaller particle exhibited, on average, 0.15 g/m^{2}hr more enhanced corrosion than the larger particle. Despite the difference in magnitude, the slopes of both trendlines appear similar. The similar slopes may suggest a simple step shift in enhanced corrosion had occurred due to decreasing the particle size. The effect of flow velocity on the enhanced corrosion experienced was the same regardless of particle size, reflected in both lines having similar positive slopes.

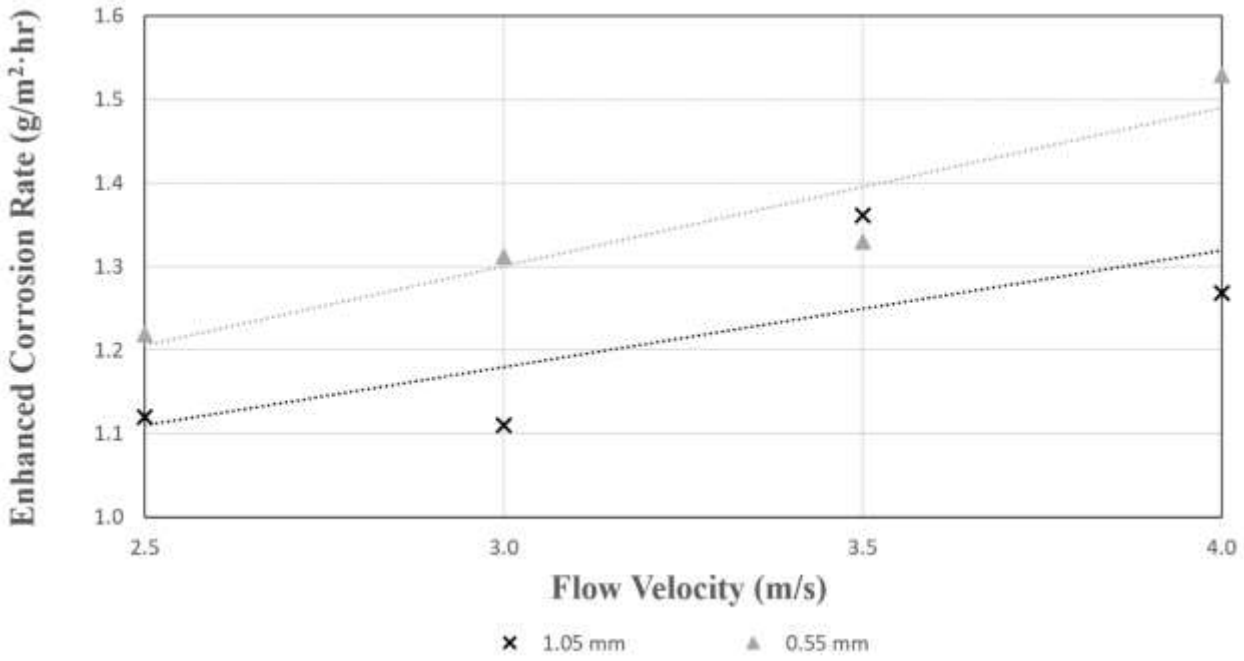

Figure 4.28. Comparison of the enhanced corrosion experienced for 1.05 mm and 0.5 mm particles at their peak corrosion conditions in saturated potash brine.

Figure 4.29 compares the percent contribution of enhanced corrosion to the total corrosion experienced for each particle size. The figure shows the different particle sizes appear to have the same trend and similar slopes. As the flow velocity increased, the contribution of enhanced corrosion decreased. Similar to Figure 4.28, the 0.55 mm particle had a larger percent of its corrosion caused by enhanced corrosion. On average, the 0.55 mm particle's enhanced corrosion had a 2% greater contribution towards the total corrosion experienced than the 1.05 mm particle.

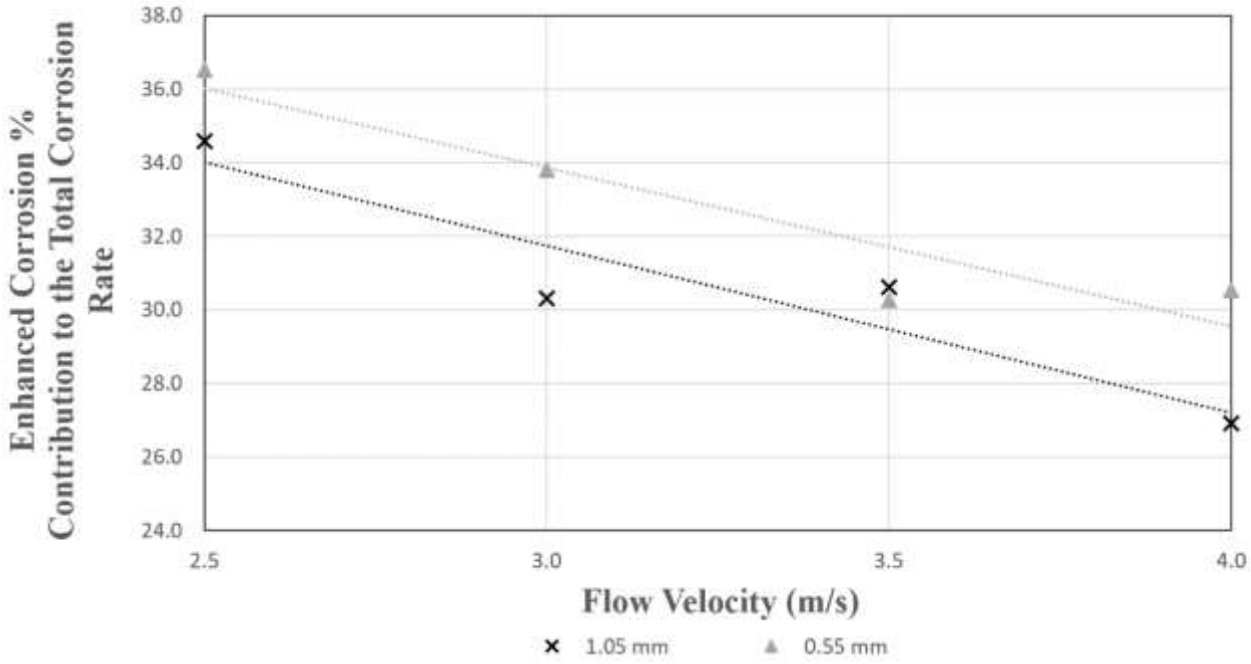

Figure 4.29. Comparison of enhanced corrosions percent contribution to the total corrosion rate at peak corrosion conditions for 1.05 mm and 0.55 mm particles in saturated potash brine.

4.7.6 Discussion of the Enhanced Corrosion of AISI 1018 Carbon Steel Elbows

For all flow velocities and particle sizes tested, enhanced corrosion was experienced at slurry concentrations greater than 0 wt.%. Figure 4.28 showed that higher flow velocities produce more significant enhanced corrosion. Enhanced corrosion occurs from a second phase accelerating the corrosion mechanism(s). At higher flow velocities, sand particles have greater energies and the number of overall impingements increases. Enhanced corrosion depends on the interaction between a solid particle and the metal surface. It could be assumed that enhanced corrosion may increase as the interaction between solid particles and the metal surface increases. Mechanisms of enhanced corrosion that describe the synergy experienced in this research include: corrosion attacking crater lips from impingements, an increased surface area created from surface roughening, and impingements causing work-hardened or strained metal which corrosion preferentially attacks (Wang and Stack, 2000). In each of the aforementioned mechanisms, both the particle energy and the number of impingements will change the mechanism's rate and severity. Additionally, as the concentration of solid particles increases, the mass transfer of

oxygen reaching the metal surface increases. The increase in oxygen mass transfer occurs as the fluid becomes more turbulent and well mixed at higher particle (Guo H. , 2006). Therefore, as flow velocity increases, the enhanced corrosion mechanisms will also increase, matching this research's results.

An interesting observation of the results showed that while the magnitude of enhanced corrosion increased with flow velocity, enhanced corrosion's overall contribution to the total corrosion decreased. The decrease in contribution may suggest that higher flow velocities, while creating more extensive enhanced corrosion, produce less synergistic interactions between erosion and corrosion and may promote more natural corrosion mechanisms. Furthermore, even though flow assisted corrosion (pure corrosion) and enhanced corrosion increased linearly with flow velocity, they increased at different rates (see Figure 4.24 and 4.26). Flow assisted corrosion had a more positive slope than enhanced corrosion from increasing flow velocity. The imbalance at which both types of corrosion increased with flow velocity may be why enhanced corrosion's overall contribution decreased as flow velocity increased.

The smaller particles in this research were shown to experience more enhanced corrosion and more significant synergistic interactions than larger particles. The main difference between large and small particles is their mass (which increases with particle size) and the number of impingements (which decrease with particle size). The smaller particles tested would have had less momentum and kinetic energy per impact than the larger particles; however, they impacted the surface more frequently. The results suggest that enhanced corrosion may be more significant using smaller particles with less kinetic energies and larger impingement rates. Therefore, the mechanism that drives enhanced corrosion may be more attributed to the number of impingements compared to the severity of impact. Impingements, regardless of energy, are known to increase corrosion from surface roughening, the strain-effect, and providing locations for corrosion to preferentially attack such as crater lips and metal dislocations/micro-cracks (Wang and Stack, 2000). The results would suggest that while individual craters made by larger particles do roughen the metal surface, the surface area of the metal may be increased more from smaller particles and a greater number of impingements. In addition, the strain produced on the metal surface (creating work-hardened metal) may be more significant from smaller particles impacting the body more frequently, creating a ‘shot peening’ effect (Wood and Hutton, 1990).

Smaller particles may also increase the local mass transfer of oxygen to the metal surface from better agitation and turbulence caused by a larger number of individual particles present per unit weight of solids. The concept of collision efficiency, the balance between impact energy and the number of impingements, becomes essential when comparing particle size's effect on enhanced corrosion (Xie *et al.*, 2003).

The results displayed that a simple step change may explain the particle size's impact on the enhanced corrosion experienced. The slopes depicting how enhanced corrosion changed with flow velocity were equal for both particle sizes. The equal slopes imply that particle size’s effect on the enhanced corrosion may be independent of flow velocity or slurry concentration. It may be possible that the effect of particle size on enhanced corrosion could be modelled by a simple y-axis step shift (when the y-axis represents the magnitude of enhanced corrosion). In general, the results in this thesis only display two particle sizes. Accurate and clear trends on how particle size affects enhanced corrosion would require more particle sizes for experimentation.

5. Conclusions and Recommendations

5.1 Conclusions

In this research, erosion-corrosion during potash-sand slurry flow was studied by cathodically protecting AISI 1018 carbon steel elbows and measuring the current density required to inhibit corrosion. The experimental parameters studied for their respective effects on the protection current density (i_{prot}) included flow velocity, slurry concentration, and particle size. The measured values of protection current density provide insights into the corrosion and enhanced corrosion of AISI 1018 carbon steel during potash-sand slurry flow. Additionally, the study determined a correlation between protection current density and the corrosion rate it inhibits. From the presented research, the following conclusions were made:

1. The i_{prot} required to inhibit corrosion on AISI 1018 carbon steel was shown to be non-linearly dependent to the slurry concentration. As slurry concentration increased above 0 wt.%, i_{prot} increased. At slurry concentrations ranging between 6-11 wt.% (dependent on flow velocity and particle size), i_{prot} reached a maximum value. Once the maximum i_{prot} occurred, i_{prot} decreased with additional slurry concentration. The increase in i_{prot} from the addition of slurry concentration was possibly attributed to the sand particles increasing the local mass transfer of oxygen to the metal's surface as oxygen is a primary driving force of the corrosion reaction. In addition, synergistic interactions between erosion and corrosion likely caused enhanced corrosion. Enhanced corrosion acts to further increase the required i_{prot} from: (1) increasing the stored strain in the metal from impingements developing more active anodic regions; (2) developing work-hardened metal which is preferentially attacked by corrosion and; (3) corrosion attacking flaked edges made from craters. The presence of a maximum i_{prot} suggests there may be a mass transfer ceiling in which the corrosion reaction becomes the rate-determining step (instead of the mass transfer of oxygen to the metal’s surface). This result may be useful in industrial scenarios where corrosion is the dominant mechanism in erosion-corrosion, and the slurry concentration can be varied. The decrease in i_{prot} at higher slurry concentrations may have been attributed to particle-particle interactions, which decrease

fluid mixing; or sand blanketing the inner elbow surface (from centrifugal forces), limiting oxygen diffusion from the fluid to the metal.

2. The i_{prot} required to inhibit corrosion on AISI 1018 carbon steel was shown to be linearly dependent on the flow velocity. As flow velocity increased, i_{prot} increased linearly in response. The research suggested that i_{prot} increased from more significant amounts of turbulence and mixing in the slurry at higher flow velocities. The linearity of i_{prot} and flow velocity may have been caused by the mass transfer of oxygen being linearly dependent to the flow velocity.
3. In this research, slurries containing the smaller particle (0.55 mm) required a greater i_{prot} to inhibit corrosion than the larger (1.05 mm) particle. This conclusion suggests smaller particles may lead to more corrosion in slurries. The difference in i_{prot} between the particle sizes was enhanced at higher slurry concentrations. The large difference in i_{prot} at higher slurry concentrations lead to the notion that larger particles may be more favourable at higher slurry concentrations concerning corrosivity. The differences between particle sizes and their effect on the in-situ corrosion were also explored using collision efficiency. Collision efficiency considers the number of impacts and the energy of each impact toward the total erosion-corrosion experienced. Smaller particles were shown in this research to cause more significant corrosion and, therefore, may suggest the number of impacts on the metal surface is more significant than the energy of each impact concerning corrosion activity.
4. The research found a correlation between the corrosion rate of AISI 1018 carbon steel and the i_{prot} required to inhibit corrosion. This correlation was determined to be linear for all flow velocities and slurry concentrations presented in this research. The linear correlation suggested that i_{prot}, as found through cathodic protection, may be used as a method to predict corrosion rates for single or two-phase flow systems. The linear relationship may prove useful in both industry and lab settings as a corrosion observation method that is non-intrusive and non-destructive.
5. Enhanced corrosion caused by the synergistic interaction of erosion and corrosion existed at all slurry concentrations greater than 0 wt.% regardless of flow velocity or particle size. Enhanced corrosion in this research was likely caused by erosion: (1) increasing the surface area of the metal exposed to corrosion, (2) increasing the stored strain in the

metal surface creating more active anodic sites at dislocations, (3) crater impacts disrupting/changing dislocations and developing microcracks leading to increased surface area, and (4) creating work-hardened metal which corrosion preferentially attacks. Experimental results showed that the enhanced corrosion of AISI 1018 carbon steel increased with the slurry's flow velocity. Conversely, the percent contribution of enhanced corrosion to the total corrosion experienced decreased with the flow velocity. Results further showed the 0.55 mm particle size produced greater amounts of enhanced corrosion and a more corrosive environment than the 1.05 mm particle. Enhanced corrosion appeared to be most affected by the number of impingements occurring on the metal surface regardless of the kinetic energy. Due to this result, smaller particles that impacted the surface more frequently showed more significant enhanced corrosion than larger particles.

5.2 Recommendations

The following recommendations are made in conclusion of this research:

1. Research should be performed in the same manor of this thesis on both larger and smaller particle sizes beyond those presented in this research. While inferences and observations were made about the effect of particle size on erosion-corrosion, larger data sets are required to make clear conclusions.
2. The presented research explored the use of cathodic protection to examine erosion-corrosion of 1018 carbon steel. Future experiments should explore various electrolytes and materials to observe the trends of cathodic current density as a function of flow velocity and slurry concentration. Higher resistance electrolytes (such as petrochemicals) may be of interest to study for its wide use in western Canada.
3. Future experiments performed in a similar fashion to this thesis should include additional manipulated variables such as temperature, viscosity, and conductivity. Each of these variables may play an important role in the severity of erosion-corrosion.

4. Cathodic protection is widely used in industry and there is potential for improvement in its industrial application and the understanding of its ability/limitations. The use of cathodic protection to study corrosion and erosion-corrosion should continue to be explored, and the study of cathodic protection itself may lead to improvements in its industrial application and structure integrity.

References

Abd-El-Kader, H., and El-Raghy, S. (1986). Wear Corrosion Mechanism of Stainless Steel in Chloride Media. *Corrosion Science, Vol. 26*, 647-653.

Anaee, R. A., and Abdulmajeed, M. (2016). Chapter 5: Tribocorrosion. In P. H. Darji, *Advanced in Tribology* (pp. 89-110). London, England: IntechOpen.

Andrews, N., Giourntas, L., Galloway, A., and Pearson, A. (2014). Effect of Impact Angle on the Slurry Erosion-Corrosion of Stellite 6 and SS316. *Wear, Vol. 320*, 143-151.

Applegate, L. M. (1973). *Cathodic Protection.* New York: McGraw-Hill Book Company Inc. .

ASTM. (1994). *ASTM G119-09: Standard Guide for Determining Synergism Between Wear and Corrosion.* USA: ASTM International.

ASTM. (1999). *Standard Practice for Calulation of Corrosion Rates and Related Information from Electrochemical Measurements.* West Conshohocken, PA: The American Society for Testing and Materials (ASTM).

Bahadori, A. (2014). Cathodic Corrosion Protection Systems - A Guide for Oil and Gas Industries. Oxford, United Kingdom: Gulf Professional Publishing.

Barik, R., Wharton, J., Wood, R., and Stokes, K. (2009). Electro-Mechanical Interactions during Erosion-Corrosion. *Wear, Vol. 267*, 1900-1908.

Batchelor, A., and Stachowiak, G. (1988). Predicting Synergism Between Corrosion and Abrasive Wear. *Wear, Vol. 123*, 281-291.

Benerskog, B., and Puigdomenech, I. (1996). Revised Poubaix Diagrams for Iron at 25-300°C. *Corrosion Science, Vol. 38*, 2121-2135.

Bird, R. B., Stewart, W. E., and Lightfoot, E. N. (2007). *Trasnport Phenomena - Revised Second Edition.* New York: Wiley.

Bosich, J. F. (1970). *Corrosion Prevention for Practicing Engineers.* New York: Barnes and Noble.

Broughton, P. L. (2019). Economic Geology of Southern Saskatchewan Potash Mines. *Ore Geology Reviews, Vol. 113*, 103-117.

Byrne, A., Holmes, N., and Norton, B. (2015). Cathodic Protection for Reinforced Concrete Structures: Present Practise and Moves Toward using Renewable Energy. *Dublin Institute of Technology*.

Cao, S., Maldonado, S. G., and Mishler, S. (2015). Tribocorrosion of passive metals in the mixed lubrication regime: theoretical model and application to metal-on-metal artificial hip joints. *Wear, Vol. 324-325*, 55-63.

Chaudahri, S., Banerji, T., and Kumar, R. (2014). Chapter 7: Domestic and Community-Scale Arsenic removal Technologies Suitable for Developing Countries. In S. Ahuja, *Water Reclamation and Sustainability* (pp. 155-182). Mumbai, India: Centre for Environmental Science and Engineering, Indian Institute of Technology.

Cimbala, Y. A., and Cengal, J. M. (2006). Fluid Mechanics: Fundementals and Applications. In Y. A. Cimbala, and J. M. Cengal. Boston: McGraw-Hill Higher Education.

Clark. (2002). Particle Velocity and Size Effects in Laboratory Slurry Erosion Measurements OR... do you know what your particles are doing? *Tribology International, Vol. 35*, 617-624.

Clark, H. M., and Wong, K. (1995). Impact Angle, Particle Energy and Mass Loss in Erosion by Dilute Slurries. *Wear, Vol. 248*, 454-464.

Clark, H., and Hartwich, R. B. (2001). A Re-Examination of the 'Particle Size Effect' in SLurry Erosion. *Wear, Vol. 186-187*, 147-161.

Dai, L., Wang, D., Wang, T., Feng, Q., and Yang, X. (2017). Analysis and Comparison of Long-Distance Pipeline Failures. *Journal of Petroleum Engineering, Vol. 2017*, 1-7.

Davis, J. (2000). *Corrosion: Understanding the Basics.* Ohio: ASM International.

Elemuren, R. (2020). *Erosion-Corrosion Study of Carbon Steel and Duplex Stainless Steel Elbows in Potash Brine-Sand Slurry (Ph.D. Thesis).* Saskatoon, SK: University of Saskatchewan.

Elemuren, R., Evitts, R., Oguocha, I., Kennell, G., Gerspacher, R., and Odeshi, A. (2018). Slurry Erosion-Corrosion of 90° AISI 1018 Carbon Steel Elbows in Saturated Potash Brine containing Abrasive Silica Particles. *Wear, Vol. 410-411*, 149-155.

Elfstrom, B. (1980). The Effect of Chloride Ions on Passive Layers on Stainless Steels. *Materials Science and Engineering, Vol. 42*, 173-180.

Evitts, R. W. (2005). Chapter 11 - Cathodic Protection. In W. Andrew, *Handbook of Environmental Degradation of Materials* (pp. 229-241). Delmar, New York: Myer Kutz Associates, Inc.

Eyres, D. J., and Bruce, G. (2012). Chapter 27 - Corrosion Control and Antifouling Systems. In *Corrosion Control and Antifouling (Seventh Edition)* (pp. 327-343). Butterworth-Heinemann.

Giourntas, L., Hodgkiess, T., and Galloway, A. (2015). Comparative Study of Erosion-Corrosion Performance on a range of Stainless Steels. *Wear, Vol. 332-333*, 1051-1058.

Guo, H. (2006). *Synergism in Erosion-Corrosion Caused by Interaction of Electrochemical and Mechanical Factors (Ph.D. Thesis).* Edmonton: University of Alberta.

Guo, H., Lu, B. T., and Luo, J. L. (2005). Interaction of Mechanical and Electrochemical Factors in Erosion-Corrosion of Carbon Steel. *Electrochemica Acta, Vol. 51*, 315-323.

Hansson, C. (2011). The Impact of Corrosion on Society. *Metallurgical and Materials Transactions A, Vol. 42*, 2952 - 2962.

Harvey, T. J., Wharton, J., and Wood, J. (2007). Development of Synergy Model for Erosion-Corrosion of Carbon Steel in a Slurry Pot. *Tribology - Materials, Surfaces, & Interfaces, Vol. 1*, 33-47.

Heppner, K., and Evitts, R. (2005). A Hybrid Differencing Scheme for Mass Transport in Electrochemical Systems. *International Journal of Numerical Methods for Heat and Fluid Flow, Vol. 15*, 842-862.

Huang, Y., and Zhang, J. (2018). *Materials Corrosion and Protection (3rd Ed.).* Shanghai: Shanghai Jiao Tong University Press.

Huang, Y., Ogoucha, I., and Yannacopoulos, S. (2005). The corrosion wear behaviour of selected stainless steels in potash brine. *Wear, Vol. 258*, 1357-1363.

Hussain, E., and Robinson, M. (2007). Erosion-Corrosion of 2205 Duplex Stainless Steel in Flowing Seawater Containing Sand Particles. *Corrosion Science, Vol. 49*, 1737-1754.

Hutchings. (1986). *The Erosion of Material by Liquid Flow* (Vol. 25). Materials Technology Institute of the Chemical Process Industries.

Hutchings, I. (1987). Wear by Particulates. *Chemical Engineering Science, Vol. 42*, 869-878.

Islam, M. A., and Farhat, Z. (2017). Erosion-corrosion mechanism and comparison of erosion-corrosion performance of API steels. *Wear, Vol. 376-377*, 533-541.

Islam, M. A., Farhat, Z., Ahmed, E., and Alfantazi, A. (2013). Erosion Enhanced Corrosion and Corrosion Enhanced Erosion of API X-70 Pipeline Steel. *Wear, Vol. 302*, 1592-1601.

Jiang, J., Xie, Y., Islam, M. A., and Stack, M. M. (2017). The Effect of Dissolved Oxygen in Slurry on Erosion-Corrosion of En30B Steel. *Journal of Bio Tribo Corrosion, Vol. 3*, 3-45.

Jiang, X. X., Tao, D., Li, S., and Yang, J. (1993). Accelerative Effect of Wear on Corrosion of High-Alloy Stainless Steels. *Corrosion Science - NACE, Vol. 49*, 836-841.

Kean, R. (1981). *Cathodic Protection.* United Kingdom: National Physics Laboratory.

Keating, A., and Nesic, S. (1999). Prediction of Two-Phase Erosion-Corrosion in Bends. *CSIRO International Conference on CFD in the Minerals and Process Industries, Vol. 6-8*, 229-236.

Kesavan, S., Mozhi, T., and Wilde, B. (1989). Technical Note: Potential-pH Diagrams for the Fe-Cl-H20 System from 25 to 150 °C. *Corrosion Science, Vol. 45*, 213-215.

Kim, K., Bhattacharyya, S., and Agarwala, V. (1981). Electrochemical Polarization Technique for Evaluation of Wear-Corrosion in Moving Components under Stress. *Wear of Materials*, 772-778.

Koch, G., Varney, J., Thompson, N., Moghissi, O., Gould, M., and Payer, J. (2016). *International Measures of Prevention, Application, and Economics of Corrosion Technologies Study.* Houston: NACE International.

Kotlyar, D., Pitt, C., and Wadsworth, M. (1988). Simultaneous Corrosion and Abrasion Measurements under Grinding Conditions. *Corrosion, Vol. 44*, 221-228.

Li, J., Tekie, Z., Mizan, T., Morsi, B., Maier, E., and Singh, C. (1996). Gas-Liquid Mass Transfer in a Slurry Reactor Operating under Olefinic Ploymerization Process Conditions. *Corrosoin Engineering Science, Vol. 51*, 549-559.

Li, Y., Burstein, G., and Hutchings, I. (1995). Influence of Environmental Composition and Electrochemical Potential on the Slurry Erosion-Corrosion of Aluminum. *Wear, Vol. 181-183*, 70-79.

Lorenzi, S., Pastore, T., Bellezze, T., and Fratesi, R. (2016). Cathodic Protection Modelling of a Propeller Shaft. *Corrosion Science, Vol. 108*, 36-46.

Lotz, U., and Postlethwaite, J. (1990). Erosion-Corrosion in Disturbed Two Phase Liquid/Particle Flow. *Corrosion Science, Vol. 30*, 96-106.

Lu, B., and Luo, J. (2006). Synergism of Electrochemical and Mechanical Factors in Erosion-Corrosion. *Journal of Physical Chemistry, Vol. 110*, 4217-4231.

Madsen, B. W. (1988). Measurement of Erosion-Corrosion Synergism with a Slurry Wear Test Apparatus. *Wear, Vol. 123*, 127-142.

Malka, R., Nesic, S., and Gulino, D. (2007). Erosion Corrosion and Synergistic Effects in Disturbed Liquid-Particle Flow. *Wear, Vol. 262*, 791-733.

Matsumura, M., Oka, Y., Hiura, H., andYano, M. (1991). The role of Passivating Film in Preventing SLurry Erosion-Corrosion of Austenitic Stainless Steel. *ISIJ International, Vol. 31*, 168-176.

McCafferty, E. (2010). Thermodynamics of Corrosion: Pourbaix Diagrams. In E. McCafferty, *Thermodynamics of Corrosion* (p. 104). Alexandria, Virgina: Springer Nature.

Morgan, J. H. (1959). The Internal Cathodic Protection of Large Steel Pipes Carrying Sea Water. *Corrosion - National Association of Corrosion Engineers, Vol. 15*, 417-422.

Neville, A., and Wang, C. (2009). Erosion-Corrosion Mitigation by Corrosion Inhibitors - An Assessment of Mechanisms. *Wear, Vol. 267*, 195-203.

Noel, R., and Ball, A. (1983). On the Synergistic Effects of Abrasion and Corrosion during Wear. *Wear, Vol. 87*, 351 - 361.

Oka, Y., and Matsumera, M. (1983). Erosive Wear Testing Apparatus-Simulation of Erosion Caused by Slurry of Low-Impingement Velocity. *Int. Conf. on Wear of Materials*, 360-366.

Postlethwaite, J., Tinker, E., and Hawrylak, M. (1974). Erosion-Corrosion in Slurry Pipelines. *Corrosion-NACE, Vol. 30*, 285-290.

Qi, Z., Jingxuan, X., Wei, Z., Shasha, B., Shiteng, Z., and Zhenfeng, C. (2011). Effect of Coal Slurry on the Corrosion of Coal-Mine Equipment. *Mining Science and Technology, Vol. 21*, 413-417.

Rajahram, S., Harvey, T., and Wood, R. (2009). Erosion-Corrosion Resistance of Engineering Materials in Various Test Conditions. *Wear, Vol. 267*, 244-254.

Rajahram, S., Harvey, T., and Wood, R. (2011). Electrochemical Investigation of Erosion-Corrosion Using a Slurry Pot Erosion Tester. *Tribology International, Vol. 44*, 232-240.

Reger, D., Goode, S. R., and Ball, D. W. (2010). *Chemistry: Principles and Practice 3rd Ed.* Boston, MA: Cengage Learning.

Saleh, B., and Ahmed, S. (2013). Slurry Erosion-Corrosion of Carburized AISI 5117 Steel. *Tribology Letters, Vol. 51*, 135-142.

Schall, J. M., and Myerson, A. S. (2019). *Handbook of Industrial Crystalization, 3rd Ed.* . Cambridge University Press.

Schmidtchen, U. (2009). Fuels - Safety: Hydogen: Overview. In J. Garche, *Enclyclopedia of Electrochemical Power Sources* (pp. 519-527). Elsevier Science.

Song, F. M., and Du, L. X. (2017). Erosion-Corrosion of Low-Alloy Wear-Resistant Steels in Alkaline Slurry. *Journal of Iron and Steel Research, Vol. 24*, 1065-1072.

Stack, M., Corlett, N., and Turgoose, S. (2003). Some Thoughts on Modelling the Effects of Oxygen and Particle Concentration on the Erosion-Corrosion of Steels in Aqueous Slurries. *Wear, Vol. 255*, 225-236.

Stack, M., Scott, F., and Wood, G. (1993). Review of Mechanisms of Erosion-Corrosion of Alloys at Elevated Temperatures. *Wear, Vol. 162-164*, 706-712.

Strathdee, G. (1996). Performance of Materials in Potash Production. *Phosphorous and Potassium N205*, 33-40.

Syed, B. A., and Siddiqui, F. I. (2012). Use of Vertical Electrical Sounding (VES) Method as an Alternative to Standard Penetration Test (SPT). *The Twenty-Second (2012) International Offshore and Polar Engineering Conference*, 871-875.

Tro, N. J. (2008). Chemistry: A Molecular Approach. In N. J. Tro, *Electrochemistry* (pp. 818-863). Upper Saddle River, New Jersey: Pearson Prentice Hall.

Wang, C., Neville, A., Ramachandran, S., and Jovancicevic, V. (2005). Alleviation of Erosion-Corrosion Damage by Liquid-Sand Impact through the use of Chemicals. *Wear, Vol. 258*, 649-658.

Wang, H., and Stack, M. (2000). The Erosive Wear of Mild and Stainless Steels Under Controlled Corrosion in Alkaline Slurries Containing Alumina Particles. *Journal of Materials Science*, 5263-5273.

Wang, S. H., Jiang, J., and Stack, M. M. (2015). Methodology Development for Investigation of Slurry Abrasion Corrosion by Integrating an Electrochemical Cell to a Miller Tester. *Biological Tribo Corrosion, Vol. 35*, 1-9.

Watson, S., Friedersdorf, F., Cramer, S., and Madsen, B. (1995). Methods of Measuring Wear-Corrosion Synergism. *Wear, Vol. 181-183*, 476-484.

Wood, R., and Hutton, S. (1990). The Synergistic Effect of Erosion and Corrosion: Trends in Published Results. *Wear, Vol. 140*, 387-394.

Woods, R., and Jones, T. (2003). Investigations of sand–water induced erosive wear of AISI 304L stainless steel pipes by pilot-scale and laboratory-scale testing. *Wear, Vol. 255*, 206-218.

Wolfbauer, C. (1977). Mineral Resources for Agricultural Use. In W. Lockeretz, *Agriculture and Energy* (pp 301-314). Cambridge, USA*:* Academic Press

Xie, J., Alpas, A., and Northwood, D. (2003). The Effect of Erosion on the Electrochemical Properties of AISI 1020 Steel. *Journal of Materials Engineering and Performance, Vol. 12*, 77-86.

Xie, Y., Jiang, J., Tufa, K. Y., and Yick, S. (2015). Wear Resistance of Materials used for Slurry Transport. *Wear, Vol. 332-333*, 1104-1110.

Xu, Y., Liu, L., Zhou, Q., Wang, X., Tan, M. Y., and Huang, Y. (2020). An Overview of Major Experimental Methods and Apparatus for Measuring and Investigating Erosion-Corrosion of Ferrous-Based Steels. *Metals, Vol. 10*, 10 - 180.

Yabuki, A. (2011). Mass Transfer Equation and Hydrodyanmic Effects in Erosion-Corrosion. In M. El-Amin, *Advanced Topics in Mass Transfer* (pp. 193-210). Rijeka, Croatia: InTech.

Yabuki, A., Sugita, K., Matsumura, M., Hirashima, M., and Tsunaga, M. (2000). The Anti-Slurry Erosion Properties of Polyethylene for Sewage Pipe Use. *Wear, Vol. 240*, 52-58.

Yang, J., and Swisher, J. (1993). Erosion-Corrosion Behaviour and Cathodic Protection of Alloys in Seawater-Sand Slurries. *Journal of Materials Engineering and Performances, Vol. 2*, 843-850.

Yang, Y., and Cheng, Y. (2012). Parametric Effects on the Erosion-Corrosion Rate and Mechanisms of Carbon Steel Pipes in Oil Sands Slurry. *Wear, Vol. 276-277*, 141-148.

Yao, Z., Zheng, Y., and Ke, W. (1995). The Influence of Applied Potential on the Erosion-Corrosion Behaviour of AISI 321 Stainless Steel in Acidic Slurry Medium. *Wear, Vol. 186*, 568-572.

Yue, Z., Zhou, P., and Shi, J. (1987). Some Factors Influencing Corrosion-Erosion Performance of Materials. *Wear of Materials, Vol. 2*, 763-770.

Zeng, L., Guo, S., and Zhang, G. (2016). Erosion-Corrosion of Stainless Steels at Different Locations of a 90° Elbow. *Corrosion Scince, Vol. 111*, 72-83.

Zheng, Y., Yao, Z., and Ke, W. (2000). Erosion-Corrosion Resistant Alloy Development for Aggressive Slurry Flows. *Materials Letters, Vol. 46*, 362-368.

Zheng, Y., Yao, Z., Wei, X., and Ke, W. (1995). The Synergistic Effect Between Erosion and Corrosion in Acidic Slurry Medium. *Wear, Vol. 186*, 551-561.

Appendix A

Summation of Phase I Results

This appendix displays the following data:

- Results of current logging experiments to determine the current density required to protect AISI 1018 steel in saturated potash brine (Table A.1)
- Results of the protective potential measured through the center of a galvanically protected, submerged AISI 1018 pipe in saturated potash in:
    - Untreated Potash - (Table A.2)
    - Pure KCl - (Table A.3)
    - Pure NaCl - (Table A.4)
    - Pure $MgCl_2$ - (Table A.5)

Table A.1: Average protective current density measured from galvanically protecting an AISI 1018 carbon steel pipe submerged in saturated potash brine using magnesium over 95 minutes.

Time (min)	Protection Current Density (mA/cm^2)			Average (mA/cm^2)	95% Confidence Interval (mA/cm^2)
	Trial 1	Trial 2	Trial 3		
0	97.7	98.5	116.7	1.13	0.20
5	98.6	92.9	122.6	1.14	0.29
10	98.8	92.2	123.0	1.14	0.30
15	91.8	91.8	122.7	1.11	0.33
20	92.6	91.5	122.4	1.11	0.32
25	92.6	91.4	121.9	1.11	0.32
30	92.5	91.2	121.4	1.11	0.31
35	92.4	91.0	121.2	1.10	0.31
40	92.1	90.8	120.8	1.10	0.31
45	92.0	90.4	120.8	1.10	0.31
50	91.7	90.0	120.6	1.10	0.31
55	91.6	89.6	120.4	1.09	0.32
60	91.4	89.5	120.3	1.09	0.32
65	91.5	90.0	120.2	1.09	0.31
70	91.4	89.6	120.0	1.09	0.31
75	91.3	89.2	120.1	1.09	0.32
80	91.2	88.7	119.8	1.09	0.32
85	91.1	88.3	119.7	1.08	0.32
90	91.1	88.1	119.7	1.08	0.32
95	90.9	87.9	119.6	1.08	0.32

Table A.2: E_{prot} determined at various depths through a galvanically protected AISI 1018 carbon steel pipe submerged in saturated potash brine.

Depth (mm)	Potential ($-mV_{SCE}$)									Average ($-mV_{SCE}$)	95% Confidence Interval (mV_{SCE})
	Trial 1	Trial 2	Trial 3	Trial 4	Trial 5	Trial 6	Trial 7	Trial 8	Trial 9		
0	1363	1350	1345	1328	1329	1329	1330	1320	1318	1335	9
5	1323	1318	1316	1308	1302	1301	1304	1297	1289	1306	7
10	1299	1289	1284	1281	1276	1276	1283	1274	1269	1281	6
15	1278	1267	1262	1260	1257	1257	1267	1256	1253	1262	5
20	1262	1252	1248	1238	1242	1240	1253	1243	1238	1246	5
25	1248	1240	1236	1232	1231	1229	1243	1231	1229	1235	4
30	1237	1231	1227	1224	1221	1220	1229	1223	1221	1226	3
35	1231	1224	1219	1218	1215	1213	1225	1217	1215	1220	4
40	1225	1219	1216	1213	1210	1210	1219	1213	1210	1215	3
45	1222	1216	1213	1210	1207	1207	1216	1211	1209	1212	3
50	1221	1215	1213	1209	1207	1206	1216	1211	1208	1212	3
55	1222	1216	1213	1210	1208	1207	1217	1212	1210	1213	3
60	1225	1219	1217	1213	1211	1210	1220	1214	1212	1216	3
65	1230	1223	1223	1218	1215	1214	1225	1219	1217	1220	3
70	1238	1231	1230	1224	1222	1221	1232	1225	1223	1227	4
75	1247	1242	1239	1233	1231	1230	1242	1237	1234	1237	4
80	1262	1256	1253	1247	1242	1245	1260	1250	1245	1251	4
85	1280	1275	1272	1261	1258	1259	1274	1261	1259	1267	5
90	1302	1297	1295	1279	1274	1276	1292	1279	1277	1286	7
95	1332	1329	1322	1305	1297	1300	1316	1305	1302	1312	8
100	1364	1358	1353	1331	1331	1329	1342	1333	1331	1341	8
102.5	1386	1380	1373	1352	1351	1349	1359	1349	1348	1361	9

Table A.3: E_{prot} determined at various depths through a galvanically protected AISI 1018 carbon steel pipe submerged in saturated KCl.

Depth (mm)	Potential (-mV_{SCE})									Average (-mV_{SCE})	95% Confidence Interval (mV_{SCE})
	Trial 1	Trial 2	Trial 3	Trial 4	Trial 5	Trial 6	Trial 7	Trial 8	Trial 9		
0	1382	1386	1387	1398	1404	1406	1400	1407	1410	1398	6
5	1361	1362	1357	1373	1370	1374	1377	1376	1373	1369	5
10	1337	1342	1341	1348	1349	1350	1351	1351	1350	1347	3
15	1320	1321	1322	1326	1326	1328	1327	1328	1326	1325	2
20	1305	1307	1307	1311	1309	1309	1309	1310	1310	1309	1
25	1294	1295	1293	1298	1298	1297	1297	1296	1296	1296	1
30	1285	1286	1287	1289	1288	1288	1286	1286	1285	1287	1
35	1278	1278	1279	1282	1280	1281	1279	1278	1277	1279	1
40	1274	1275	1276	1278	1277	1276	1274	1273	1273	1275	1
45	1272	1272	1273	1275	1274	1274	1271	1270	1269	1272	1
50	1271	1272	1272	1275	1274	1274	1270	1269	1269	1272	1
55	1273	1274	1274	1277	1276	1276	1272	1271	1270	1274	1
60	1277	1278	1278	1283	1281	1281	1276	1274	1274	1278	2
65	1283	1284	1283	1289	1287	1288	1282	1281	1281	1284	2
70	1291	1291	1292	1299	1297	1296	1291	1289	1290	1293	2
75	1301	1302	1302	1309	1312	1308	1301	1301	1302	1304	3
80	1315	1317	1316	1324	1323	1323	1316	1316	1317	1319	2
85	1332	1335	1335	1345	1345	1345	1337	1336	1337	1339	3
90	1354	1351	1352	1368	1371	1365	1358	1357	1357	1359	4
95	1375	1375	1378	1394	1392	1395	1385	1385	1389	1385	5
100	1406	1404	1404	1429	1427	1430	1419	1419	1419	1417	7
102.5	1422	1422	1423	1446	1448	1447	1440	1440	1439	1436	7

Table A.4: E_{prot} determined at various depths through a galvanically protected AISI 1018 carbon steel pipe submerged in saturated NaCl.

Depth (mm)	Potential (-mV_{SCE})									Average (-mV_{SCE})	95% Confidence Interval (mV_{SCE})
	Trial 1	Trial 2	Trial 3	Trial 4	Trial 5	Trial 6	Trial 7	Trial 8	Trial 9		
0	1093	1083	1099	1106	1100	1097	1077	1068	1062	1087	10
5	1090	1081	1089	1103	1098	1095	1076	1067	1061	1084	9
10	1089	1080	1076	1101	1096	1094	1074	1066	1060	1082	9
15	1086	1080	1070	1099	1094	1092	1073	1065	1060	1080	9
20	1084	1079	1069	1097	1093	1091	1073	1065	1059	1079	8
25	1084	1078	1069	1096	1091	1089	1072	1064	1058	1078	8
30	1082	1076	1068	1094	1090	1088	1071	1063	1058	1077	8
35	1081	1076	1068	1093	1090	1087	1070	1062	1057	1076	8
40	1080	1075	1067	1093	1089	1087	1070	1062	1057	1076	8
45	1079	1077	1067	1092	1089	1087	1069	1062	1056	1075	8
50	1079	1074	1067	1092	1088	1087	1069	1061	1056	1075	8
55	1078	1073	1066	1092	1088	1086	1069	1061	1055	1074	8
60	1078	1074	1066	1092	1089	1087	1068	1062	1056	1075	8
65	1078	1072	1067	1092	1089	1087	1068	1061	1056	1074	8
70	1078	1072	1068	1093	1090	1088	1067	1061	1057	1075	8
75	1077	1072	1068	1094	1091	1089	1068	1061	1057	1075	8
80	1077	1072	1068	1095	1092	1090	1068	1061	1057	1076	9
85	1078	1073	1069	1096	1093	1092	1069	1062	1058	1077	9
90	1079	1074	1069	1097	1095	1093	1069	1063	1059	1078	9
95	1080	1075	1070	1099	1096	1095	1069	1063	1059	1078	9
100	1082	1075	1076	1101	1099	1097	1070	1064	1060	1080	10
102.5	1083	1076	1076	1102	1100	1098	1070	1064	1060	1081	10

Table A.5: E_{prot} determined at various depths through a galvanically protected AISI 1018 carbon steel pipe submerged in saturated $MgCl_2$.

Depth (mm)	Potential (-mV_{SCE})									Average (-mV_{SCE})	95% Confidence Interval (-mV_{SCE})
	Trial 1	Trial 2	Trial 3	Trial 4	Trial 5	Trial 6	Trial 7	Trial 8	Trial 9		
0	1434	1417	1407	1412	1396	1395	1402	1394	1393	1406	8
5	1391	1376	1369	1375	1355	1351	1363	1357	1355	1366	8
10	1350	1336	1323	1334	1314	1309	1326	1319	1319	1326	8
15	1312	1299	1288	1291	1278	1271	1295	1290	1287	1290	7
20	1275	1265	1249	1257	1249	1240	1270	1263	1260	1259	7
25	1249	1234	1223	1234	1220	1216	1248	1242	1242	1234	8
30	1225	1214	1201	1211	1199	1195	1230	1227	1224	1214	8
35	1207	1197	1184	1194	1185	1180	1216	1213	1212	1199	9
40	1196	1186	1174	1185	1176	1171	1209	1206	1204	1190	9
45	1188	1177	1169	1177	1170	1165	1203	1201	1201	1183	9
50	1188	1178	1169	1177	1169	1166	1202	1201	1200	1183	9
55	1193	1183	1173	1181	1173	1170	1205	1203	1203	1187	9
60	1202	1193	1183	1190	1184	1180	1211	1210	1209	1196	8
65	1217	1208	1197	1204	1196	1194	1222	1220	1219	1209	7
70	1237	1229	1219	1221	1215	1211	1235	1236	1233	1226	6
75	1265	1254	1244	1243	1237	1231	1253	1251	1252	1248	6
80	1295	1287	1275	1273	1266	1261	1275	1273	1276	1276	6
85	1330	1321	1314	1307	1297	1293	1303	1303	1303	1308	7
90	1365	1356	1345	1337	1333	1327	1331	1334	1331	1340	8
95	1401	1393	1383	1379	1371	1366	1370	1367	1366	1377	8
100	1442	1438	1430	1423	1417	1410	1413	1412	1413	1422	7
102.5	1468	1459	1453	1446	1439	1435	1439	1435	1438	1446	7

Appendix B

Summation of Phase II Results

This appendix displays the following data:

- Results of the initial testing of the ICPS using dilute NaCl brine (Table B.1)

Table B.1: Current density required to protect an AISI 1018 carbon steel elbow in 0.1 M NaCl solution at 0, 10, 20, and 30 wt.% slurry concentration using 1.05 mm diameter sand particles.

Fluid Velocity (m/s)	Protection Current Density (mA/cm^2)			
	Slurry Concentration			
	0 wt.%	10 wt.%	20 wt.%	30 wt.%
2.5	1.205	1.430	1.435	1.253
3.0	1.365	1.456	1.369	1.285
3.5	1.366	1.503	1.418	1.336
4.0	1.338	1.562	1.483	1.363

Appendix C

Summation of Phase III Results

This appendix displays the following data:

- Results of the current density required to protect AISI 1018 steel elbows in saturated potash brine using the 1.05 mm diameter sand particle (Table C.1 – C.4)
- Results of the current density required to protect AISI 1018 steel elbows in saturated potash brine using the 0.55 mm diameter sand particle (Table C.5 – C.8)

Table C.1: Averaged protection current density required to protect AISI 1018 carbon steel elbows in saturated potash brine at 2.5 m/s from 0 to 35 wt.% sand concentration using 1.05 mm sand.

Slurry Concentration (wt.%)	Cathodic Protection Current Density (mA/cm^2)									Average Current Density (mA/cm^2)	95% Confidence Interval (mA/cm^2)
	Experimental Trials										
	1	2	3	4	5	6	7	8	9		
0	0.902	1.088	0.824	0.826	0.814	0.989	0.823	1.073	0.995	0.926	0.070
1	0.924	1.140	0.877	0.878	0.887	0.987	0.855	1.121	1.031	0.967	0.068
2	0.948	1.175	0.920	0.911	0.935	1.078	0.895	1.174	1.069	1.012	0.070
3	0.975	1.215	0.955	0.936	0.947	1.093	0.935	1.231	1.108	1.044	0.075
4	1.002	1.244	0.983	0.967	0.995	1.105	0.967	1.267	1.143	1.075	0.074
5	1.028	1.267	1.013	0.991	0.956	1.131	0.995	1.271	1.173	1.092	0.076
6	1.056	1.271	1.037	1.020	1.044	1.151	1.023	1.287	1.203	1.121	0.067
7	1.066	1.267	1.071	1.046	1.069	1.164	1.047	1.292	1.221	1.138	0.062
8	1.063	1.250	1.090	1.065	1.080	1.153	1.063	1.292	1.236	1.144	0.057
9	1.063	1.245	1.098	1.072	1.079	1.164	1.069	1.283	1.241	1.146	0.055
10	1.052	1.217	1.102	1.080	1.068	1.157	1.071	1.270	1.242	1.140	0.052
11	1.042	1.189	1.101	1.077	1.061	1.138	1.064	1.256	1.242	1.130	0.050
12	1.028	1.162	1.094	1.070	1.045	1.118	1.055	1.238	1.237	1.116	0.049
13	1.015	1.137	1.082	1.059	1.028	1.104	1.042	1.210	1.228	1.101	0.048
14	1.002	1.115	1.065	1.043	1.020	1.087	1.026	1.192	1.215	1.085	0.047
15	0.992	1.099	1.047	1.030	1.000	1.062	1.014	1.185	1.200	1.070	0.048
16	0.991	1.094	1.032	1.018	1.005	1.053	1.002	1.187	1.181	1.063	0.047
17	0.990	1.088	1.012	1.007	0.989	1.036	0.990	1.183	1.164	1.051	0.047
18	0.994	1.084	1.006	1.005	0.996	1.024	0.983	1.181	1.151	1.047	0.046
19	0.996	1.077	1.009	1.000	0.997	1.015	0.980	1.168	1.142	1.043	0.043
20	0.993	1.067	1.014	1.000	0.986	1.015	0.983	1.160	1.135	1.039	0.041
21	0.988	1.053	1.014	1.003	0.989	1.014	0.987	1.149	1.130	1.036	0.039
22	0.978	1.039	1.007	1.003	0.988	1.015	0.992	1.132	1.131	1.032	0.037
23	0.970	1.023	1.010	0.998	0.954	1.008	0.980	1.119	1.131	1.022	0.039
24	0.960	1.011	1.018	0.990	0.973	1.001	0.975	1.093	1.131	1.017	0.036

Table C.1: Averaged protection current density required to protect AISI 1018 carbon steel elbows in saturated potash brine at 2.5 m/s from 0 to 35 wt.% sand concentration using 1.05 mm sand cont'd.

Slurry Concentration (wt.%)	Cathodic Protection Current Density (mA/cm^2)									Average Current Density (mA/cm^2)	95% Confidence Interval (mA/cm^2)
	Experimental Trials										
	1	2	3	4	5	6	7	8	9		
25	0.953	0.997	1.005	0.980	0.962	0.989	0.968	1.079	1.121	1.006	0.035
26	0.945	0.987	0.992	0.972	0.954	0.974	0.960	1.070	1.108	0.996	0.035
27	0.940	0.980	0.980	0.961	0.944	0.975	0.951	1.055	1.099	0.987	0.034
28	0.943	0.980	0.969	0.952	0.934	0.962	0.944	1.053	1.089	0.981	0.034
29	0.946	0.984	0.957	0.943	0.924	0.955	0.938	1.059	1.075	0.976	0.034
30	0.951	0.985	0.952	0.936	0.928	0.949	0.938	1.051	1.064	0.973	0.031
31	0.954	0.988	0.946	0.932	0.928	0.949	0.940	1.047	1.052	0.971	0.030
32	0.955	0.982	0.936	0.938	0.930	0.958	0.948	1.035	1.038	0.969	0.026
33	0.953	0.982	0.947	0.945	0.928	0.958	0.955	1.032	1.038	0.971	0.024
34	0.950	0.978	0.945	0.947	0.886	0.960	0.955	1.022	1.035	0.964	0.027
35	0.945	0.968	0.924	0.944	0.926	0.952	0.955	1.014	1.027	0.962	0.022

Table C.2: Averaged protection current density required to protect AISI 1018 carbon steel elbows in saturated potash brine at 3.0 m/s from 0 to 35 wt.% sand concentration using 1.05 mm sand.

Slurry Concentration (wt.%)	Cathodic Protection Current Density (mA/cm^2)				Average Current Density (mA/cm^2)	95% Confidence Interval (mA/cm^2)
	Experimental Trials					
	1	2	3	4		
0	1.044	0.918	0.993	1.093	1.012	0.070
1	1.102	0.971	1.017	1.130	1.055	0.068
2	1.140	1.017	1.059	1.172	1.097	0.070
3	1.175	1.055	1.079	1.206	1.129	0.075
4	1.196	1.084	1.118	1.231	1.157	0.074
5	1.215	1.114	1.136	1.261	1.182	0.076
6	1.228	1.142	1.162	1.287	1.205	0.067
7	1.235	1.168	1.176	1.304	1.221	0.062
8	1.233	1.184	1.191	1.312	1.230	0.057
9	1.224	1.194	1.186	1.298	1.225	0.055
10	1.212	1.187	1.189	1.283	1.218	0.052
11	1.198	1.186	1.192	1.277	1.213	0.050
12	1.180	1.171	1.166	1.272	1.197	0.049
13	1.159	1.154	1.163	1.251	1.182	0.048
14	1.142	1.137	1.153	1.239	1.168	0.047
15	1.131	1.117	1.163	1.217	1.157	0.048
16	1.127	1.101	1.161	1.202	1.148	0.047
17	1.130	1.095	1.164	1.190	1.145	0.047
18	1.132	1.098	1.169	1.194	1.148	0.046
19	1.128	1.104	1.175	1.188	1.149	0.043
20	1.121	1.103	1.178	1.190	1.148	0.041
21	1.112	1.100	1.167	1.188	1.142	0.039
22	1.103	1.090	1.157	1.189	1.135	0.037
23	1.094	1.083	1.155	1.178	1.127	0.039
24	1.084	1.072	1.143	1.166	1.116	0.036
25	1.074	1.060	1.140	1.157	1.108	0.035
26	1.068	1.052	1.148	1.148	1.104	0.035
27	1.067	1.046	1.141	1.132	1.097	0.034
28	1.073	1.046	1.156	1.117	1.098	0.034
29	1.080	1.051	1.149	1.114	1.098	0.034
30	1.082	1.059	1.153	1.114	1.102	0.031
31	1.076	1.059	1.147	1.127	1.102	0.030
32	1.074	1.063	1.143	1.124	1.101	0.026
33	1.071	1.061	1.141	1.123	1.099	0.024
34	1.066	1.058	1.135	1.122	1.095	0.027
35	1.052	1.056	1.131	1.114	1.089	0.022

Table C.3: Averaged protection current density required to protect AISI 1018 carbon steel elbows in saturated potash brine at 3.5 m/s from 0 to 35 wt.% sand concentration using 1.05 mm sand.

Slurry Concentration (wt.%)	Cathodic Protection Current Density (mA/cm^2) Experimental Trials			Average Current Density (mA/cm^2)	95% Confidence Interval (mA/cm^2)
	1	2	3		
0	1.067	1.204	1.077	1.116	0.070
1	1.141	1.346	1.157	1.215	0.068
2	1.198	1.424	1.199	1.274	0.070
3	1.244	1.458	1.232	1.311	0.075
4	1.284	1.474	1.274	1.344	0.074
5	1.313	1.473	1.303	1.363	0.076
6	1.334	1.470	1.326	1.376	0.067
7	1.341	1.466	1.344	1.384	0.062
8	1.337	1.452	1.350	1.380	0.057
9	1.333	1.428	1.338	1.366	0.055
10	1.321	1.409	1.338	1.356	0.052
11	1.301	1.393	1.329	1.341	0.050
12	1.279	1.378	1.322	1.326	0.049
13	1.264	1.375	1.304	1.314	0.048
14	1.260	1.376	1.295	1.310	0.047
15	1.267	1.386	1.292	1.315	0.048
16	1.276	1.387	1.300	1.321	0.047
17	1.276	1.378	1.310	1.321	0.047
18	1.266	1.364	1.325	1.318	0.046
19	1.260	1.352	1.327	1.313	0.043
20	1.253	1.336	1.327	1.305	0.041
21	1.245	1.312	1.310	1.289	0.039
22	1.234	1.315	1.292	1.280	0.037
23	1.226	1.314	1.286	1.275	0.039
24	1.213	1.313	1.277	1.267	0.036
25	1.203	1.302	1.272	1.259	0.035
26	1.194	1.294	1.278	1.255	0.035
27	1.190	1.291	1.298	1.259	0.034
28	1.187	1.284	1.293	1.255	0.034
29	1.193	1.274	1.288	1.252	0.034
30	1.198	1.270	1.276	1.248	0.031
31	1.198	1.266	1.269	1.244	0.030
32	1.198	1.270	1.256	1.241	0.026
33	1.196	1.286	1.254	1.245	0.024
34	1.194	1.286	1.250	1.243	0.027
35	1.191	1.278	1.258	1.243	0.022

Table C.4: Averaged protection current density required to protect AISI 1018 carbon steel elbows in saturated potash brine at 4.0 m/s from 0 to 35 wt.% sand concentration using 1.05 mm sand.

Slurry Concentration (wt.%)	Cathodic Protection Current Density (mA/cm^2)			Average Current Density (mA/cm^2)	95% Confidence Interval (mA/cm^2)
	Experimental Trials				
	1	2	3		
0	1.112	1.215	1.234	1.187	0.070
1	1.214	1.408	1.377	1.333	0.068
2	1.278	1.412	1.465	1.385	0.070
3	1.338	1.364	1.513	1.405	0.075
4	1.367	1.382	1.534	1.428	0.074
5	1.387	1.384	1.537	1.436	0.076
6	1.389	1.330	1.536	1.418	0.067
7	1.386	1.351	1.525	1.421	0.062
8	1.380	1.368	1.515	1.421	0.057
9	1.374	1.372	1.507	1.418	0.055
10	1.367	1.377	1.487	1.410	0.052
11	1.361	1.387	1.491	1.413	0.050
12	1.358	1.395	1.481	1.411	0.049
13	1.368	1.398	1.470	1.412	0.048
14	1.376	1.382	1.456	1.405	0.047
15	1.375	1.381	1.452	1.403	0.048
16	1.370	1.369	1.458	1.399	0.047
17	1.364	1.377	1.468	1.403	0.047
18	1.359	1.388	1.459	1.402	0.046
19	1.365	1.386	1.453	1.402	0.043
20	1.372	1.381	1.441	1.398	0.041
21	1.381	1.378	1.433	1.397	0.039
22	1.374	1.375	1.436	1.395	0.037
23	1.371	1.359	1.438	1.389	0.039
24	1.371	1.356	1.432	1.386	0.036
25	1.368	1.360	1.426	1.385	0.035
26	1.364	1.365	1.419	1.383	0.035
27	1.361	1.357	1.412	1.376	0.034
28	1.363	1.349	1.408	1.373	0.034
29	1.368	1.350	1.406	1.375	0.034
30	1.374	1.349	1.409	1.377	0.031
31	1.372	1.350	1.403	1.375	0.030
32	1.359	1.349	1.400	1.369	0.026
33	1.360	1.347	1.394	1.367	0.024
34	1.363	1.358	1.388	1.370	0.027
35	1.365	1.356	1.385	1.369	0.022

Table C.5: Averaged current density data found by cathodically protecting AISI 1018 carbon steel elbows in saturated potash brine at 2.5 m/s from 0 to 35 wt.% sand concentration using 0.55 mm sand.

Slurry Concentration (wt.%)	Cathodic Protection Current Density (mA/cm^2)										Average Current Density (mA/cm^2)	95% Confidence Interval (mA/cm^2)
	Experimental Trials											
	1	2	3	4	5	6	7	8	9	10		
0	0.939	0.896	0.883	1.005	0.947	1.066	0.928	0.891	0.859	0.850	0.926	0.039
1	0.967	0.917	0.907	1.119	0.961	1.174	0.965	0.971	0.926	0.899	0.981	0.053
2	0.991	0.991	0.920	1.164	0.998	1.210	0.987	1.028	1.036	0.932	1.026	0.054
3	0.934	1.026	0.941	1.204	1.032	1.224	1.013	1.071	1.090	0.969	1.050	0.058
4	1.022	1.020	0.961	1.234	1.065	1.262	1.037	1.107	1.148	0.999	1.086	0.058
5	1.027	1.058	0.981	1.249	1.098	1.298	1.059	1.137	1.257	1.032	1.120	0.064
6	1.071	1.084	0.954	1.256	1.125	1.318	1.074	1.164	1.189	1.057	1.129	0.061
7	1.051	1.097	1.008	1.255	1.151	1.323	1.098	1.188	1.183	1.089	1.144	0.055
8	1.096	1.082	1.015	1.249	1.176	1.331	1.120	1.214	1.176	1.123	1.158	0.053
9	1.124	1.051	1.020	1.235	1.189	1.332	1.134	1.234	1.172	1.137	1.163	0.053
10	1.111	1.096	1.017	1.219	1.201	1.307	1.147	1.249	1.162	1.151	1.166	0.048
11	1.129	1.087	1.010	1.195	1.198	1.298	1.134	1.252	1.151	1.183	1.164	0.047
12	1.125	1.046	1.001	1.172	1.199	1.276	1.136	1.246	1.144	1.164	1.151	0.048
13	1.095	1.068	0.951	1.152	1.176	1.257	1.137	1.238	1.135	1.172	1.138	0.051
14	1.028	1.056	0.935	1.141	1.161	1.239	1.126	1.227	1.122	1.179	1.121	0.054
15	0.966	1.051	0.957	1.133	1.153	1.211	1.105	1.215	1.118	1.166	1.108	0.053
16	1.064	1.050	0.948	1.129	1.146	1.202	1.095	1.196	1.137	1.169	1.114	0.045
17	1.018	1.057	0.933	1.128	1.140	1.201	1.090	1.178	1.140	1.166	1.105	0.048
18	1.039	1.063	0.949	1.126	1.137	1.203	1.085	1.157	1.148	1.131	1.104	0.042
19	1.013	1.059	0.956	1.120	1.139	1.206	1.084	1.137	1.145	1.148	1.101	0.043
20	1.015	1.041	0.961	1.104	1.144	1.206	1.090	1.120	1.142	1.138	1.096	0.042
21	1.024	1.052	0.965	1.090	1.150	1.203	1.101	1.109	1.139	1.147	1.098	0.040
22	1.024	1.047	0.965	1.079	1.155	1.194	1.110	1.105	1.134	1.164	1.098	0.041
23	0.967	1.037	0.964	1.067	1.157	1.183	1.117	1.105	1.126	1.171	1.090	0.046
24	1.026	1.026	0.960	1.055	1.156	1.173	1.120	1.109	1.116	1.179	1.092	0.042

Table C.5: Averaged current density data found by cathodically protecting AISI 1018 carbon steel elbows in saturated potash brine at 2.5 m/s from 0 to 35 wt.% sand concentration using 0.55 mm sand cont'd.

Slurry Concentration (wt.%)	Cathodic Protection Current Density (mA/cm^2)										Average Current Density (mA/cm^2)	95% Confidence Interval (mA/cm^2)
	Experimental Trials											
	1	2	3	4	5	6	7	8	9	10		
25	0.999	1.031	0.952	1.046	1.148	1.161	1.120	1.111	1.106	1.172	1.084	0.043
26	1.017	1.013	0.946	1.039	1.140	-	1.116	1.111	1.107	1.171	1.073	0.045
27	0.995	1.008	0.947	1.038	1.134	-	1.105	1.109	1.094	1.171	1.067	0.045
28	1.012	1.015	0.953	1.041	1.125	-	1.100	1.111	1.089	1.161	1.067	0.041
29	0.994	1.009	0.965	1.046	1.116	-	1.094	1.108	1.104	1.165	1.067	0.041
30	1.011	0.968	0.977	1.057	1.107	-	1.088	1.105	1.112	1.146	1.063	0.040
31	1.017	1.034	0.984	1.057	1.103	-	1.086	1.101	1.110	1.139	1.070	0.031
32	1.001	1.028	0.985	1.057	1.105	-	1.084	1.095	1.119	1.127	1.067	0.032
33	1.010	1.025	0.984	1.055	1.111	-	1.088	1.086	1.113	1.129	1.067	0.031
34	1.001	1.021	0.983	1.055	1.116	-	1.095	1.079	1.102	1.141	1.066	0.034
35	1.009	1.009	0.979	1.045	1.120	-	1.100	1.072	1.098	1.153	1.065	0.036

Table C.6: Averaged current density data found by cathodically protecting AISI 1018 carbon steel elbows in saturated potash brine at 3.0 m/s from 0 to 35 wt.% sand concentration using 0.55 mm sand.

Slurry Concentration (wt.%)	Cathodic Protection Current Density (mA/cm^2)			Average Current Density (mA/cm^2)	95% Confidence Interval (mA/cm^2)
	Experimental Trials				
	1	2	3		
0	1.009	1.087	0.948	1.015	0.039
1	1.067	1.163	1.075	1.101	0.053
2	1.118	1.217	1.105	1.147	0.054
3	1.167	1.223	1.125	1.172	0.058
4	1.212	1.264	1.135	1.203	0.058
5	1.262	1.302	1.137	1.234	0.064
6	1.283	1.313	1.139	1.245	0.061
7	1.298	1.333	1.140	1.257	0.055
8	1.309	1.346	1.144	1.266	0.053
9	1.312	1.347	1.150	1.270	0.053
10	1.311	1.344	1.161	1.272	0.048
11	1.305	1.338	1.175	1.272	0.047
12	1.298	1.327	1.185	1.270	0.048
13	1.279	1.295	1.190	1.254	0.051
14	1.262	-	1.189	1.225	0.054
15	1.256	1.250	1.187	1.231	0.053
16	1.257	1.240	1.183	1.227	0.045
17	1.264	1.242	1.177	1.228	0.048
18	1.270	1.250	1.170	1.230	0.042
19	1.268	1.258	1.162	1.229	0.043
20	1.269	1.258	1.155	1.228	0.042
21	1.264	1.256	1.155	1.225	0.040
22	1.259	1.249	1.159	1.222	0.041
23	1.251	1.241	1.168	1.220	0.046
24	1.246	1.232	1.174	1.217	0.042
25	1.243	1.222	1.175	1.213	0.043
26	1.245	1.212	1.174	1.211	0.045
27	1.254	1.202	1.169	1.208	0.045
28	1.260	1.195	1.163	1.206	0.041
29	1.265	1.192	1.158	1.205	0.041
30	1.266	1.197	1.151	1.205	0.040
31	1.263	1.199	1.145	1.202	0.031
32	1.253	1.199	1.144	1.199	0.032
33	1.243	1.197	1.148	1.196	0.031
34	1.228	1.192	1.159	1.193	0.034
35	1.224	1.187	1.167	1.193	0.036

Table C.7: Averaged current density data found by cathodically protecting AISI 1018 carbon steel elbows in saturated potash brine at 3.5 m/s from 0 to 35 wt.% sand concentration using 0.55 mm sand.

Slurry Concentration (wt.%)	Cathodic Protection Current Density (mA/cm^2)					Average Current Density (mA/cm^2)	95% Confidence Interval (mA/cm^2)
	Experimental Trials						
	1	2	3	4	5		
0	1.141	0.993	1.030	1.188	1.209	1.112	0.039
1	1.202	1.149	1.148	1.285	1.248	1.206	0.053
2	1.249	1.210	1.229	1.357	1.305	1.270	0.054
3	1.294	1.263	1.263	1.408	1.352	1.316	0.058
4	1.320	1.300	1.278	1.436	1.395	1.346	0.058
5	1.340	1.325	1.283	1.445	1.432	1.365	0.064
6	1.346	1.337	1.273	1.448	1.464	1.373	0.061
7	1.352	1.337	1.238	1.450	1.489	1.373	0.055
8	1.345	1.333	1.225	1.444	1.502	1.370	0.053
9	1.333	1.321	1.211	1.421	1.502	1.357	0.053
10	1.321	1.311	1.210	1.405	1.495	1.348	0.048
11	1.309	1.293	1.221	1.389	1.477	1.338	0.047
12	1.281	1.279	1.205	1.371	1.462	1.320	0.048
13	1.271	1.266	1.221	1.361	1.441	1.312	0.051
14	1.291	1.269	1.235	1.360	1.418	1.315	0.054
15	1.300	1.279	1.243	1.368	1.400	1.318	0.053
16	1.296	1.288	1.239	1.377	1.395	1.319	0.045
17	1.291	1.284	1.236	1.379	1.395	1.317	0.048
18	1.288	1.275	1.227	1.373	1.403	1.313	0.042
19	1.278	1.266	1.224	1.364	1.404	1.307	0.043
20	1.271	1.257	1.224	1.351	1.393	1.299	0.042
21	1.269	1.248	1.224	1.337	1.381	1.292	0.040
22	1.273	1.240	1.234	1.325	1.371	1.289	0.041
23	1.282	1.236	1.242	1.314	1.361	1.287	0.046
24	1.288	1.240	1.244	1.311	1.349	1.287	0.042
25	1.289	1.246	1.244	1.316	1.335	1.286	0.043
26	1.288	1.249	1.243	1.317	1.332	1.286	0.045
27	1.285	1.243	1.238	1.315	1.339	1.284	0.045
28	1.280	1.238	1.231	1.308	1.344	1.280	0.041
29	1.276	1.234	1.227	1.301	1.343	1.276	0.041
30	1.274	1.228	1.227	1.293	1.338	1.272	0.040
31	1.274	1.224	1.231	1.286	1.335	1.270	0.031
32	1.279	1.224	1.237	1.280	1.328	1.269	0.032
33	1.287	1.232	1.240	1.280	1.322	1.272	0.031
34	1.292	1.241	1.241	1.287	1.318	1.276	0.034
35	1.293	1.244	1.239	1.294	1.320	1.278	0.036

Table C.8: Averaged current density data found by cathodically protecting AISI 1018 carbon steel elbows in saturated potash brine at 4.0 m/s from 0 to 35 wt.% sand concentration using 0.55 mm sand.

Slurry Concentration (wt.%)	Cathodic Protection Current Density (mA/cm^2)					Average Current Density (mA/cm^2)	95% Confidence Interval (mA/cm^2)
	Experimental Trials						
	1	2	3	4	5		
0	1.053	1.138	1.267	1.178	1.332	1.194	0.039
1	1.194	1.265	1.411	1.383	1.463	1.343	0.053
2	1.267	1.354	1.482	1.432	1.551	1.417	0.054
3	1.314	1.408	1.519	1.455	1.628	1.465	0.058
4	1.332	1.434	1.520	1.464	1.685	1.487	0.058
5	1.332	1.444	1.517	1.462	1.716	1.494	0.064
6	1.321	1.446	1.488	1.453	1.708	1.483	0.061
7	1.304	1.446	1.475	1.441	1.685	1.470	0.055
8	1.289	1.437	1.451	1.429	1.668	1.455	0.053
9	1.287	1.437	1.433	1.417	1.652	1.445	0.053
10	1.287	1.430	1.406	1.403	1.628	1.431	0.048
11	1.296	1.453	1.407	1.399	1.610	1.433	0.047
12	1.305	1.452	1.416	1.404	1.589	1.433	0.048
13	1.309	1.459	1.420	1.415	1.576	1.436	0.051
14	1.308	1.467	1.419	1.414	1.578	1.437	0.054
15	1.308	1.467	1.414	1.409	1.580	1.436	0.053
16	1.302	1.461	-	1.399	1.577	1.435	0.045
17	1.300	1.454	1.460	1.389	1.566	1.434	0.048
18	1.306	1.445	1.462	1.384	1.553	1.430	0.042
19	1.316	1.442	1.465	1.384	1.536	1.429	0.043
20	1.321	1.444	1.465	1.390	1.521	1.428	0.042
21	1.320	1.450	1.449	1.394	1.513	1.425	0.040
22	1.315	1.452	1.446	1.395	1.512	1.424	0.041
23	1.311	1.448	1.445	1.390	1.514	1.422	0.046
24	1.307	1.443	1.452	1.387	1.511	1.420	0.042
25	1.313	1.434	1.460	1.383	1.503	1.419	0.043
26	1.319	1.430	1.461	1.383	1.496	1.418	0.045
27	1.323	1.434	1.460	1.388	1.489	1.419	0.045
28	1.322	1.441	1.454	1.397	1.485	1.420	0.041
29	1.319	1.445	1.450	1.398	1.485	1.419	0.041
30	1.320	1.444	1.446	1.397	1.487	1.419	0.040
31	1.320	1.438	1.450	1.394	1.489	1.418	0.031
32	1.322	1.432	1.455	1.389	1.487	1.417	0.032
33	1.328	1.427	1.458	1.389	1.483	1.417	0.031
34	1.333	1.426	1.459	1.394	1.480	1.418	0.034
35	1.333	1.427	1.458	1.401	1.475	1.419	0.036

Appendix D

Summation of Phase IV Results

This appendix displays the following data:

- Results of determining E_{corr} at various flow loop operating conditions (Table D.1)
- Results of determining i_{corr} at various flow loop operating conditions (Table D.2)
- Results showing the corrosion rate determined from i_{corr} at various flow loop operating conditions (Table D.3)
- Results from determining the verification data point to confirm the correlation between protective current density and corrosion rate (Table D.4)

Table D.1: Determining E_{corr} of AISI 1018 carbon steel elbows in saturated potash brine at various flow loop operating conditions.

Flow Loop Velocity (m/s)	Slurry Concentration (wt.%)	E_{corr} (V_{SCE})				Average E_{corr} (V_{SCE})	95% Confidence Interval (V_{SCE})
		Trial 1	Trial 2	Trial 3	Trial 4		
2.5	0	-0.622	-0.605	-0.632	-0.640	-0.620	0.020
3.0	0	-0.612	-0.592	-0.602	-0.634	-0.610	0.024
3.5	0	-0.61	-0.591	-0.584	-0.612	-0.596	0.020
4.0	0	-0.588	-0.584	-0.578	-0.590	-0.584	0.008
4.0	5	-0.562	-0.558	-0.578	-	-0.566	0.018

Table D.2: Determining i_{corr} of AISI 1018 carbon steel elbows in saturated potash brine at various flow loop operating conditions.

Flow Loop Velocity (m/s)	Slurry Concentration (wt.%)	i_{corr} (A)						Average i_{corr} (A)	Avg Current Density (mA/cm^2)	95% Confidence Interval (mA/cm^2)
		Trial 1	Trial 2	Trial 3	Trial 4	Trial 5	Trial 6			
2.5	0	0.009	0.010	0.010	0.012	0.010	-	0.010	0.200	0.026
3	0	0.011	0.012	0.012	0.014	0.012	-	0.012	0.240	0.023
3.5	0	0.014	0.014	0.015	0.017	0.015	-	0.015	0.296	0.023
4	0	0.016	0.016	0.018	0.019	0.017	-	0.017	0.341	0.023
4	5	0.021	0.025	0.022	0.012	0.017	0.026	0.021	0.405	0.083

Table D.3: The corrosion rate as determined from measurement of i_{corr} at various flow loop operating conditions.

Flow Loop Velocity (m/s)	Slurry Concentration (wt.%)	Corrosion Rate (g/m^2hr)						Average Corrosion Rate (g/m^2hr)	95% Confidence Interval (g/m^2hr)
		Trial 1	Trial 2	Trial 3	Trial 4	Trial 5	Trial 6		
2.5	0	1.765	2.094	2.010	2.540	2.046	-	2.09	0.27
3	0	2.309	2.417	2.437	2.946	2.455	-	2.51	0.24
3.5	0	2.917	2.916	3.049	3.524	3.044	-	3.09	0.24
4	0	3.365	3.308	3.605	3.958	3.583	-	3.56	0.24
4	5	4.290	5.192	4.530	5.046	3.542	5.337	4.66	0.56

Table D.4: Determination of i_{corr}, E_{corr}, and corrosion rate at a flow loop velocity of 2.5 m/s and 5 wt.% slurry concentration to verify correlation between protective current density and corrosion rate.

Measured Value	Experiments						Average	Average Current Density (mA/cm^2)	95% Confidence Interval
	Trial 1	Trial 2	Trial 3	Trial 4	Trial 5	Trial 6			
E_{corr} (V_{SCE})	-0.602	-0.600	-0.594	-0.592	-0.594	-	-0.596	N/A	0.004 V_{SCE}
i_{corr} (A)	0.011	0.021	0.016	0.008	0.013	0.022	0.015	0.302	0.091 mA/cm^2
Corrosion rate (g/m^2hr)	2.221	4.342	3.387	3.312	2.764	4.577	3.43	N/A	0.74 g/m^2hr

Appendix E

Supporting Documents

This appendix displays the following data:

- SDS data sheet for the refined, untreated potash ore used in experiments (E.1)
- Sand size distribution tables and material data sheets (E.2 and E.3)
- AISI 1018 carbon steel elbow material data sheet (E.4)

E.1: Material Safety Data Sheet for the untreated potash ore used in flow loop experiments.

PCS Sales

Potash

Safety Data Sheet 100

Revision date 04/30/2015 : Version: 1.0

SECTION 1: Identification of the substance/mixture and of the company/undertaking

1.1. Product identifier

Product form	: Mixture
Substance name	: Potash
Product code	: GRA, SOG, STD, SUS
Product group	: Commercial product
Other means of identification	: Muriate of Potash: Granular, Standard, and Suspension Grades, WST

1.2. Relevant identified uses of the substance or mixture and uses advised against

Use of the substance/preparation : Fertilizer

1.3. Details of the supplier of the safety data sheet

PCS Sales (USA), Inc.
1101 Skokie Blvd.
Suite 400
Northbrook, IL 60062
T 800-241-6908 / 847-849-4200

Suite 500
122 1st Avenue South
Saskatoon, Saskatchewan Canada S7K7G3
T 800-667-0403 (Canada) / 800-667-3930 (USA)

SDS@PotashCorp.com - www.PotashCorp.com

1.4. Emergency telephone number

Emergency number : 800-424-9300
CHEMTREC

SECTION 2: Hazards identification

2.1. Classification of the substance or mixture

GHS-US classification

Eye Irrit. 2B H320

Full text of H-phrases: see section 16

2.2. Label elements

GHS-US labelling

Signal word (GHS-US)	: Warning
Hazard statements (GHS-US)	: H320 - Causes eye irritation
Precautionary statements (GHS-US)	: P264 - Wash hands thoroughly after handling P305+P351+P338 - If in eyes: Rinse cautiously with water for several minutes. Remove contact lenses, if present and easy to do. Continue rinsing

P337+P313 - If eye irritation persists: Get medical advice/attention

2.3. Other hazards

No Pictogram according to the established criteria
No additional information available

SECTION 3: Composition/information on ingredients

3.1. Substances

Not applicable

3.2. Mixtures

Name	Product identifier	%	GHS-US classification
Potassium chloride	(CAS No.) 7447-40-7	95 - 99.8	Eye Irrit. 2B, H320
Sodium chloride	(CAS No.) 7647-14-5	1 - 4	Skin Irrit. 2, H315 Eye Irrit. 2A, H319 STOT SE 3, H335

May contain up to 0.25% base lubrication (de-dust) oil and/or 0.03% neutralized primary aliphatic (anti-cake) amine.

SECTION 4: First aid measures

4.1. Description of first aid measures

First-aid measures general : If medical advice is needed, have product container or label at hand.

First-aid measures after inhalation : If inhaled, remove to fresh air and keep at rest in a position comfortable for breathing. Give oxygen or artificial respiration if necessary. Obtain medical attention if breathing difficulty persists.

First-aid measures after skin contact : Wash skin thoroughly with mild soap and water. Obtain medical attention if irritation develops or persists.

First-aid measures after eye contact : Immediately rinse with water for a prolonged period (15 minutes) while holding the eyelids wide open including upper and lower lids. Obtain medical attention if pain and irritation develops or persists.

First-aid measures after ingestion : Do not induce vomiting. Administer water if patient is conscious. Ingesting potash will usually cause purging of the stomach by vomiting. Seek medical attention if a large amount is swallowed. Get medical advice and attention if you feel unwell.

4.2. Most important symptoms and effects, both acute and delayed

Symptoms/injuries : Irritation to eyes, skin and respiratory tract.

Symptoms/injuries after inhalation : Overexposure may be irritating to the respiratory system.

Symptoms/injuries after skin contact : May cause skin irritation.

Symptoms/injuries after eye contact : May cause eye irritation.

Symptoms/injuries after ingestion : If a large quantity has been ingested : Abdominal pain; Diarrhea; Nausea; Vomiting; Tingling in hands and feet; Weak pulse; Circulatory disturbances

Chronic symptoms : Prolonged inhalation of dust may cause respiratory irritation.

4.3. Indication of any immediate medical attention and special treatment needed

No additional information available

SECTION 5: Firefighting measures

5.1. Extinguishing media

Suitable extinguishing media : Not flammable. Use extinguishing media appropriate for surrounding fire.

Unsuitable extinguishing media : None known.

5.2. Special hazards arising from the substance or mixture

Fire hazard : Under conditions of fire this material may produce: Potassium oxides; Hydrogen chloride; Chlorine gas

Explosion hazard : Product is not explosive.

Reactivity : Stable at ambient temperature and under normal conditions of use.

5.3. Advice for firefighters

Firefighting instructions : Keep upwind. Under conditions of fire this material may produce: Potassium oxides; Hydrogen chloride; Chlorine gas

Protection during firefighting : Wear full fire-fighting turn-out gear (full Bunker gear) and respiratory protection (SCBA).

Other information : Do not allow run-off from fire fighting to enter drains or water courses.

SECTION 6: Accidental release measures

6.1. Personal precautions, protective equipment and emergency procedures

General measures : Do not breathe fumes from fires or vapours from decomposition.

6.1.1. For non-emergency personnel

Protective equipment : Wear suitable protective clothing, gloves and eye/face protection protection including tight fitting goggles in areas of high dust concentration. Wear NIOSH approved respiratory protective equipment when workplace conditions warrant use of respirator.

Emergency procedures : Collect as any solid. Ventilate area.

6.1.2. For emergency responders

Protective equipment : Wear suitable protective clothing, gloves and eye/face protection including tight fitting goggles in areas of high dust concentration. Wear NIOSH approved respiratory protective equipment when conditions warrant use of respirator.

Emergency procedures : If possible, stop flow of product. Contain and collect as any solid. Ventilate area.

6.2. Environmental precautions

If spill could potentially enter any waterway, including intermittent dry creeks, contact the U.S. COAST GUARD NATIONAL RESPONSE CENTER at 800-424-8802. In case of accident or road spill notify CHEMTREC at 800-424-9300 (in USA) or CANUTEC at 613-996-6666 (in Canada). In other countries call CHEMTREC at (International code) +1-703-527-3887.

6.3. Methods and material for containment and cleaning up

For containment : Contain and collect as any solid. Do not allow into drains or water courses or dispose of where ground or surface waters may be affected.

Methods for cleaning up	: Recover the product by vacuuming, shoveling or sweeping. Avoid generation of dust during clean-up of spills. If uncontaminated, recover and reuse as product. If on soil, remove and collect the top 5 cm of soil.

6.4. Reference to other sections

No additional information available

SECTION 7: Handling and storage

7.1. Precautions for safe handling

Additional hazards when processed	: When heated, material emits irritating fumes.
Precautions for safe handling	: Handle in accordance with good industrial hygiene and safety procedures. Avoid contact with skin and eyes. Do not eat, drink or smoke when using this product. Always wash hands after handling the product.
Hygiene measures	: Emergency eye wash fountains should be available in the immediate vicinity of any potential exposure.

7.2. Conditions for safe storage, including any incompatibilities

Storage conditions	: Store tightly closed in a dry, cool and well-ventilated place. Protect from moisture.
Special rules on packaging	: Avoid contact with aluminum or carbon steel to minimize corrosion.

7.3. Specific end use(s)

Fertilizer

SECTION 8: Exposure controls/personal protection

8.1. Control parameters

Highly soluble – No ACGIH TWA, Particulate Not Otherwise Specified (PNOS) not appropriate for highly soluble material.

8.2. Exposure controls

Appropriate engineering controls	: Ensure adequate ventilation, especially in confined areas.
Personal protective equipment	: Gloves. Safety glasses. Protective clothing.

Hand protection	: Impermeable protective gloves.
Eye protection	: Protective goggles.
Skin and body protection	: Emergency eye wash fountains and safety showers should be available in the immediate vicinity of any potential exposure. Wear suitable protective clothing. Wash contaminated clothing before reuse. Handle in accordance with good industrial hygiene and safety practice. Wash clothing frequently.
Respiratory protection	: Use NIOSH-approved air-purifying or supplied-air respirator where airborne concentrations of dust are expected to exceed exposure limits.
Environmental exposure controls	: Ensure adequate ventilation, especially in confined areas.

SECTION 9: Physical and chemical properties

9.1. Information on basic physical and chemical properties

Physical state	: Solid
Appearance	: Granular solid. Fine to 4 mm size.
Colour	: White to red
Odour	: Slight oily
Odour threshold	: No data available
pH	: 7 (approximately)
Relative evaporation rate (butylacetate=1)	: No data available
Melting point	: 771 – 773 °C (1420 – 1423 °F)
Freezing point	: No data available
Boiling point	: 1420 - 1500 °C (2588 - 2732 °F)
Flash point	: No data available
Self ignition temperature	: Not flammable
Decomposition temperature	: No data available
Flammability (solid, gas)	: Not flammable
Vapour pressure	: 80 Pa at 20°C
Relative vapour density at 20 °C	: No data available
Relative density	: No data available
Density	: 1.98 g/cc
Solubility	: Water: 347 g/l (at 20 °C)
Log Pow	: No data available
Log Kow	: No data available
Viscosity, kinematic	: No data available

Viscosity, dynamic	: No data available
Explosive properties	: None known.
Oxidising properties	: None known.
Explosive limits	: Not explosive

9.2. Other information

VOC content : < 0.5 %

SECTION 10: Stability and reactivity

10.1. Reactivity

Stable at ambient temperature and under normal conditions of use.

10.2. Chemical stability

Stable at standard temperature and pressure.

10.3. Possibility of hazardous reactions

Hazardous polymerization will not occur.

10.4. Conditions to avoid

Protect from moisture.

10.5. Incompatible materials

Contact with acids liberates toxic gas (chlorine). Contact with hot nitric acid may produce toxic nitrosyl chloride.

10.6. Hazardous decomposition products

Contact with strong acids may produce hydrogen chlorine gas.

SECTION 11: Toxicological information

11.1. Information on toxicological effects

Acute toxicity : Not classified

Potash	
Additional information	Potassium chloride is listed by the FDA as "Generally Recognized as Safe" (GRAS) and may be used as a food additive according to prescribed conditions.

Potassium chloride (7447-40-7)	
LD50 oral rat	2600 mg/kg

Sodium chloride (7647-14-5)	
LD50 oral rat	3 g/kg
LD50 dermal rabbit	> 10 g/kg
LC50 inhalation rat (mg/l)	> 42 g/m³ (Exposure time: 1 h)

Serious eye damage/irritation	: Causes eye irritation pH: 7 (approximately)
Respiratory or skin sensitisation	: Not classified
Germ cell mutagenicity	: Not classified
Carcinogenicity	: Not classified
Reproductive toxicity	: Not classified
Specific target organ toxicity (single exposure)	: Not classified
Specific target organ toxicity (repeated exposure)	: Not classified
Aspiration hazard	: Not classified

SECTION 12: Ecological information

12.1. Toxicity

Ecotoxicity:	**Acute Toxicity to Fish:**	(*Lepomis macrochirus*) (blue gill) – 96 hour - LC_{50} = 2010 mg/L (ppm KCl)
	Chronic Toxicity to Fish:	No data available
	Acute Toxicity to Aquatic Invertebrates:	(*Daphnia magna*) - 48 hours - EC_{50} = 337 – 825 mg/L; (*Physa heterostropha*) - 96 hrs - LC_{50} = 940 mg/L.
	Chronic Toxicity to Aquatic Invertebrates:	No data available
	Toxicity to Aquatic Plants:	((*Nitzschia linearis*)diatom) - 5 days- 120 hour TL_m = 1,337 ppm KCl; (*Scendesmus subspicatus*) 72 hour - EC_{50} = 2,500 mg/L. (*Chlorella vulgaris*) - 3 – 4 months - NOEC = 600 mg KCl/L, LOEL = 700 mg KCl/L
	Toxicity to Bacteria: (activated)	No data available
	Toxicity to Soil Dwelling Organisms:	No data available
	Toxicity to Terrestrial Plants:	No data available
Environmental Fate:	**Stability in Water:**	Ions can persist, dissociates in water
	Stability in Soil:	Binds to clay particles
	Transport and Distribution:	1.51×10^{-4} % to air; 45.2% to water; 54.7% to soil; 0.0755% to sediment
Toxicity:	Not toxic to aquatic organisms defined by USEPA	
Degradation Products:	**Biodegradation:**	No data available
	Photodegradation:	No data available

SECTION 13: Disposal considerations

13.1. Waste treatment methods

Sewage disposal recommendations : This material may be hazardous to the aquatic environment. Keep out of sewers and waterways.

Waste disposal recommendations : Place in an appropriate container and dispose of the contaminated material at a licensed site.

Additional information : Dispose of waste material in accordance with all local, regional, national, and international regulations.

SECTION 14: Transport information

In accordance with DOT / TDG / ADR / RID / ADNR / IMDG / ICAO / IATA

14.1. UN number

No dangerous good in sense of transport regulations.

14.2. UN proper shipping name

Not applicable

14.2 Additional information

Other information : No supplementary information available.

Overland transport

No additional information available

Transport by sea

No additional information available

Air transport

No additional information available

SECTION 15: Regulatory information

15.1. US Federal regulations

Potash	
SARA Section 311/312 Hazard Classes	Immediate (acute) health hazard

Potassium chloride (7447-40-7)
Listed on the United States TSCA (Toxic Substances Control Act) inventory

Sodium chloride (7647-14-5)
Listed on the United States TSCA (Toxic Substances Control Act) inventory

15.2. US State regulations

The following states have an OSH program approved by OSHA. If you are located in any of these states you may be under state jurisdiction rather than federal jurisdiction and your state may have more stringent requirements than OSHA. You should consult your state regulations to ensure compliance.

Alaska	Indiana	Minnesota	North Carolina	Utah
Arizona	Iowa	Nevada	Oregon	Vermont
California	Kentucky	New Mexico	Puerto Rico	*Virgin Islands
*Connecticut	Maryland	*New Jersey	South Carolina	Virginia
Hawaii	Michigan	*New York	Tennessee	Washington
*Illinois				Wyoming

*The state plans in these states apply only to public sector employers. In these states private sector employers are subject to USOL – OSHA jurisdiction. All other state plans apply to both public and private sector employers.

Sodium chloride (7647-14-5)
U.S. - Texas - Effects Screening Levels - Long Term
U.S. - Texas - Effects Screening Levels - Short Term

15.3. Canadian regulations

Potash	
WHMIS Classification	Uncontrolled product according to WHMIS classification criteria

Potassium chloride (7447-40-7)	
Listed on the Canadian DSL (Domestic Sustances List) inventory.	
WHMIS Classification	Uncontrolled product according to WHMIS classification criteria

Sodium chloride (7647-14-5)	
Listed on the Canadian DSL (Domestic Sustances List) inventory.	
WHMIS Classification	Uncontrolled product according to WHMIS classification criteria

This product has been classified in accordance with the hazard criteria of the Controlled Products Regulations (CPR) and the MSDS contains all of the information required by the CPR.

SECTION 16: Other information

NFPA health hazard : 1 - Exposure could cause irritation but only minor residual injury even if no treatment is given.

NFPA fire hazard : 0 - Materials that will not burn.

NFPA reactivity : 0 - Normally stable, even under fire exposure conditions, and are not reactive with water.

Full text of H- phrases:

Eye Irrit. 2	Serious eye damage/eye irritation Category 2
Skin Irrit. 2	Skin corrosion/irritation Category 2
STOT SE 3	Specific target organ toxicity (single exposure) Category 3
H315	Causes skin irritation
H319	Causes serious eye irritation
H335	May cause respiratory irritation

Previous PotashCorp MSDS Number : MSDS 1 - Potash

SDS US (GHS HazCom 2012)

Although the information contained is offered in good faith, SUCH INFORMATION IS EXPRESSLY GIVEN WITHOUT ANY WARRANTY (EXPRESS OR IMPLIED) OR ANY GUARANTEE OF ITS ACCURACY OR SUFFICIENCY and is taken at the user's sole risk. User is solely responsible for determining the suitability of use in each particular situation. PCS Sales specifically DISCLAIMS ANY LIABILITY WHATSOEVER FOR THE USE OF SUCH INFORMATION, including without limitation any recommendation which user may construe and attempt to apply which may infringe or violate valid patents, licenses, and/or copyright.

E.2: Grade 10 silica filter sand (nominal diameter of 1.05 mm) material data sheet.

FILTER AND WATER WELL
SILICA SANDS & GRAVELS

PRODUCT

TARGET® Filter Silica Sands and Filter Gravels are high-silica materials processed in our Morinville plant to meet the requirements of individual water filtration systems. In addition to the standard grades listed below, sands and gravels can be manufactured for projects with other specifications. In addition Target supplies a premium filter sand to meet conditions in the most demanding environments.

Certified to NSF/ANSI 61

Target Products filter sands and gravels are NSF 61 Certified and meet all AWWA B100 standards.

USES AND ADVANTAGES

TARGET Filter Sand is suitable for many rapid and slow filtration systems. The washed feedstock is dried, to sterilize the materials, then sized to meet effective size and uniformity coefficient specifications. Rigorous quality control testing, during production, assures that the final product meets the requirements of the American Water Works Association Standard B100 and is tested and certified to ANSI/NSF 61 Standards for filtering materials.

PHYSICAL PROPERTIES

	Standard Media		Premium Media
Colour	Tan		Light Beige
Grain Shape	Sub-rounded		Sub-round to rounded
Bulk Density	95 – 100 lb/ft^3 (1520 – 1600 kg/m^3)		95-1000 lb/ft^3
	Filter Sand	1.50 tonnes per m^3	1.50 tonnes per m^3
	Fine Filter Gravels	1.53 tonnes per m^3	-
	Coarse Filter Gravels	1.60 tonnes per m^3	-
Hardness, Mohs	6.5 – 7.0		6.9-7.0
Specific Gravity	2.60 – 2.65		2.63 – 2.65
Moisture Content	<0.1% weight		<0.1% weight
Acid Solubility	<5% weight		<1% weight

Bulk density values vary with particle size. Values for individual products can be determined at the time of shipping if required.

PACKAGING

Target Filter Sands are available in 22.7 kg (50 lb) plastic bags, in 25 kg (55 lb) poly woven bags or in 1.75 tonnes (3850 lb) bulk bags. Target Filter Gravels are usually supplied in 25 kg (55 lb) poly woven bags or 1.75 tonnes (3850 lb) bulk bags. Other bag sizes and bulk deliveries are available on request.

TARGET PRODUCTS LTD

FILTER AND WATER WELL
SILICA SANDS & GRAVELS

TYPICAL SIEVE ANALYSES - Percent Passing

Sieve Size		SANDS, Cumulative % Passing					
ASTM	Metric	10 – 20	16 – 30	Standard 20 – 40	Premium 20-40	30 – 50	40 – 70
No. 8	2.36 mm	100					
No. 10	2.00 mm	99 – 100					
No. 12	1.70 mm	90 – 100	100				
No. 16	1.18 mm	10 – 35	95 – 100	100	100		
No. 20	0.850 mm	0 – 3	30 – 55	90 – 100	93 - 97	100	100
No. 30	0.600 mm	0 – 1	5 – 10	20 – 45	15 - 40	80+	98+
No. 40	0.420 mm		0 – 3	5 – 10	0 - 5	30 – 45	60 – 80
No. 50	0.300 mm		0 – 1	0 – 1	0 - 1	0 – 10	15 – 30
No. 70	0.212 mm					0 – 2	1 – 3
No. 80	0.180 mm						0 – 1
Effective Size, d_{10}, mm		0.85 – 1.25	0.55 – 0.65	0.45 – 0.55	0.45 – 0.55	0.30 – 0.40	0.20 – 0.30
Uniformity Coefficient, d_{60}/d_{10}		< 1.4	< 1.6	< 1.6	< 1.4	< 1.6	< 1.6

Sieve Size		GRAVELS, Cumulative % Passing						
ASTM	Metric	1 – 2"	½ - 1"	¼ - ½"	⅛ - ¼"	1/16 - ⅛"	4 – 10	8 – 16
2"	50 mm	100						
1 ½"	38 mm	88 – 92						
1"	25 mm	0 – 10	100					
¾"	19 mm	0 – 1	92 – 98	100				
½"	12.5 mm		4 – 10	98 – 100	100			
3/8"	9.5 mm		0 – 1	50 – 80	95 – 100			
No. 3	6.7 mm			2 – 8	50 – 75	100	100	
No. 4	4.75 mm						90 – 100	100
No. 6	3.36 mm				0 – 5	99 – 100	30 – 60	98 – 100
No. 8	2.36 mm						0 – 10	85 – 95
No. 10	2.00 mm					5 – 15	0 – 1	35 – 55
No. 14	1.41 mm					0 – 1		
No. 16	1.18 mm							0 – 1
Effective Size, d_{10}, mm		19 – 24	12 – 15	7 – 8	3.0 – 3.5	1.4 – 1.7	2.4 – 2.9	1.4 – 1.7
Uniformity Coefficient, d_{90}/d_{10}		< 1.7	< 1.7	< 1.7	< 1.7	< 1.7	< 1.4	< 1.5

The sieve analyses given in the tables are typical values. Because actual values could change from time to time please confirm that effective size and uniformity coefficient values remain within specification.

TARGET PRODUCTS LTD

FILTER AND WATER WELL
SILICA SANDS & GRAVELS

TYPICAL SIEVE ANALYSES - Percent Retained

Sieve Size			SANDS, Individual % Retained				
ASTM	Metric	10 – 20	16 – 30	Standard 20 – 40	Premium 20-40	30 – 50	40 – 70
No. 8	2.36 mm	0					
No. 10	2.00 mm	0 – 1	0				
No. 12	1.70 mm	0 – 10	0				
No. 16	1.18 mm	65 – 85	0 – 5		0		
No. 20	0.850 mm	10 – 30	40 – 65	0 – 10	3 – 7		
No. 30	0.600 mm	0 – 3	20 – 45	50 – 70	55 –75	5 – 25	0 – 2
No. 40	0.420 mm		5 – 10	15 – 35	15 – 40	40 – 60	20 – 40
No. 50	0.300 mm		0 - 2	5 – 10	0 – 1	20 – 35	45 – 65
No. 70	0.212 mm					0 – 10	15 – 25
Pan		0 – 1	0 – 1	0 – 1	0 – 1	0 – 2	1 – 3
Effective Size, d_{10}, mm		0.85 – 1.25	0.55 – 0.65	0.45 – 0.55	0.45 - 0.55	0.30 – 0.40	0.20 – 0.30
Uniformity Coefficient, d_{60}/d_{10}		< 1.4	< 1.6	< 1.6	< 1.4	<1.6	<1.6

Sieve Size		GRAVELS, Individual % Retained						
ASTM	Metric	1 – 2"	½ - 1"	¼ - ½"	⅛ - ¼"	1/16 - ⅛"	4 – 10	8 – 16
1 ½"	38 mm	8 – 12						
1"	25 mm	70 – 90	0					
¾"	19 mm	0 – 10	2 – 8					
½"	12.5 mm	0 – 1	80 – 10	0 – 2				
3/8"	9.5 mm		4 – 8	30 – 50				
No. 3	6.7 mm		0 – 1	30 – 50	0 – 5			
No. 4	4.75 mm						0 – 10	
No. 6	3.36 mm			2 – 8	85 – 95	0 – 3	40 – 60	0 – 2
No. 8	2.36 mm						30 – 55	5 – 15
No. 10	2.00 mm					85 – 95	0 – 10	35 – 55
No. 14	1.41 mm					5 – 10		
No. 16	1.18 mm							35 – 55
Pan					5 – 10	0 – 3	0 – 1	0 – 1
Effective Size, d_{10}, mm		19 – 24	12 – 15	7 – 8	3.0 – 3.5	1.4 – 1.7	2.4 – 2.9	1.4 – 1.7
Uniformity Coefficient, d_{90}/d_{10}		< 1.7	< 1.7	< 1.7	< 1.7	< 1.7	< 1.4	< 1.5

The sieve analyses given in the tables are typical values. Because actual values could change from time to time please confirm that effective size and uniformity coefficient values remain within specification.

TARGET PRODUCTS LTD

FILTER AND WATER WELL
SILICA SANDS & GRAVELS

TYPICAL CHEMICAL ANALYSIS and PROPERTIES

STANDARD FILTER SAND		
Chemical Compound		Typical Value, % weight
Silica	SiO_2	93.2 – 95.6
Alumina	Al_2O_3	3.5 – 4.6
Iron Oxide	Fe_2O_3	0.30 – 0.35
Calcium Oxide	CaO	0.25 – 0.65
Magnesium Oxide	MgO	0.08 – 0.15
Potassium Oxide	K_2O	0.70 – 0.90
Sodium Oxide	Na_2O	0.65 – 0.85
Titanium Oxide	TiO_2	0.1 maximum
Loss on Ignition		0.3 maximum

PREMIUM FILTER SAND		
Chemical Compound		Typical Value, % weight
Silica	SiO_2	98.0 – 99.0
Alumina	Al_2O_3	0 – 0.3
Iron Oxide	Fe_2O_3	0 – 0.2
Calcium Oxide	CaO	0 – 0.2
Magnesium Oxide	MgO	0 – 0.3
Potassium Oxide	K_2O	0 – 0.2
Sodium Oxide	Na_2O	0 – 0.4
Titanium Oxide	TiO_2	0 – 0.2
Loss on Ignition		0 – 0.1

TARGET PRODUCTS LTD

E.3: Grade 4095 silica filter sand (nominal diameter of 0.55 mm) material data sheet.

TECHNICAL DATA

Granusil
MINERAL FILLERS

FEATURES AND BENEFITS

ST. CANUT, QUEBEC

GRANUSIL® Mineral Fillers are produced from high purity industrial quartz sands for a wide variety of industrial and contractor mixed applications which need a reliable silica contribution or require a chemically inert structural filler. Consistently uniform grain shapes and particle size distributions offer excellent placement, compaction and mechanical properties. High silica content combined with low level soluble ions, alkalis and alkaline oxides provide non-reactive service in most corrosive and exposed environments.

These durable monocrystalline structures resist abrasion in high traffic-excessive wear applications and provide the stability formulators seek in high solids emulsions, elastomerics, cemented and modified cementitious systems. GRANUSIL® is the preferred structural component in systems ranging from polymerized floor overlays to artificial sports turf.

All GRANUSIL® grades are processed and sized under rigid SPC and UNIMIN QIP℠ statistical and quality assurance programs. The result is chemical purity and consistently uniform particle size distributions for predictable performance in either manufactured or site-prepared products.

PARTICLE SIZE ANALYSIS AND PROPERTIES

Mean Values. These Do Not Represent A Specification.

	Mesh Size ASTM	Microns	4095	4020	4010	7030	8000
	12	1.70mm	---	---	---	---	---
	16	1.18mm	---	---	---	---	---
	20	850	1.3	---	---	---	---
Typical Mean %	30	600	34.9	0.7	0.5	---	---
Retained on	40	425	58.7	15.7	14.0	---	0.2
Individual Sieves	50	300	4.2	36.9	36.8	7.0	1.0
	70	212	0.7	29.3	28.3	39.2	6.2
	100	150	0.2	12.7	13.5	30.3	7.4
	140	106	---	3.6	4.6	13.5	14.2
	200	75	---	0.7	1.5	6.5	16.0
	270	53	---	---	---	---	10.3
	325	45	---	---	---	---	2.0
	PAN	PAN	---	0.4	0.8	3.5	42.7
Prior Grade Designation			4075				

Grain Shape	Subround	Visual
Hardness (Mohs)	7.0	Moh's Scale
Moisture Content (%)	<0.1	ASTM C-566
Specific Gravity (g/cm^3)	2.65	ASTM C-128
Bulk Density, loose (lb/ft^3)	92-95	ASTM C-29
Bulk Density, compacted (lb/ft^3)	98-100	ASTM C-29

TECHNICAL DATA

Granusil

CHEMICAL ANALYSIS

Mean Values. These Do Not Represent A Specification.

Mean Percent by Weight

		4095	4020	4010	7030	8000
Silicon Dioxide	(SiO_2)	99.61	99.48	99.43	99.17	95.98
Iron Oxide	(Fe_2O_3)	0.04	0.04	0.05	0.06	0.25
Aluminum Oxide	(Al_2O_3)	0.13	0.19	0.20	0.27	1.55
Calcium Oxide	(CaO)	0.05	0.07	0.08	0.21	0.83
Titanium Dioxide	(TiO_2)	0.02	0.02	0.02	0.03	0.01
Magnesium Oxide	(MgO)	0.01	0.02	0.02	0.03	0.03
Potassium Oxide	(K_2O)	0.03	0.05	0.05	0.06	0.06
Sodium Oxide	(Na_2O)	tr	tr	tr	tr	0.01
Loss on Ignition	(L.O.I.)	0.11	0.15	0.23	0.23	0.21

ORDERING INFORMATION

Shipping Point: ST. CANUT, QUEBEC, CANADA
ORIGINATING CARRIER: QUEBEC – GATINEAU RAILWAY (QGRY)

Availability: BAG AND BULK
TRUCK AND RAIL

UNIMIN

FOR PRODUCT INFORMATION AND CUSTOMER SERVICE: UNIMIN CANADA LTD.
U.S. and CANADA 800-243-9004 • FAX 800-243-9005
WORLDWIDE 416-626-1500 • FAX 416-626-1855

Silica Sands • Ground Silica • Feldspar • Ball Clay • Kaolin • Nepheline Syenite • High Purity Quartz • Olivine • Microcrystalline Silica • Bentonite Clay • Dolomite

GRADE NUMBERS INDICATE RELATIVE VALUES OR RESULTS. THEY ARE NOT A SPECIFICATION OR WARRANTY OF PERFORMANCE.

HEALTH HAZARD WARNING: Prolonged inhalation of dust associated with the materials described in this data sheet can cause delayed lung injury including Silicosis, a progressive, disabling and sometimes fatal lung disease. IARC has determined that crystalline silica, inhaled from occupational sources, can cause cancer in humans. Risk of injury is dependent on the duration and level of exposure. Follow OSHA or other relevant safety and health standards for the form of crystalline silica called Quartz. Current material safety data sheets, containing safety information, are available and should be consulted before usage.

Notice: While information contained herein is correct to the best of our knowledge, Unimin Corporation hereby disclaims any warranties as to the accuracy of the same. Recommendations or suggestions are made without guarantee or representation as to result, since conditions of usage are beyond our control. All materials are sold to Unimin Corporation standard terms and conditions of sale and the condition that buyer shall make his own tests to determine the suitability of such product for buyer's purpose. No statement contained herein shall be construed as a recommendation to infringe any patent.

Silica/Silica Containing

St. Canut – GRANUSIL-2 (06/07)

MILL TEST CERTIFICATE

Purchaser: ALBERTA PIPE FITTINGS LTD
Order No.: APF/ZICN-17
Invoice No.: ZICN180822

YINGKOU ZICN PIPE MANUFACTURING CO.,LTD
NO.72 1ST STREET OF MINXING RIVER,XISHI DISTRICT,YINGKOU, LIAONING,P.R.CHINA 115004

Date: Aug 22nd 2018
Certificate No: 1808137

CERTIFICATE COMPLYING TO EN10204-2004 3.1

Material Specification	Specification for Inspection	Visual and Dimensional	Cu+Ni+Cr+Mo	Cr+Mo	RT(5)	UT(5)	MT(5)	PT(5)
ASTM A234/A234M-17 WPB ASME SA234/SA 234M-15 WPB NACE MR0175-2015 CSAZ245.11-2013 Cat I Grade 241	ANSI B 16.9-2012 ASTM A960/A960M-16a	GOOD	≤1.00%	≤0.32%			OK	

ITEM	DESCRIPTION			QTY (PCS)	HEAT NO.	CHEMICAL COMPOSITION % MAX											MECHANICAL PROPERTY(1) Min				Sampling Methods	Heat treatment (2)	Raw Material	
						C	Mn	P	S	Si	Cr	Mo	V	Ni	Cu	CE(2)	Y.S.	T.S.	EL(7)	HB			Type (4)	Manufacturer (6)
						×10⁻²	×10⁻²	×10⁻²	×10⁻²	×10⁻²	×10⁻²	×10⁻²	×10⁻²	×10⁻²	×10⁻²	×10⁻²	Mpa	Mpa	%					
							29			10							240	415	30					
						30	106	50	58		40	15	8	40	40	50		585		197	(8)			
1	BW ELL LR90	1"	STD	1000	182	20	49	22	10	25	3	0.2	0.4	2	3	29	365	455	33	145	L	HF	1	TJCG
2	BW ELL LR90	1 1/4"	STD	2000	322	20	50	16	10	25	5	0.8	0.3	5	5	30	325	500	34	142	L	HF	1	JSSG
3	BW ELL LR90	2 1/2"	STD	100	565	20	49	10	10	23	4	1.5	0.2	5	15	31	335	480	32.6	144	L	HF	1	JSCD
4	BW ELL LR90	4"	STD	480	-17	19	57	8	5	21	3.8	0.2	0.1	3.2	10.4	30	315	455	39	145	L	HF	1	JYYY
5	BW ELL LR90	5"	STD	250	250	20	60	12	4	22	4	1	0.2	3	11	32	335	475	33	144	L	HF	1	JSCD
6	BW ELL LR90	6"	STD	500	602	21	49	5	5	21	3	1	1	5	5	31	335	490	32	141	L	HF	1	JSCD
7	BW ELL LR90	10"	STD	50	425	19	48	14	10	31	2	1	1	1	2	28	305	466	32	148	L	HF	1	SHHC
8	BW ELL LR90	12"	STD	50	830	19	48	14	10	31	2	1	1	1	2	28	300	470	32	142	L	HF	1	SHDG
9	BW ELL LR90	14"	STD	10	875	19	50	16	6	23	2	1	1	1	2	28	286	485	32	144	L	HF	1	SHHG
10	BW ELL LR90	18"	STD	10	953	16	49	18	10	22	3	3	3	2	6	27	335	485	32	141	L	HF	1	JSCD
11	BW ELL LR90	4"	XS	10	070	21	47	9	7	20	3	1.7	0.1	8	10	31	331	459	37	142	L	HF	1	JSCD
12	BW ELL LR90	6"	XS	100	966	20	50	18	9	21	2	1	1	2	5	30	330	480	35	145	L	HF	1	JSCD
13	BW ELL LR90	8"	XS	50	910	21	55	11	5	22	5	1	1	3	10	32	280	465	33	140	L	HF	1	TJCG
14	BW ELL LR90	2"	SCH160	100	178	19	52	18	7	25	2	1	2	5	8	30	330	490	35	149	L	HF	1	JSCD
15	BW ELL SR90	1 1/2"	STD	500	010	24	56	13	10	16	3	1	1	1	3	35	300	455	30	144	L	HF	1	HYHL

Note: (1) YS=Yield Strength TS=Tensile Strength EL=Elongation (2)CE=C+Mn/6+(Cr+Mo+V)/5+(Ni+Cu)/15
(3) HF: Hot formed (620-980℃) and cooled in still air. S: cold formed and normalized(900℃×0.5HR), cooled in still air,HT=Hot formed+tempered, NT=Normalized+tempered
(4) 1=seamless pipe 2=welded pipe 3=steel plate
(5) RT=Radiographical Test UT= Ultrasonic Test MT=Magnetic Particle Test PT=Penetration Test
(6) Manufacturer
(7) Standard round specimen,or small proportional specimen,min% in 4D:longitudinal-22,Transvers-14, rectangular specimen for wall thickness 5/16 and over,and for all small sizes tested in full section; min% in 2in:longitudinal-30,Transverse-20,Fittings made from plate min %:17. For each 1/32 in.decrease. in wall thickness below 5/16 in. a deduction of 1.5% for longitudinal and 1.0% for transverse from the mentioned value
(8) L: longitudinal bar T:transverse bar R: round piece

We hereby certify that the products detailed herein have been manufactured and inspected in accordance with the specifications concerned and also with the purchaser's requirements and that the test results shown herein are correct. This material was manufactured, tested, and inspected.

Stamp and signature : _____

E.4: AISI 1018 carbon steel elbow material data sheet.

Appendix F

Sample Calculations

This appendix displays the following data:

- Sample calculation of converting i_{corr} into a corrosion rate using Faradays law and a modified Faradays equation (F.1)

F.1: Converting corrosion current density (i_{corr}) into corrosion rates using a modified Faradays equation.

For an example, the corrosion rate at a flow velocity of 2.5 m/s and slurry concentration of 0 wt.% solids is shown below using Eq. [E.1] and [E.2]:

$$CR = 3.27 \cdot i_{corr} \cdot \frac{MW}{d \cdot n} \quad \text{[E.1]}$$

Or

$$CR = 3.27 \cdot i_{corr} \cdot \frac{EW}{d} \quad \text{[E.2]}$$

Using the following values:

- i_{corr} at 2.5 m/s and 0 wt.% solids = 0.200 mA/cm^2
- *MW* or atomic number = 55.845 g/mol
- n = 2
- d = 7.86 g/cm^3
- *EW* = 55.845/2 = 27.92 (unitless)

Inputting the above values in Eq. [E.2] gives:

$$CR = \left(3.27 \ \frac{g \cdot mm}{mA \cdot cm \cdot year}\right) \cdot \left(0.200 \ \frac{mA}{cm^2}\right) \cdot \frac{27.92}{7.86 \frac{g}{cm^3}} \quad \text{[E.3]}$$

$$CR = 2.323 \ \frac{mm}{year} \quad \text{[E.4]}$$

The conversion of the corrosion rate into units of g/m^{2}hr is found using tabulated conversion factors and shown below in Eq. [E.5]:

$$CR = \left(2.323\ \frac{mm}{year}\right) \cdot \left(21.6 \frac{\frac{g}{m^2 \cdot day}}{\frac{mm}{year}}\right) \cdot \left(\frac{day}{24\ hr}\right) = 2.091\ \frac{g}{m^2 \cdot hr} \quad \text{[E.5]}$$

The final answer is a corrosion rate of 2.091 g/m^{2}hr on AISI 1018 carbon steel during a flow velocity of 2.5 m/s and a slurry concentration of 0 wt.% sand.

Appendix G

Permission to Use Copyright Figures

This appendix displays the following:

- Permission to use licsence numbers and publishers for Figures 2.2, 2.3, 2.4, 2.5, 2.6, 2.7, 2.8, 3.2, 4.4 and 4.5 (Table G.1)

Table G.1: Permission to Use for Copyright Material

Figure	Publisher	Domain	Liscence #
2.2	Springer Nature	Copyright Clearance Center (Marketplace)	1015572-1
2.3	Tribology International	Copyright Clearance Center (Rightslink)	4754420453823
2.4	Springer Nature	Copyright Clearance Center (Rightslink)	4757871413987
2.5	Elsevier	Copyright Clearance Center (Rightslink)	4754440517342
2.6	Springer Nature	Copyright Clearance Center (Rightslink)	4784931331976
2.7	Elsevier	Copyright Clearance Center (Rightslink)	4754870829939
2.8	Elsevier	Copyright Clearance Center (Rightslink)	4754861063488
3.2	Elsevier	Copyright Clearance Center (Rightslink)	4754850774641
4.4	NACE International	Copyright Clearance Center (Marketplace)	1015712-1
4.5	NACE International	Copyright Clearance Center (Marketplace)	1014981-1

End of Document